

SCRATCH BEHAVIOR OF POLYMERS

A Dissertation

by

GOY TECK LIM

Submitted to the Office of Graduate Studies of
Texas A&M University
in partial fulfillment of the requirements for the degree of

DOCTOR OF PHILOSOPHY

August 2005

Major Subject: Mechanical Engineering

SCRATCH BEHAVIOR OF POLYMERS

A Dissertation

by

GOY TECK LIM

Submitted to the Office of Graduate Studies of
Texas A&M University
in partial fulfillment of the requirements for the degree of

DOCTOR OF PHILOSOPHY

Approved by:

Chair of Committee,
Committee Members,

J.N. Reddy
H.-J. Sue
A. Srinivasa
S. Suh
Paul N. Roschke
Dennis O'Neal

Head of Department,

August 2005

Major Subject: Mechanical Engineering

ABSTRACT

Scratch Behavior of Polymers. (August 2005)

Goy Teck Lim, B.Eng., National University of Singapore;

M.Eng., National University of Singapore

Chair of Advisory Committee: Dr. J.N. Reddy

This dissertation work is focused on the analytical and numerical examination of the mechanical response of polypropylene (PP) under scratch deformation by a semi-spherical indenter. The finite element (FE) method is employed as the analysis technique and ABAQUS[®], a commercial FE package is adopted to perform the analysis. Important physical and computational considerations on the implementation of FE analyses for the scratch problem are reviewed. It is shown through the discussion of the generated results that a good understanding can be gained on how different scratch conditions can affect scratch behavior of PP. A phenomenological deduction of the scratch damage process and mechanisms is also established. Considering the two main damage modes of polymers, shear yielding and crazing, it is shown that the two damage modes not only exist in the scratch deformation, and moreover, that they may compete against each other for dominance. A parametric study is also performed to assess the influence of material and surface properties on scratch response of material.

A secondary research effort is also made to investigate the material constitutive modeling of polymers. Focusing on elastomeric or rubbery materials, a new mixed

network model between the Gaussian and eight-chain non-Gaussian models is proposed. This mixed model inherently preserves the good predictive power of these two models and yields better predictions over a wider range of deformation than that of the rubber model adopted by ABAQUS[®].

DEDICATION

Pursuing this dream in a foreign environment has been by far the biggest challenge I have taken on. With humility and happiness, I will dedicate this work to the following individuals who have impacted my life along this journey in their own special way:

My parents (Mr. Kim Bee Lim & Mdm. Gek Choo Sng) and my brothers (Mr. Yee Loong Lim; Mr. Gay Hong Lim and Mr. Yifa Lin) who have been supporting my dream and giving me the reasons to be strong and keep moving on.

Prof. J.N. Reddy who has realized my dream to study in USA and set me a role model to aspire to be a good researcher.

Prof. H.-J. Sue who has been providing valuable guidance for me to grow as a person and as a researcher.

Dr. A. Srinivasa who has challenged me to think better and differently.

Prof. Paul N. Roschke whose enthusiasm towards life and research has always amazed me.

Dr. S. Suh whose encouraging words have never failed to motivate me.

Three special ladies who shared memorable times with me along this arduous journey.

Ms. Cecilia and Angela Yip who have allowed me to enjoy the warmth of a family that is away from home and not forgetting their kind gestures.

Mr. Douglas E. Rodriguez who has ushered me into the American ways of life and extended his friendship that goes beyond being just a roommate.

Ms. Kay Boon Tan whose friendship and kind words have made those difficult moments easier.

My colleagues in ACML and PTC who have shown me by examples that researchers never stop learning.

Professors, colleagues and friends who have all made a difference but I have carelessly left them out.

TABLE OF CONTENTS

	Page
ABSTRACT	iii
DEDICATION.....	v
TABLE OF CONTENTS	vi
LIST OF TABLES	ix
LIST OF FIGURES	x
 CHAPTER	
I INTRODUCTION	1
Significance of Scratch Research.....	1
Review of Scratch Research	3
Dissertation Layout.....	11
II LITERATURE REVIEW AND RESEARCH SCOPE	13
Literature Review.....	13
Research Scope	15
III FINITE ELEMENT MODELING	22
Physical and Computational Considerations for FE Modeling.....	23
Analysis Steps of a Scratch Deformation.....	23
Dynamic Analysis of Scratch Step	24
Static Analyses of Indentation and Spring-Back Steps	25
Importing/Exporting between Static and Dynamic Analyses in ABAQUS®	26
FE Mesh: Geometry, Element Type and Boundary Conditions.....	28
Material Law.....	30
Plastic Yielding Criterion	31

CHAPTER		Page
	Crazing, Debonding and Cracking Criterion.....	32
	Contact Algorithm.....	33
	Surface Interaction.....	34
	Adaptive Remeshing.....	34
	Load Cases.....	35
	Convergence Study.....	37
	Time Increment for Explicit Time Integration Scheme.....	40
IV	SCRATCH DAMAGE AND CRAZE INITIATION.....	43
	Scratch Width.....	44
	Scratch Damage Process and Its Mechanism.....	46
	Quantification of Plastic Damage.....	51
	Assessment of Craze Initiation.....	54
	Plastic Yielding and Crazing.....	56
	Scratching Coefficient of Friction (μ_s).....	58
	Concluding Remarks.....	61
V	SCRATCH PARAMETRIC STUDY.....	63
	Scratch Performance.....	64
	Scheme of Parametric Study.....	66
	Parametric Study: Scratch Resistance.....	67
	Mechanical Properties.....	68
	Surface Property.....	70
	Parametric Study: Scratch Visibility.....	72
	Concluding Remarks.....	75
VI	RUBBER ELASTICITY.....	76
	Rubber Network.....	76
	Entropy of a Rubber Chain.....	80
	Entropy of a Rubber Network.....	82
	Strain Energy of a Rubber Network.....	82
	Gaussian Rubber Network Model.....	84
	Non-Gaussian Rubber Network Models.....	88
	Entropy and Strain Energy of Non-Gaussian Rubber Network.....	89
	Comparison between Gaussian and Kuhn-Grün Functions.....	90
	3-Chain and 8-Chain Non-Gaussian Models.....	91
	Evaluation of Inverse Langevin Function.....	94

CHAPTER	Page
Stress-Stretch Constitutive Equations.....	98
Stress-Stretch Constitutive Equations for Gaussian Model	101
Stress-Stretch Constitutive Equations for 3-Chain Non-Gaussian Model	101
Stress-Stretch Constitutive Equations for 8-Chain Non-Gaussian Model	102
Numerical Implementation of Rubber Models	103
Mixed Rubber Elasticity Model	106
Material Subroutine for ABAQUS®	109
Concluding Remarks.....	114
VII CONCLUSION AND FUTURE RESEARCH PLAN.....	115
Closure to Present Scratch Research.....	115
New Scratch Research Directions.....	117
First Research Goal: A More Representative Material Constitutive Law	118
Second Research Goal: Experimentation	119
Third Research Goal: Damage Criterion.....	120
Fourth Research Goal: To Perform a More Accurate and Complete FEA	122
REFERENCES	124
APPENDIX A.	133
VITA	159

LIST OF TABLES

TABLE		Page
1	Files for transferring between static and dynamic analysis for ABAQUS®	26
2	Mesh information for FE Meshes A – E	29
3	Mechanical and surface properties of Material Types I – II	31
4	Load Cases A – D	36
5	Loading conditions for experimentation and FEA	44
6	Scheme of parametric study for scratch performance	67
7	Parameters for Gaussian, 3-chain and 8-chain rubber network models	106

LIST OF FIGURES

FIGURE		Page
1	Research publications on scratch study of polymers from 19 th to 21 st century	3
2	Considerations and factors for the scratch study of polymers	5
3	Various steps involved during a scratch process (load-controlled) ...	7
4	True compressive stress-strain curves of PP for various strain rates [6]	8
5	Experimental setup for scratch test	16
6	FE mesh (Mesh A) and the indenter surface	27
7	FE Mesh A and its adaptive remeshing domain (with darker shading)	35
8	Scratch depth profiles for Meshes A – E at the end of the scratch process ($\mu_a = 0$)	37
9	Scratch depth profiles for Meshes A – E at the end of the scratch process ($\mu_a = 0.3$)	39
10	CPU time for Material Types II and III: (a) $\mu_a = 0$; (b) $\mu_a = 0.3$...	39
11	Scratch depth profiles using various time steps and Mesh D ($\mu_a = 0$)	40
12	von Mises stress profiles using various time steps and Mesh D ($\mu_a = 0$)	41
13	Comparison of scratch widths for different load cases	45
14	(a) Undeformed section; (b) section is compressed and squeezed upwards; (c) section is pushed to the side; (d) a scratch groove is formed	47

FIGURE		Page
15	Maximum principal stress profiles and the positions of the indenter at various stages of the scratch process	48
16	Direction of maximum principal stress in the elements around the indenter (Load Case B) (a) perspective in 2-3 plane; (b) perspective in 1-3 plane.....	49
17	Maximum envelope of von Mises stress for different load cases along the scratch path	52
18	Maximum envelope of equivalent plastic strain for different load cases along the scratch path	53
19	Pressure and maximum principal strain contour plots at four different time intervals (a – d) (Load Case A)	55
20	Maximum envelope of equivalent plastic strain along the scratch path	57
21	Maximum envelope of volumetric strain along the scratch path	58
22	Tangential force acted on the indenter during the scratch process	59
23	Scratching coefficient of friction along the scratch path (Load Case B)	59
24	Southwell plot of the scratching coefficient of friction	61
25	Variation of reaction forces with (a) elastic modulus; (b) yield stress; and (c) Poisson's ratio	69
26	Stress-strain diagram to illustrate the effect of changing (a) elastic modulus and (b) yield stress for change in strain energy ..	70
27	Variation of reaction forces with the coefficient of adhesive friction.....	71
28	Interaction between indenter and substrate and forces acting on the indenter	72
29	Variation of scratch depth profiles with (a) elastic modulus; (b) yield stress; and (c) Poisson's ratio	73

FIGURE		Page
30	Stress-strain diagram to illustrate the effect of changing (a) elastic modulus and (b) yield stress for elastic recovery	74
31	Chemical structure of poly-isoprene (natural rubber) and chemical cross-linking due to vulcanization.....	78
32	Flow chart for the formulation of the constitutive relations of rubber	79
33	Conformation of a rubber chain in Cartesian space.....	81
34	Bell-shaped curve of the Gaussian function ($b = 1$)	85
35	Stretching of the unit continuum cube	86
36	(a) 3-chain rubber model; (b) 8-chain rubber model	92
37	Inverse Langevin function and its singularity at $x = 1$	94
38	Comparison of percentage error in approximation over (a) $0 \leq x < 1$; (b) $0 \leq x \leq 0.7$	97
39	Nominal stress-stretch curves of rubber under (a) uniaxial extension; (b) shear.....	105
40	Prediction of stress-stretch behavior by the Gaussian, 8-chain and mixed models	108
41	Stress-stretch curves of 8-chain rubber model by ABAQUS [®] and Eq. [41] in (a) uniaxial and (b) shear.....	112
42	Stress-stretch curves of 8-chain rubber model by ABAQUS [®] and the mixed model in (a) uniaxial and (b) shear	113
43	Scratch machine for scratch testing	120
44	(a) OM image of a scratch profile [74]; (b) SEM image of scratch damage; (c) interferometer image of a scratch groove [75]	120

FIGURE		Page
45	Indentation depths versus normal load for Mesh D and Material I ($\mu_a = 0$).....	147
46	Indentation depths versus normal load for Mesh D and Material I ($\mu_a = 0.3$)	148
47	Indentation depths versus normal load for Mesh D and Material I ($\mu_a = 0.6$)	148
48	Indentation depths versus normal load for Mesh D and Material II ($\mu_a = 0$)	149
49	Indentation depths versus normal load for Mesh D and Material II ($\mu_a = 0.3$).....	150
50	Indentation depths versus normal load for Mesh D and Material II ($\mu_a = 0.6$).....	150
51	Indentation depths versus normal load for Mesh D and Material III ($\mu_a = 0$)	151
52	Indentation depths versus normal load for Mesh D and Material III ($\mu_a = 0.3$).....	152
53	Indentation depths versus normal load for Mesh D and Material III ($\mu_a = 0.6$)	152

CHAPTER I

INTRODUCTION

This study is concerned with the analytical and numerical examination of the mechanical response of polypropylene (PP) under scratch deformation by a semi-spherical indenter. The goal of this study is to apply fundamental mechanics to solicit a good understanding of the damage process, damage modes and their mechanisms on the PP substrate during a scratch process. The finite element method (FEM) is employed as the analysis technique and ABAQUS[®], a commercial FE analysis package is utilized to perform the analysis. Using a numerical approach, parametric studies are executed to evaluate the importance of material and surface parameters to aid engineers in designing better scratch-resistant products.

In this chapter, introductory remarks are made to highlight the significance of scratch research and review its current status. Important factors and considerations defining the scopes of scratch study are evaluated in detail to give an appreciation of the inherent complexity in research. Finally, an outline is provided to lay out various research components and their arrangement in the dissertation.

SIGNIFICANCE OF SCRATCH RESEARCH

Good surface quality is a prime attribute that both manufacturers and consumers aspire to have in consumer products, either for the sake of functionality or mere

aestheticism. While producing a desired surface finish has its own level of difficulty, the sustainability of a good surface quality over its service life poses the real challenge.

For polymer applications, the concern over surface quality can be broadly classified into surface aestheticism, integrity and durability. For surface aestheticism, one can easily find its relevance in many products such as automotive parts, electronic and telecommunication devices. For these products like car dashboards and cellular phones, surface scratches merely reduce the original product attractiveness while their intended functionality remains largely unaffected. As for applications like food packaging, retaining surface integrity of packaging materials becomes an important issue. Scratches formed on packaging films can render them to tear, which may in turn lead to product damage. On the other hand, surface durability is sought after in the coating and data storage industries. In coating applications, an exposed surface may lead to corrosion or damage of the underlying substrate. Hence, coatings are desired to be intact for as long as the product remains in its service life. Such surface durability is also emphasized in the data storage industry, where unrecoverable data from scratches on hard disks and optical storage devices can cause companies and individuals considerable resources and valuable man-hours.

Much neglected by many but probably as important is the genuine structural concern of scratches. Surface scratches can act as stress concentration *hotspots* that reduce the load carrying capacity of products over time and ultimately lead to their premature fracture and failure.

REVIEW OF SCRATCH RESEARCH

In view of the above discussion, it is evident that scratch study is important to many industries. However, surface concern for polymer applications has come into existence only over the last few decades and is gaining its importance together with advances in polymer science and technology. This trend of research interest can be appreciated from Figure 1¹, which shows the number of research publications related to scratch studies of polymers since the late nineteenth century. One can see that little research effort was put in before the nineteen-eighties; after this time, there has been a surge of research interest over the last two decades.

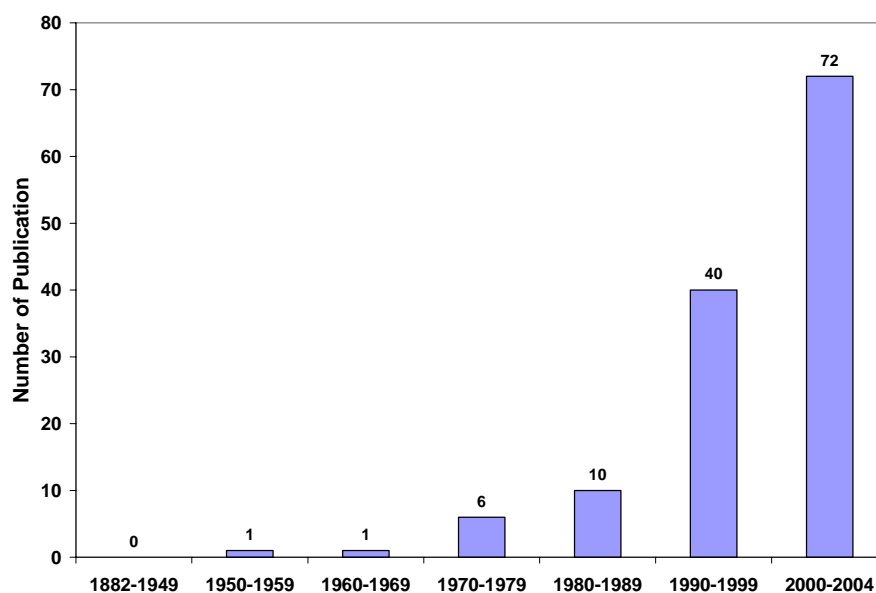


Figure 1: Research publications on scratch study of polymers from 19th to 21st century.

¹ The results presented are based on the Compendex[®] engineering journal database using keywords “scratch” and “polymer”.

Unlike works on traditional materials such as metals and ceramics that enjoy a longer research history, the scratch study of polymers still remains in its early phases, which limits the amount of understanding. Besides being a relatively new research area, there are several inherent issues leading to its slow progress. Firstly, there is a lack of standardized test methods and equipment to administer scratch experiments on polymers. Testing standards for scratches have only appeared in 2003 for ASTM [1] and 1997 for ISO [2-3], which are themselves more suitable for ceramics and mar study, respectively. Due to the absence of standardized testing methods, researchers began to develop their own scratch testing equipment to perform experimentation. One can refer to the paper by Lim et al. [4] for a compendious list of scratch equipment used by various researchers. As a result, the knowledge gained is specific to the test equipment, experimental conditions and materials. Secondly, the way to evaluate scratches also varies with researchers, ranging from using the subjective human eyesight to more objective optical devices like scanners. These limitations in scratch testing and evaluation unfavorably lead to a difficult situation for researchers where they have been unable to compare and verify experimental results. This inevitably hinders the progress of scratch research.

However probably the most important factor of all is the level of complexity involved in the fundamental study of scratch behavior of polymers. To further our understanding of the scratch behavior of polymers, it is necessary to examine the underlying material science and physics (mechanics) of the problem as well as their inter-relationships. To appreciate the complexity of scratch research of polymers, one can refer to Figure 2 that lists the important considerations and factors for this study.

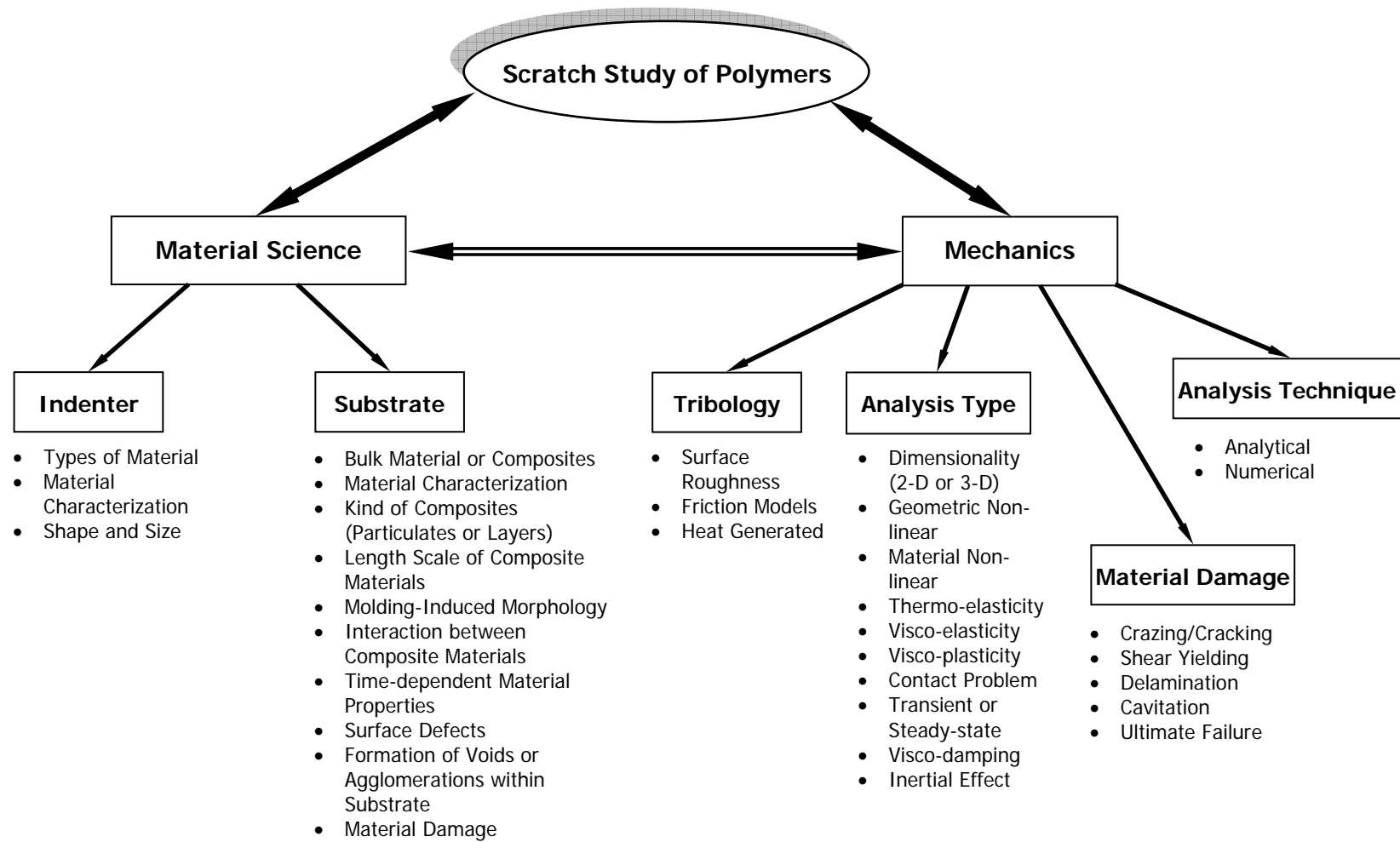


Figure 2: Considerations and factors for the scratch study of polymers.

Due to the nature of the problem, delving into the mechanics of the scratch response of polymers entails a rigorous treatment of several components, *i.e.*, tribology, type of analysis, material damage and analysis technique. During a scratch process, surface interaction between the object (indenter) and scratched material (substrate) takes place. Unless perfectly smooth surfaces can be produced, surface interaction inherently produces friction and consequently heat. For the tribological study of a scratch process, it is necessary to describe the surface roughness property and adopt a suitable friction model. For now, the most straightforward approach to treat friction is to assign a coefficient of adhesive friction, μ_a to the interacting surfaces and obtain the frictional force, F based on the Coulomb's friction model [5] as

$$F = \mu_a N \quad (1)$$

where N is the normal force. Tribology, the study of interacting surfaces and friction, has been intentionally considered separately from the types of analysis so as to highlight its uniqueness in the scratch study. Shown in Figure 3, as an indenter pushes into the substrate by means of controlled normal force or displacement and traverses across the substrate, the indenter no longer just interacts with the top surface of the substrate. With the exposure of underlying materials from scratch damages, the indenter also comes into contact with the sub-surface and core of the substrate. This introduces additional complexity to the study as the coefficient of adhesive friction can no longer be used to describe the frictional property of the sub-surface and core. It is to be expected that as the material ruptures under scratching, the surface roughness of the substrate is increased and so does the frictional force. Such a unique change in the frictional response for the

scratch problem has hitherto not been reported or considered with importance in any research findings.

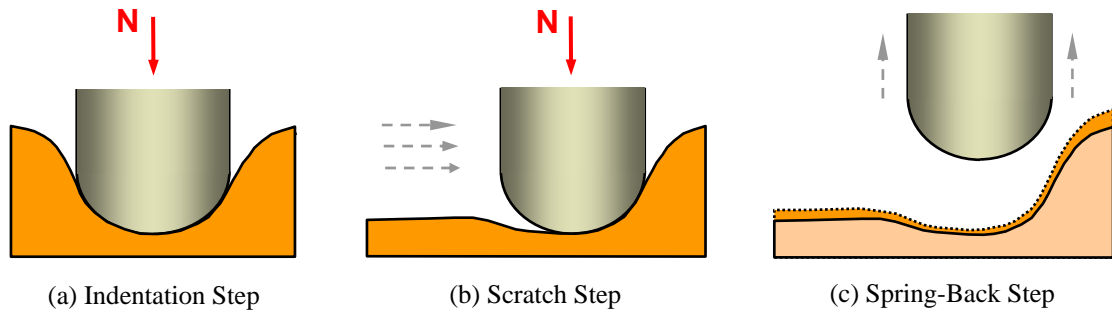


Figure 3: Various steps involved during a scratch process (load-controlled).

On the analysis types for scratch research, the dimensionality of the problem needs to be reviewed. Depending on the considered scratch problem, appropriate simplifications can be introduced to reduce the dimensionality from the challenging three-dimensional problem to simpler two-dimension, plane-stress, plane-strain, or other formulations. Simplifications to the problem can also be in the form of reducing the geometrical size of the analysis domain due to the presence of axial or plane symmetry. Also geometrical large deformations encountered in scratched materials demands the use of non-linear strain measure in the analysis, instead of simpler small-strain theory.

As PP is the material of concern in this scratch study, proper considerations must be made in the analysis to capture the correct mechanical response of the material. Depending on the types of polymers and the extent of deformation, polymers respond to deformation differently with time, temperature, stress state (tension or compression) and

strain rates and may strain-harden and/or strain-soften. Presented in Figure 4 from the work of Arruda et al. [6], the stress-strain response of PP is non-linear, even in the elastic range and varies for different strain rates.

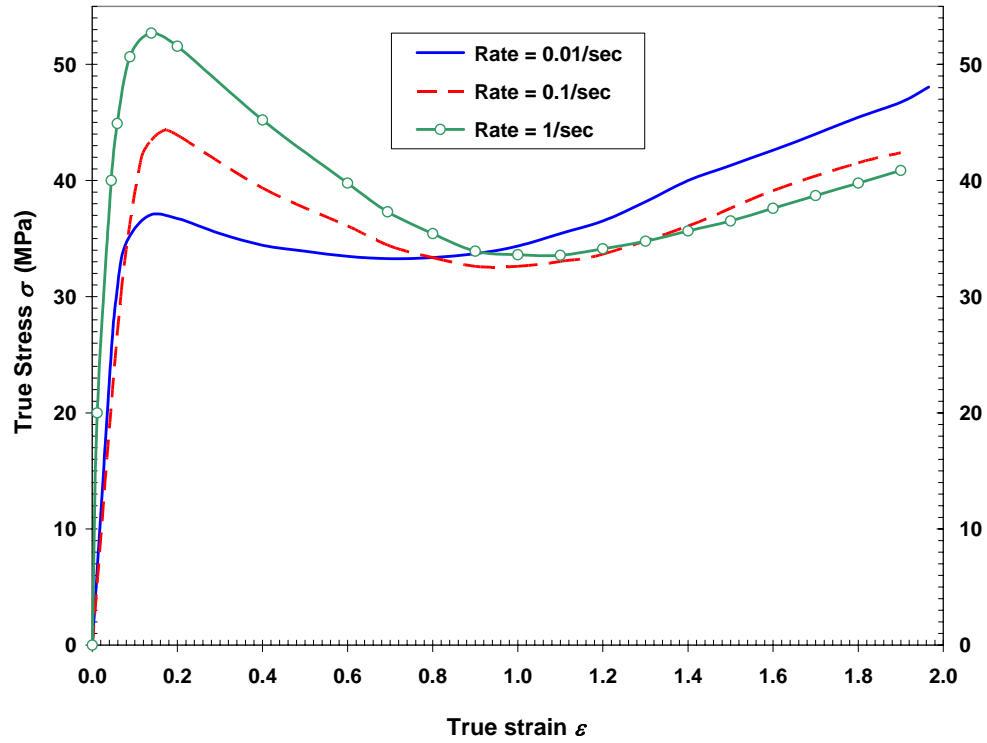


Figure 4: True compressive stress-strain curves of PP for various strain rates [6].

In view of material needs, the scopes of a scratch analysis should cover material non-linearity, viscoelasticity and thermo-elasticity. As scratch deformation may occur beyond initial material yielding, scratch analysis should also account for plasticity or viscoplasticity. For the dynamical nature of the scratch process, the inertia, stiffness and visco-damping of the system need to be identified. Moreover depending on the scratch

speed and length, the dynamical response of the system should be assessed carefully if it remains as transient throughout the analysis or settles into a steady-state response at some point during the process.

The next crucial factor in the scratch mechanics is to have an adequate description of the material damage for polymers. It is well-known that bulk or homogeneous polymers, when deformed, can yield in shear or undergo crazing/cracking, depending on the type and extent of deformation. Making the damage prediction more challenging is the fact that the two failure modes can coexist together, even though there may be a dominant mechanism between the two. In a scratch process, stress flow in a material can change drastically from tension to compression as the indenter plows across the substrate; this will be highlighted in the results presented in Chapter IV. This may in turn induce a change of one failure mode to another at a material point, before and after the scratch deformation. Hence to account for such failure behavior, there is a need of a criterion to allow the two failure mechanisms to compete for dominance. A monitoring scheme should also be incorporated to follow the change of the failure mechanism and transfer the stress flow to neighboring material points once damage occurs at a material point. The treatment of material damage becomes more challenging for polymer composites since the composite arrangement can be layered, *e.g.*, coated system, or particulated, *e.g.*, rubber-modified polymers. Depending on the adhesive strength between the matrix and fillers, delamination or cavitation may occur locally at the interfaces. The ability to identify these local failures is equally important since the

integrated load-carrying capability of the damaged composite may be affected and its overall failure mechanism may also change.

The final link to close the chain for the scratch mechanics is to provide a solution tool for analyzing the problem. To any well-posed mechanics problem, researchers in general seek to furnish solutions, either by using analytical means or numerical tools. Analytical approaches are typically possible for simpler cases and become increasingly prohibitive to yield results for large and complicated problems. A closed-form analytical solution has the advantage of providing valuable insights on the influence of the critical parameters to the problem. Numerical techniques, on the other hand, are normally built on the foundations of analytical approaches and attempt to solve problems through approximation or discretization of geometry, domain, temporal and spatial derivatives; common available numerical techniques are finite difference [7] and finite element method [8]. More versatile than analytical approaches, numerical techniques permit one to formulate several physical phenomena and incorporate unique material response into a single analysis. As a result of the approximation and discretization, numerical techniques generally possess a mathematical framework that is well-suited for large-scale computer implementation. With the advent of modern computers, numerical techniques are now often preferred by researchers. However, there are disadvantages that are associated with numerical techniques. A major drawback of adopting numerical techniques is the fact that the results generated are approximations to the exact solutions. To improve the accuracy of numerical techniques, ad-hoc remedies, such as finer discretization, have to be introduced. Another short-coming is that the numerical

techniques are usually cumbersome for parametric studies, since a series of runs is needed to establish the influence of a single parameter on the problem. These two disadvantages often translate into long computational times and demand excessive computer resources such as disk space and memory. Regardless of the choice of an analytical or numerical approach, there are inherent considerations in each of these approaches that need special attention so that the analysis can capture the essential physics of the scratch problem and generate results that lead to a better understanding of the topic.

DISSERTATION LAYOUT

As mentioned earlier, a numerical approach is employed in this dissertation to understand the scratch problem and finite element method is selected as the solution tool. To further develop the background of scratch research, a compendious literature review of the topic is given in Chapter II. An overview of research strategies adopted in the dissertation is also highlighted in this chapter. In Chapter III, various physical and computational considerations for implementing a finite element analysis (FEA) of the scratch problem are carefully laid out, together with verification exercises to assess the correctness of the commercial software, ABAQUS[®]. Based on the adopted FEA, numerical results generated to examine the evolution of strain and stress states during the scratch process are reviewed in Chapter IV. Using the furnished numerical results, a phenomenological deduction of the scratch damage mechanism and the prediction of craze initiation is discussed. The existence of shear yielding and crazing and their likely

competition in a scratch deformation is also studied in this chapter. Next in Chapter V, a parametric study to examine the influence of material and surface properties on scratch performance of polymers is presented. An introduction of the dual definitions of scratch performance is also provided in this chapter. In Chapter VI, a formal discourse on the material constitutive modeling for rubbery and amorphous polymers is made. This outlines a preliminary effort in providing a more realistic material law for the scratch analysis. Concluding remarks to summarize scratch research findings and an introduction of new scratch research directions and extensions is given in Chapter VII. Finally in the last chapter (Chapter VIII), citation of referred literature in the dissertation is documented. Derivations and results, that are non-essential but complementary to the chapters, are collected in the appendices of the dissertation.

CHAPTER II

LITERATURE REVIEW AND RESEARCH SCOPE

Over the last two decades, scratch behavior of polymers has gradually become an important research topic in both the academic and industrial world. Although it is crucial to identify the key considerations and scopes of scratch research, it is equally essential to be familiar with the current state of knowledge in the field. With this understanding, a more cohesive research strategy can be contrived to apply the existing knowledge to address the various needs of scratch research. Hence in the next section, the state of scratch research is reviewed. Subsequently, the important topics of study to be adopted for this dissertation are introduced accordingly.

LITERATURE REVIEW

A literature review of research activity in scratch mechanics reveals that in the early stages, researchers often had to rely on accumulated knowledge gained from indentation studies and proposed scratch research methodologies accordingly. In the seminal work of Hertz [9], closed-form linear elastic solutions were developed for static indentation problems. This marks the emergence of a new field in mechanics, now commonly known as *contact mechanics*. Subsequent works have been conducted to extend the scope of the Hertzian indentation problem to include the action of tangential stress due to sliding friction [10-20] between isotropic bodies. However, these analyses are still essentially linear elastic and hence cannot sufficiently describe the large

deformation experienced by the material during a scratch. Moreover, the results of static analyses can, at most, be applied to the instant when a body is about to slide over another body. Research efforts that essentially treat dynamic aspects of the scratch problem can be attributed to Churilov [21,22], Rahman [23] and Brock [24]; again, they are limited to a linear elastic study of isotropic materials. For viscoelastic materials, Lee and Radok [25] and Hunter [26] considered the Hertzian indentation problem for a rigid spherical punch. During a scratch process, a material may deform plastically under extensive straining and such plastic flow should be considered in the analysis. Probably due to the inherent nonlinearity, there has been hitherto no analytical work to consider the plastic yielding of materials under indentation or sliding. While the above-mentioned works are valuable within their own merits, it is evident that most of these works are limited in the material description and scope of analysis for a more comprehensive study of scratch behavior of polymers.

For numerical techniques, the computational approach commonly adopted by researchers for the scratch problem is the finite element method (FEM) [8]. Even so, research efforts on this topic using FEM remain scanty and most of these works are also restricted to the study of indentation (see the well-compiled bibliography by Mackerle [27]). Tian and Saka [28] investigated elastoplastic and plane-strain behavior of a layered substrate of bilinear materials under normal and tangential contact stresses using a commercial finite element (FE) package, ABAQUS[®]. Their analysis however did not account for dynamic effects of the moving indenter, and contact between the indenter and substrate was not modeled. Another work that utilizes ABAQUS[®] for analysis is by

Lee et al. [29], who modeled a steel ball scratching a rotating polycarbonate disk. While the material law adopted for the polycarbonate substrate is more realistic, the authors over-simplified a three-dimensional (3-D) problem to a two-dimensional plane-strain problem, rendering their FE analysis (FEA) to be non-applicable to their original problem, as noted by Wong et al. [30]. Bucaille et al. [31] and Subhash and Zhang [32] executed 3-D simulations of a displacement-controlled scratch deformation by a smooth rigid conical indenter on an elastic-perfectly-plastic and bilinear material, respectively. Their 3-D FEAs are however unsuitable to study the scratch response of polymers since the material rheology adopted cannot capture the strain hardening and softening nature of polymers.

RESEARCH SCOPE

Learning from these earlier research efforts and the discussion of various requirements of scratch research in Chapter I, there are several attributes that the mechanical analysis of the scratch problem should possess for a comprehensive study. To begin with, it is clear from the previous section that a numerical approach is more suitable to perform the scratch analysis than an analytical approach. Among different numerical techniques, FEM is selected for the current study due to its versatility to accommodate various physical phenomena like surface contact, frictional interaction, and atypical material responses. In this study, the scratch problem of concern is to investigate the mechanical response of polypropylene (PP) under the scratching action of

a semi-spherical tipped indenter. For this scratch study, the research emphasis is focused on:

- understanding how different scratch conditions can affect scratch behavior of PP
- examining phenomenological damage process and mechanism of scratches
- predicting the initiation of crazes during a scratch process
- assessing the influence of material and surface properties on the scratch response.

To meet the research goals, it is essential to ensure that the formulation of FEA undertaken in the study possesses the correct attributes. Key attributes of FEA to be covered in this research endeavor are summarized below.

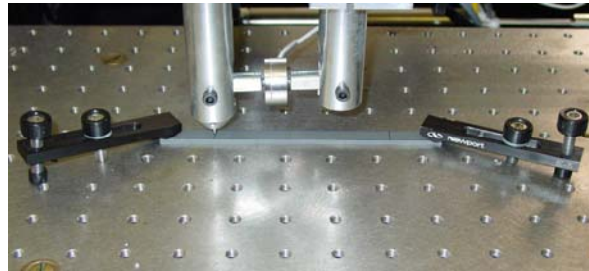


Figure 5: Experimental setup for scratch test.

- (a) **3-D Dynamic Analysis.** In the experimental setup that is to be numerically simulated (see Figure 5), the PP specimen is 12 cm long, 1 cm wide and 3 mm thick while the diameter of the indenter tip is 1 mm. For numerical simulation, the analysis should remain 3-D as the analysis or computational domain is too

complex to allow for simplification to a 2-D, plane stress or plane strain formulation. To study the transient response of scratch problem, dynamic analysis should be executed to simulate the scratch process accordingly.

(b) **Contact and Frictional Interaction.** As surface contact between the indenter and substrate is ubiquitous during scratching, its interaction is to be featured in the scratch analysis. As incorporated, the analysis needs to provide a reasonably accurate understanding of the influence of surface contact on the problem. Frictional interaction between contacting surfaces is another important integrated phenomenon in the scratch process. The special case of frictionless contact will also be considered in this study to discern the frictional effect on the scratch problem.

(c) **Geometrical Non-linearity.** During the scratch process, the substrate material undergoes large geometrical changes. For FEA, such geometrical nonlinear deformation can be accounted for by adopting non-linear strain measures. As a result of large deformation, the FE mesh may undergo severe distortion and this leads to convergence problems for FEA. To ensure numerical convergence in the FEA, remeshing of the computational domain is required to preserve the quality of the FE mesh.

(d) **Material Model for Polymers.** Selection of an appropriate material constitutive model is a key factor for the analysis of any deformation process to capture the true representation of the material response. The constitutive law

considered for PP should take into account strain-softening, strain-hardening and rate-dependent characteristics of the material.

- (e) **Damage Criterion for Polymers.** To account for plastic flow during the scratch process, yielding criterion and associated hardening rule need to be featured in the analysis. Crazing, the other dominant damage mode of polymers, should also be considered in the study. This is done by subjecting the numerical results to suitable criterion to predict its initiation.

To implement all the above attributes in FEA, it will be a daunting research undertaking if each of these attributes is to be built or *reinvented* from ab initio. By adopting a commercial FEA package like ABAQUS[®] which has most of the features incorporated, time and research effort can better be spent on executing the analysis and studying the numerical results. Detailed discussion on how various scratch analysis attributes are being fulfilled in ABAQUS[®] is duly presented in Chapter III. The scopes of study put forth above are in line with a key assumption made in this study, *i.e.*, heat from external sources or generated due to scratching or inelastic straining has been neglected. In essence, all scratch FEAs conducted in this work do not account for thermal effects.

As highlighted above, a suitable constitutive model is an important key to predicting an appropriate material response to a mechanical deformation. While there have been considerable efforts to include an appropriate material law for FEA in this study, the constitutive law adopted using the experimental stress-strain curves (see

Figure 4 in Chapter I) may be insufficient to respond to a complex mode of deformation like a scratch. As presented in the later chapters, this inadequacy in the material model is shown through a lack of quantitative correspondence between the computed numerical and experimental results. To address this issue, additional research effort is put in this work to look into the material constitutive modeling of polymers. As PP is semi-crystalline in nature and has a varying degree of crystallinity and various crystal structures [34], studies related to modeling the constitutive response of such complex materials are difficult to find in the open literature. Since the amorphous phase of PP is similar to elastomeric materials in terms of their rheological structures [34], the secondary effort of this research is focused on elastomeric or rubbery materials. The knowledge gained from this effort lays the foundation for future development of polymer surface study as well as material constitutive modeling of amorphous polymers and elastomers.

Rubber, a common elastomer, is well understood and researched for its hyperelastic response. From the open literature, there are a handful of constitutive theories that have been proposed, which can generally be classified into the statistical network theories and phenomenological theories. Depending on the choice of probability density functions, statistical network theories can be further sub-divided into Gaussian and non-Gaussian. Using the Gauss or normal density function [35] to statistically describe the spatial configuration of randomly oriented rubber chains, the developed constitutive theory is commonly known as the Gaussian or neo-Hookean model [36]. The Gaussian network model is known to have a good prediction of the

stress-strain behavior of vulcanized rubber under uniaxial tension, shear and biaxial deformation at small strains [36-38]. At large deformation, the non-Gaussian effect of chain stretch needs to be accounted for in order to give an accurate prediction of its mechanical behavior. Of all, the non-Gaussian density function proposed by Kuhn and Gr \ddot{u} n [36] has been commonly adopted by several researchers [34, 39-42] to establish the 3-chain [39], 4-chain [40], 8-chain [41], full-chain [34] and averaged-stretch [42] network models for rubber. In development of the Gaussian and non-Gaussian network theories, it has been assumed that the material is incompressible. Considering the compressibility of elastomers in the constitutive modeling of rubbers, the work by Bischoff et al. [43] and Kaliske and Rothert [44] are particularly noted. In the work of Bischoff et al. [43], the different ways of including the condition of compressibility in the formulation of constitutive theory is reviewed. The work by Kaliske and Rothert [44] to model volumetric changes in a material during a deformation process has been adopted in ABAQUS[®].

From the independent study that is presented in Chapter VI, the incompressible non-Gaussian network theories generally model large strain response of rubber well but their predictive capabilities are not superior to those of the Gaussian model at low and moderate strains. Reviewing the various rubber models, a new mixed network model between the Gaussian and eight-chain non-Gaussian models is proposed. This mixed model inherently preserves the good predictive power of these two models and yields good predictions over a wide range of deformation. It is also highlighted in this chapter

that the performance of the mixed model is better than the three- and eight-chain models as well as the rubber network model adopted by ABAQUS[®].

CHAPTER III

FINITE ELEMENT MODELING

As outlined in Chapter II, there are essentially four main focuses for the numerical effort in modeling the scratch problem. Based on polypropylene as the material of research, the four focuses are (i) to understand the influence of various scratch conditions on the scratch response of the material, (ii) to examine the phenomenological damage process and mechanisms of scratches, (iii) to predict craze initiation, and finally (iv) to understand the effect of material and surface properties on scratch performance. Finite element method (FEM) is chosen as the numerical technique to handle the complicated aspects of the scratch problem while ABAQUS[®], a commercial finite element package, is adopted to perform the required numerical analyses. Using commercial software in this work helps to save precious research hours and manpower that may otherwise be spent in developing computer codes. However, there are new challenges on the analysis implementation when adopting commercial software like ABAQUS[®], since commercial software are mostly developed to provide a *black-box* for the convenience of end-users. To achieve research goals outlined above, it is therefore important to ensure that ABAQUS[®] can be executed correctly to perform reliable and accurate finite element analysis (FEA) for the scratch problem. A prime concern for all numerical modeling effort of mechanical problems is how well the numerical model can account for the key physical aspects of the problem, which in turn translates to how closely the generated solutions can represent the state of reality. To

duly accommodate these modeling needs, this chapter discusses the important physical considerations of the scratch problem and associated computational issues. Relevant numerical studies conducted to evaluate computational needs are also presented.

PHYSICAL AND COMPUTATIONAL CONSIDERATIONS FOR FE MODELING

When an object (indenter) makes contact and traverses across the surface of another material (substrate), thereby making a scratch, the entire scratch process necessitates consideration of several physical and material factors. Based on contact mechanics for indentation [9], the shapes of the indenter (*e.g.*, spherical, conical and others) result in vastly dissimilar stress fields and different surface damage modes [45]. Size of the indenter determines the scale of damage, from nanometer to millimeter. Since this work focuses on mechanical response of a PP substrate that is scratched by a stainless steel ball indenter with a diameter of 1 mm, the deformation essentially remains in the millimeter range. Besides the indenter, the geometry and shape of the substrate and the relative material property of the indenter and substrate directly influence the extent of scratch damage. Detailed discussion is provided in the subsequent sections on how these factors and various computational concerns are included in the FEA.

Analysis Steps of a Scratch Deformation

To model a scratch process, it is helpful to envision how a scratch occurs in an actual experimental setup. A scratch process can be separated into three mechanical

steps (see Figure 3); the first is the indentation step whereby the indenter makes an indentation onto the substrate *via* a specific normal load or displacement. In the second scratch step, the indenter ploughs through the top surface and subsurface of the substrate and pushes or removes materials along the scratch path. For the final step, the indenter, having come to a stop at the end of the scratch, is then lifted up from the scratch groove, thereby allowing elastic recovery to take place in the substrate. This last step is commonly known in the metal-forming industry as *spring-back*.

Dynamic Analysis of Scratch Step

Due to the dynamic nature of the scratch step, a dynamic analysis is required. An immediate concern of dynamic analysis is the analysis time and the resulting scratch speed of the indenter for a specified scratch length. It is always ideal for simulations if their analysis can be performed over a time interval that mimics the actual physical process. Depending on the nature of the problem, the geometry, the type and size of element of the FE mesh, executing a realistic FE dynamic analysis can be time consuming and demands large computer resources.

In the formulation of dynamic analysis by ABAQUS® [46,47], an explicit scheme is employed to describe the time evolution of the independent variables. For the analysis, ABAQUS® determines an appropriate time increment for every time step to ensure the stability of the time integration scheme. To achieve a desired level accuracy of the dynamic analysis using an explicit scheme [8], it may be necessary to consider the use of time increments that are smaller than the stable increments. For this purpose, a

numerical study is conducted to assess the need of adopting smaller time increment for dynamic analysis of the scratch problem.

Static Analyses of the Indentation and Spring-Back Steps

Both the indentation and spring-back steps are not controlled in terms of time and take a longer time scale for completion. This is because during indentation (see Figure 3), the loaded indenter may have seated on the specimen for a while prior to scratching and the analysis of the surface damage does not follow immediately after the spring-back. Therefore, it is more appropriate to perform static analyses for these two steps. In this study, the indentation step is intended to be load-controlled, *i.e.*, indentation is caused by a driving normal load acted on the indenter. However due to the limitation of the contact algorithm of ABAQUS® [46], a firm contact has to be established first before a load can be specified correctly on the indenter. To do this, the indentation step is further divided into two steps [48]. In the first step, a displacement boundary condition is specified to push the indenter vertically onto the substrate and the normal reaction force is noted; the indentation depth is changed and another static analysis is performed. This iterative process repeats until it produces the desired normal reaction force. Once the desired force has been achieved within an acceptable tolerance, the displacement boundary condition is then replaced by a normal load of the same magnitude as the reaction force in the second step. For the spring-back step, it can be executed readily by prescribing a displacement boundary condition to move the indenter away from the surface of the substrate, thereby removing any contact with the substrate.

It is noted that in Chapter V where parametric studies are reported for the current scratch research, the scratch analysis performed is displacement-controlled, rather than the above-mentioned load-controlled. To reduce analysis time, dynamic analysis is considered for all three steps: indentation, scratch and spring-back.

Importing/Exporting between Static and Dynamic Analyses in ABAQUS®

Though ABAQUS® has been structured to allow users to transfer analysis data between static and dynamic analysis, there are salient points from the perspective of FE analysis and mechanics that need attention so that the intended analysis is performed with a certain level of accuracy.

Table 1: Files for transferring between static and dynamic analysis for ABAQUS®.

From Static to Dynamic Analysis	From Dynamic to Static Analysis
*.mdl, *.prt, *.res, *.stt	*.abq, *.pac, *.prt

Firstly, the same non-linear strain measure should be used for both static and dynamic analysis. To have a consistent comparison of variables across different analyses, the original undeformed configuration of the substrate shall be taken as the reference configuration and should not be updated in the new analysis. However, material state variables, like the equivalent plastic strain, should be updated so that the plastic flow of the material remains continuous across analyses. As required by

ABAQUS®, rigid surfaces and their surface interaction properties from the previous analysis have to be redefined if they remain applicable to the new analysis. Hence, contact and boundary conditions are required to be re-established in the new analysis. To facilitate a successful transfer of the data and model information between analyses, restarting files are generated in the current analysis for exporting to the next analysis. Table 1 lists the types of files that are needed to transfer between static and dynamic analyses for ABAQUS®. For this scratch study, ABAQUS® input files for static and dynamic analyses can be found in Appendices A-1 and A-2, respectively.

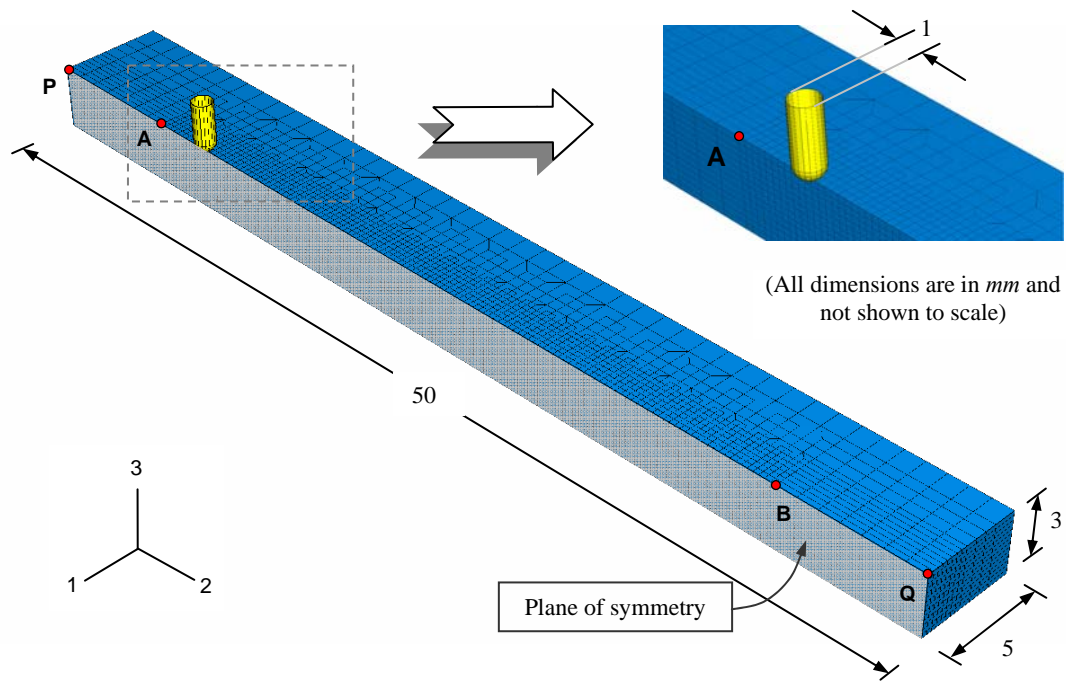


Figure 6: FE mesh (Mesh A) and the indenter surface.

FE Mesh: Geometry, Element Type and Boundary Conditions

To simulate actual experimental conditions given in [49,50], dimensions of the FE mesh follow as closely as possible to those of experimental test specimens and are taken to be 50 mm by 10 mm by 3 mm. But, compared to the test specimens, the length of the FE mesh has been reduced to decrease computational time. Due to the plane of symmetry of the problem, one can reduce the width of the original mesh by half, as indicated in Figure 6.

To perform a 3-D analysis of the scratch process, 3-D linear eight-node solid elements (C3D8R) with selective reduced integration and hourglass mode control [46,47] are utilized for their meshing simplicity. Elements with selective reduced integration are chosen for a more accurate representation of the average strains in the elements, which is beneficial for the calculation of constitutive behavior for highly non-linear materials like polymers. But due to the reduced integration, hourglass mode control is required to numerically arrest undesirable singular hourglass modes in the elements due to the rank deficiency of the stiffness matrix. The hourglass control mode employed by ABAQUS® follows the work by Flanagan and Belytschko [51].

To ensure sufficient surface contact between the indenter and substrate, five mesh designs have been considered for a convergence study. Shown in Figure 6 is Mesh A where there are 128 elements across the critical length (A-B) over which the scratch path lies. The critical length (A-B) of 36 mm is measured along the length of substrate at 7 mm from its both ends. Table 2 shows the detailed mesh information for the five different meshes (Mesh A – E). To aid a discussion on the convergence study later in

the chapter, the table also provides the number of undeformed elements over the projected area of the indenter to give a perspective of a sufficient contact. The five meshes are created using a mesh generator written in FORTRAN, which is documented in Appendix A-3.

Table 2: Mesh information for FE Meshes A – E.

Mesh	No. of elements over the critical length	No. of DOF	No. of element over the projected area of the indenter
A	128	64,215	~ 10
B	256	151,110	~ 42
C	384	260,550	~ 96
D	512	391,995	~ 173
E	768	689,310	~ 363

For the indenter, the diameter of its spherical tip is taken to be 1 mm. In Figure 6, the indenter is shown by a cylindrical shaft with a length of 2 mm, with one end defining the spherical tip. The indenter is modeled by an analytical rigid surface whose six degrees of motion are controlled by a reference node while the rigid surface is defined together with a mass element. To isolate the inertia of the indenter from the mechanical response of the substrate, a small value of 5 μg is assigned to the mass of the indenter.

To mimic the clamping of test specimens at both ends [49, 50] (see Figure 5), all nodes on both 1-3 boundary planes of the FE mesh are restrained from movement in all

three directions; the adopted coordinate system is provided in Figure 6. Since test specimens are supported to a rigid surface of the scratch machine, all nodes on the bottom surface are restricted from moving in the vertical 3-direction. To impose the symmetry of the problem, nodes along the plane of symmetry are not allowed to translate in the 1-direction. Since the original mesh has been reduced by one-half due to the symmetry, one should note that all load imposed along the plane of symmetry should be scaled accordingly.

Material Law

The material considered for the substrate is primarily PP. Like most polymers that are viscoelastic in nature, the constitutive behavior of PP varies with strain rate. As material input for FEA, the true compressive stress-strain curve of PP at various strain rates, as shown in Figure 4, has been adopted [6]. This considered rate-dependent material should be referred to as Material I. To enable convergence and for purposes of parametric studies, two additional materials (Material II and III) are considered for the substrate. The material characteristic of Material II is pure elastic while Material III is elastoplastic with no hardening. As listed in Table 3, the mechanical properties adopted for these two materials are noted to follow closely to those of polypropylene (Material I).

In the experimental setup of a scratch test [49,50], the indenter tip is made up of stainless steel, which is more than one hundred times stiffer than PP and its yielding stress is about ten times as much. It is therefore equitable to treat and model the indenter as rigid and this assumption has been adopted for all analyses.

Table 3: Mechanical properties of Material Types I - III.

Material Type	E (GPa)	ν	σ_y (MPa)	ρ (kg/m ³)
I (Rate-Dependent)	1.65	0.40	(see Figure 4)	905
II (Pure elastic)	1.65	0.40	-	905
III (Elastic-fully plastic)	1.65	0.40	35.0	905

Plastic Yielding Criterion

Since most polymers undergo strain softening and hardening at large plastic deformation, it is important to predict the onset and describe the evolution of plastic flow in the analysis. To predict and monitor any plastic deformation in the FE analysis wherever appropriate, von Mises shear yielding criterion [52] is employed. For the von Mises criterion, plastic yielding occurs whenever the second invariant of the deviatoric stress tensor reaches or exceeds the yield stress, as given in Eq. (2)

$$J'_2 = \frac{1}{6} [(\sigma_1 - \sigma_2)^2 + (\sigma_2 - \sigma_3)^2 + (\sigma_3 - \sigma_1)^2] \begin{cases} < \frac{1}{3} \sigma_y^2 (\varepsilon_{eq}^{pl}) & \text{(shear yielding does not occur)} \\ \geq \frac{1}{3} \sigma_y^2 (\varepsilon_{eq}^{pl}) & \text{(shear yielding occurs)} \end{cases} \quad (2)$$

where σ_1 , σ_2 and σ_3 are the principal stresses and σ_y is the axial yield stress that is a function of the equivalent plastic strain ε_{eq}^{pl} . The equivalent plastic strain is the total plastic strain increment over time and defined as

$$\varepsilon_{eq}^{pl} = \int_0^t \sqrt{\frac{2}{3} (\dot{\varepsilon}^{pl} : \dot{\varepsilon}^{pl})} dt, \quad (3)$$

where $\dot{\varepsilon}^{pl}$ is the plastic strain increment tensor and the double dot denotes tensor dot product. To vary the yield stress with the amount of plastic flow according to the material hardening and/or softening, the isotropic hardening rule is utilized [52].

Crazing, Debonding and Cracking Criterion

For polymers, the fracture mechanisms that can lead to stress whitening are crazing, voiding, debonding, and cracking. Particularly for scratch damage, crazing should be treated with the same importance as bulk shear yielding for several reasons. First of all, crazes are highly light-reflective in nature and if present, can increase scratch visibility on materials. Besides being a precursor of brittle cracking and fracture, crazing can occur at lower stress levels than those for bulk shear yielding [53]. Depending on materials, the state of deformation and the operating environment, it is likely that crazing competes against shear yielding to become the dominant fracture mechanism. It is therefore of research interest to study the possible initiation of crazes during a scratch process. The criterion used for assessing craze initiation can also be relevant to evaluate voiding, debonding, and cracking since they involve the same type of stress/strain components, *i.e.*, the critical strain and the maximum hydrostatic tension. Of the various criteria for craze initiation, the critical strain criterion by Bowden and Oxborough [54] is adopted for its sound physical basis and ability to account for a general triaxial state of stress. The criterion states that crazing occurs when the strain in any direction reaches a

critical value and that this critical strain depends on the hydrostatic tension [54,55]; mathematically, this criterion can be described as,

$$\varepsilon_C = A + \frac{B}{\sigma_1 + \sigma_2 + \sigma_3} \equiv \varepsilon_1 \quad (4)$$

where ε_C is the critical craze strain and σ_i ($i=1,2,3$)² are the principal stresses while A and B are time-temperature-dependent parameters. In this study, ε_C is treated to be equivalent to the maximum principal strain, ε_1 .

Contact Algorithm

To establish, track and maintain contact between surfaces during scratching, the contact pair (master-slave) algorithm for finite sliding as provided by ABAQUS[®] [46] was selected for the study. The analytical rigid surface of the indenter is assigned to be the master surface while the slave surface belongs to the top surface of the FE mesh for the substrate. Though the contact pair algorithm may be robust, the FE mesh must still be sufficiently refined to avoid any erroneous over-closure of contact surfaces. Mesh refinement is also crucial to create sufficient contact with the surface of the indenter for an accurate calculation of contact stresses and forces. These two factors provide the motivation or need to perform the convergence study to determine the optimal mesh design from one of the five introduced in Table 2, for the scratch problem at a reasonable computational cost. Double precision calculation is used in the FEA to alleviate any contact noise that may compromise the results.

² The average of the three principal stresses gives the hydrostatic stress.

Surface Interaction

Like any two sliding surfaces, there will be interactions between them that can be in the form of friction and heat generation. As thermal effects are not considered in this study, heat generation between surfaces is ignored. For the frictional interaction between the surfaces, the basic Coulomb friction model [5] had been incorporated in the FEA [46] *via* the definition of the coefficient of adhesive friction, μ_a . Depending on the scope of the FEA performed, different values of the coefficient of adhesive friction are taken and are specified in the respective discussion accordingly.

Adaptive Remeshing

As the scratch process involves large deformation, the FEA may encounter convergence problems arising from a severely distorted mesh. To maintain a high quality FE mesh throughout the analysis, adaptive remeshing, available in ABAQUS® [46], can be employed.

Lagrangian adaptive meshing, which is suitable for transient problem with large deformation, is selected to allow the adaptive mesh domain to move together with the material contained within. Adaptive remeshing can be however highly computational intensive and hence time consuming. To reduce computational time, only critical elements that are close to the scratch path are assigned for remeshing, as shown in Figure 7.

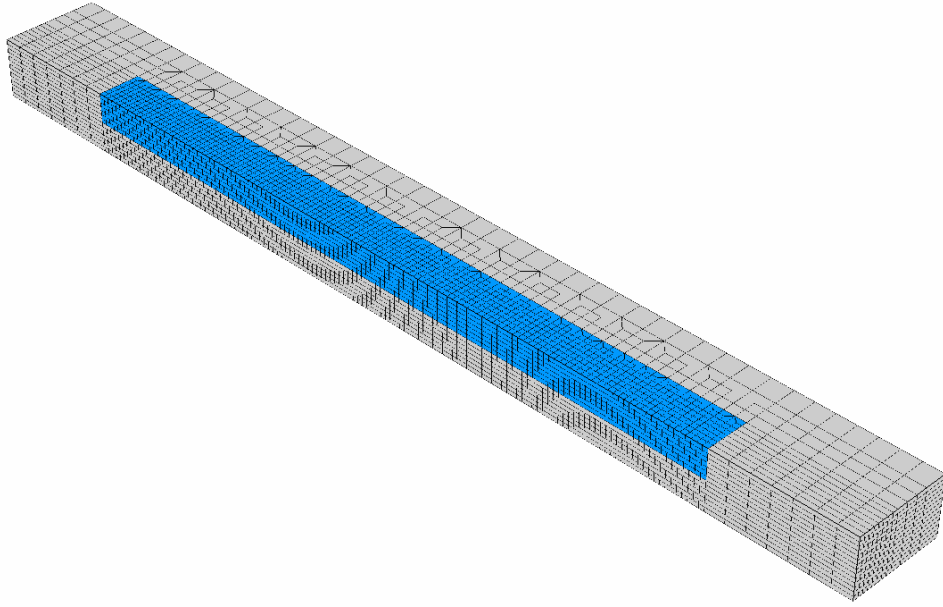


Figure 7: FE Mesh A and its adaptive remeshing domain (with darker shading).

Load Cases

Four different load cases, *Load Cases A – D*, are considered for this study, as summarized in Table 4. For Load Case A, the scratch process is characterized by a constant scratch speed v of the semi-spherical indenter under a constant normal load P . As for Load Case B, the normal load of the indenter increases linearly over the scratch length with a constant scratch speed. The normal load for Load Case C is kept constant while the scratch speed accelerates from zero to 20 m/s. As mentioned earlier that in the depth-controlled indentation step, it is necessary to determine the correct indentation depth for producing the intended normal load and establishing firm contact. Hence as would be expected, the indentation depths are different for different materials, mesh design and surface conditions. The indentation depths documented in Table 4 are

relevant for Material I, Mesh D and a coefficient of adhesive friction of 0.3. For the prediction of indentation depth for a specific normal load, one can refer to Appendices A-4 to A-6 for the plots and their fitted polynomial expressions of Material I – III and selected values for the coefficient of adhesive friction. The last load case, Load Case D, is specially designed for convergence study whose results are presented later in this chapter, as well as for parametric study in Chapter V. Load Case D essentially reflects a displacement-controlled scratch test. Unlike the other three load cases where static analysis is performed for the indentation step, all the three steps for Load Case D are considered as dynamic analyses.

Table 4: Load Cases A – D.

<i>Load Case</i>	<i>Indentation Step</i>		<i>Scratch Step ($t = 3$ ms)</i>	<i>Spring-back Step</i>
	<i>Depth-Controlled</i>	<i>Load Imposition</i>		
A	$u_3 = -0.03673$ mm	$P^* = 5$ N	$P = 5 - 15$ N $v = 10$ m/s	$u_3 = 3$ mm
B	$u_3 = -0.09865$ mm	$P = 15$ N	$P = 15$ N $v = 10$ m/s	$u_3 = 3$ mm
C	$u_3 = -0.09865$ mm	$P = 15$ N	$P = 15$ N $v = 0 - 20$ m/s	$u_3 = 3$ mm
D	$u_3 = -0.25$ mm	-	$u_3 = -0.25$ mm $v = 10$ m/s	$u_3 = 3$ mm

* Note that the normal load P was scaled by one-half due to the plane of symmetry.

Analysis time of the scratch step in all analyses is set at 3 milli-second (ms) and the scratch length is 30 mm. Though the resulting scratch speed may be fast for some

applications, the study intends to examine the fundamental behavior of polymers under different loadings and scratch conditions. The FE results obtained should still suffice to a better understanding of polymer scratch behavior.

CONVERGENCE STUDY

The aim of the convergence study is to determine the optimal mesh design for analysis so that sufficient numerical accuracy can be attained at an acceptable computational cost. Due to the lack of established analytical results in the open literature, this work uses Material Type II as the primary material for verification since full elastic recovery should be expected for pure elastic material in the wake of the traversing indenter. As indicated, Load Case D was adopted for this convergence study.

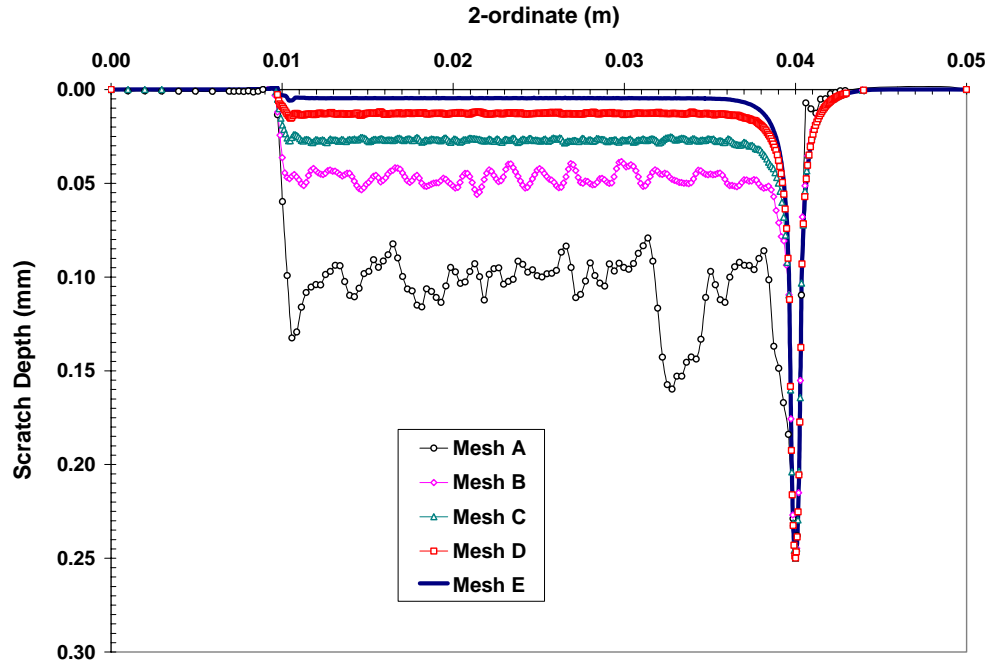


Figure 8: Scratch depth profiles for Meshes A – E at the end of the scratch process ($\mu_a = 0$).

Presented in Figures 8 and 9 are the scratch depth profiles for Mesh A – E at the end of the scratch process, without and with consideration of frictional interaction, respectively. The abscissa of the plots corresponds to the length PQ of the FE model (Figure 6). From both figures, one can see that the scratch profiles are converging to the zero level as the mesh size increases from Mesh A to E. The trend of convergence in these figure is indicative of the computationally intensiveness of the FE scratch analysis since a significantly high number of finite elements are required to achieve a reasonable level of recovery. For scratch analysis with no friction, the average residual depths for Meshes D and E are approximately 12.7 μm and 4.6 μm , respectively. However, the inclusion of frictional resistance in the scratch analysis ($\mu_a = 0.3$) increases the respective average residual depths to 17.1 μm and 11.2 μm for Meshes D and E, respectively. Hence, this implies that the effect of considering frictional interaction in scratch analysis adds more bearing on the required number of elements to achieve full elastic recovery.

While it may be ideal to add as many elements as needed for an accurate FEA, it is important to review the computational cost that comes with more elements. In Figures 10(a) and (b), the computational time³ of each mesh design for the FEA using Material Types II and III are plotted. Although the results generated by Mesh E have the best accuracy (see Figure 8), the analysis using the same mesh design is also the most computationally intensive, which can be as much as twelve days of computational time for Material Type III with the consideration of friction! To have a more reasonable and

³ FEA using ABAQUS was performed using one processor on a 32-processor IBM Regatta p690.

tractable computational time and yet maintain a reasonably good level of accuracy, Mesh D was chosen as the optimal mesh design to perform all the FEA in this study.

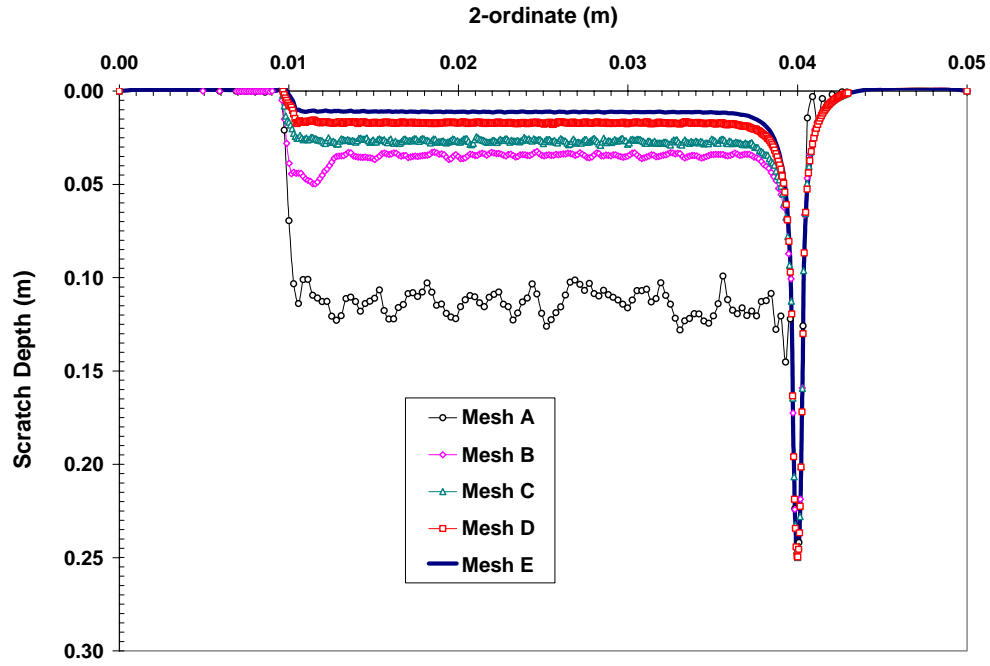


Figure 9: Scratch depth profiles for Meshes A – E at the end of the scratch process ($\mu_a = 0.3$).

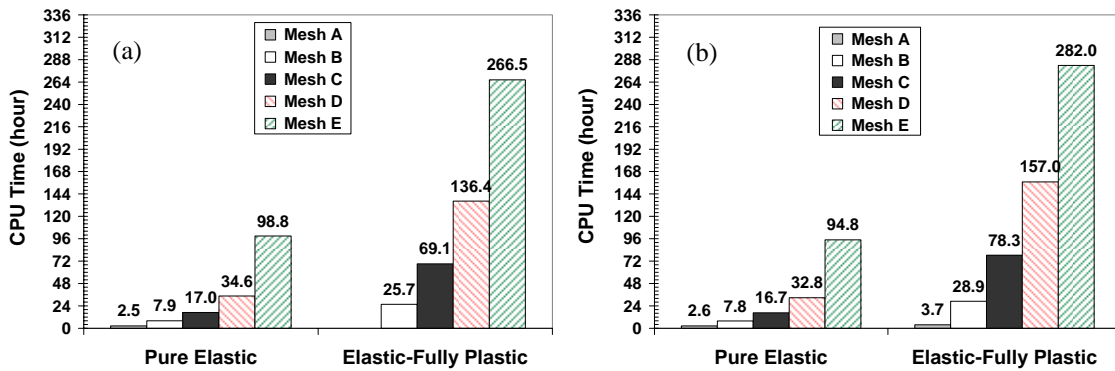


Figure 10: CPU time for Material Types II and III: (a) $\mu_a = 0$; (b) $\mu_a = 0.3$.

TIME INCREMENT FOR EXPLICIT TIME INTEGRATION SCHEME

With selection of the optimal mesh design (Mesh D), it is now relevant to pose the question of whether the stable time increment used by ABAQUS[®] is sufficient to ensure accuracy of the results. To examine this issue, a numerical exercise is conducted to evaluate the accuracy of the dynamic analysis performed by ABAQUS[®] using the stable time increment as well as a selection of smaller time increments.

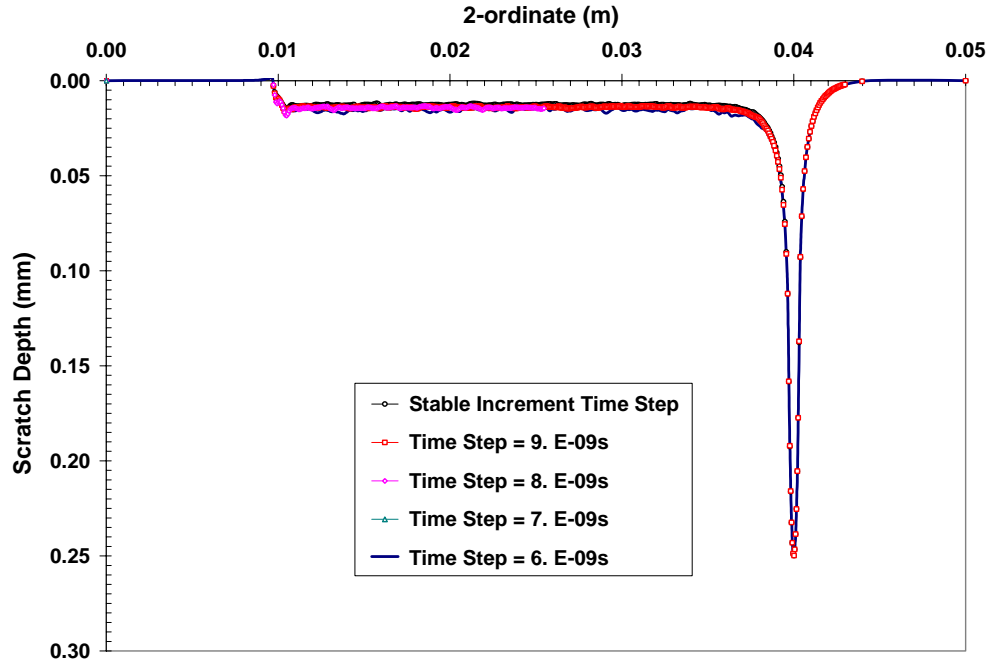


Figure 11: Scratch depth profiles using various time steps and Mesh D ($\mu_a = 0$).

Figure 11 shows the plots of scratch depths from FEA using different time increments along the length PQ of substrate (see Figure 6). For this exercise, the material of concern is Material II while Load Case D is adopted for the analysis. From

the figure, it is clear that there is no significant difference in scratch depth profiles based on the stable and other smaller time increments. It should be indicative that even with the use of stable time increment, the convergence of numerical results has been attained.

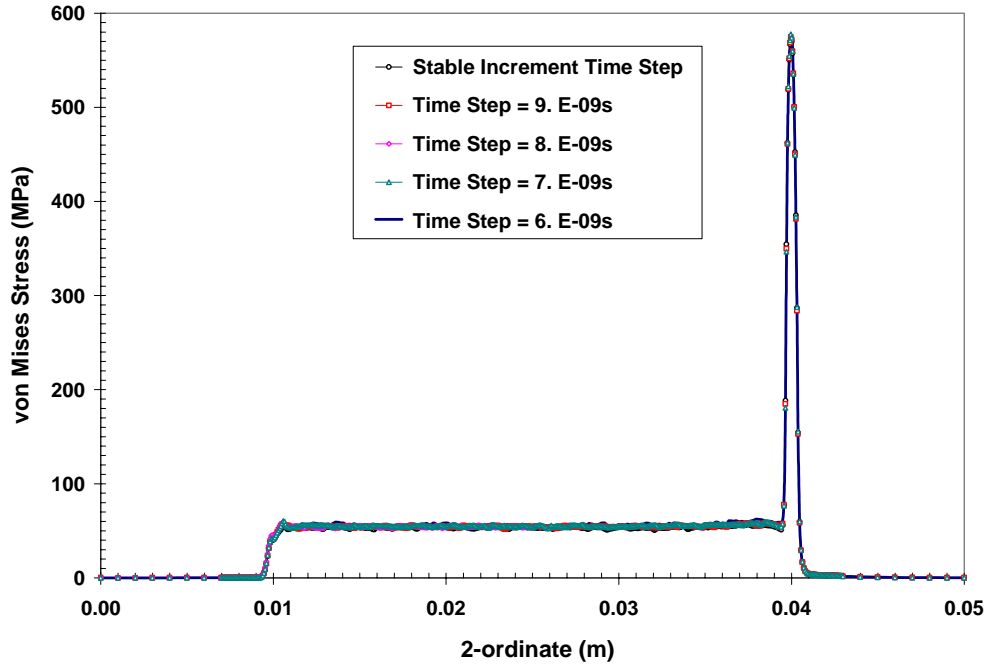


Figure 12: von Mises stress profiles using various time steps and Mesh D ($\mu_a = 0$).

This is further supported by the corresponding von Mises stress plots presented in Figure 12, where no discernible difference is again noted from various sets of results. Keeping the computational cost in mind, one can therefore conclude that adopting the stable time increment computed by ABAQUS[®] should be sufficient in ensuring both the stability and accuracy of the FEA results. While the above conclusion may be drawn based on a specific set of material, loading and surface conditions, employing smaller

time increments than those for stable values is in general computationally more expensive and can become prohibitive in some cases. In view of these, all dynamic analyses performed for this dissertation work shall henceforth adopt the stable time increment determined by ABAQUS®.

CHAPTER IV

SCRATCH DAMAGE AND CRAZE INITIATION

The prime objectives of performing finite element analysis (FEA) of the scratch problem for polymeric materials are to investigate the scratch response of such materials and study the damage mechanisms involved. It has been elaborated in Chapter III as to how FEA can be performed at a reasonable accuracy and computational cost using ABAQUS[®] with careful regards to the physics, experimentation and computational aspects of the problem. For this chapter, FEA results are presented to solicit a mechanistic understanding on the damage process of a scratch deformation on polymers, particularly for polypropylene (PP, Material I – see Table 3 in Chapter III). Two key damage modes, relevant to polymers – plastic yielding and crazing, are evaluated carefully with the use of numerical solutions. It is brought to the reader's attention through a discussion of numerical simulation that these two damage modes of polymers, as commonly found in various deformation processes such as impact fracture, occur concurrently in a scratch deformation process and may compete against each other for dominance. Several procedures on the use of various strain measures and reaction forces to quantify the scratch performance of polymers and predict the incipient of damage are introduced. In spite of a relatively simple elasto-plastic material model for PP and other assumptions adopted in this work, a good qualitative agreement between FEA results and experimental observations is achieved and it thereby establishes the usefulness of

FEA in examining polymer scratch damage mechanisms for shear yielding and crazing/microcracking.

SCRATCH WIDTH

To assess how scratch damage varies with different loading conditions, scratch widths from experimental testing and FE analyses are plotted in Figure 13. The loading condition considered for experimentation and numerical effort are given in Table 5.

Table 5: Loading conditions for experimentation and FEA.

Description	Experiment	FEA
Increasing Normal Load/ Constant Scratch Speed	$P = 0 - 50 \text{ N}$ $v = 100 \text{ mm/s}$	<i>Load Case A</i>
Constant Normal Load/ Constant Scratch Speed	$P = 30 \text{ N}$ $v = 100 \text{ mm/s}$	<i>Load Case B</i>
Constant Normal Load/ Increasing Scratch Speed	$P = 30 \text{ N}$ $v = 0 - 140 \text{ mm/s}$	<i>Load Case C</i>

To enable a consistent comparison across different types of scratch conditions, measurement of scratch widths are based on the definitions provided in the figure and at points where the normal load corresponds to 30 N and the scratch speeds are 100 mm/s and 10 m/s for experimental and numerical results, respectively. Reviewing both sets of results for the three load types, it can be observed that a change in scratch speed

produces the most severe scratch damage while an increasing normal load for scratching yields the least damage.

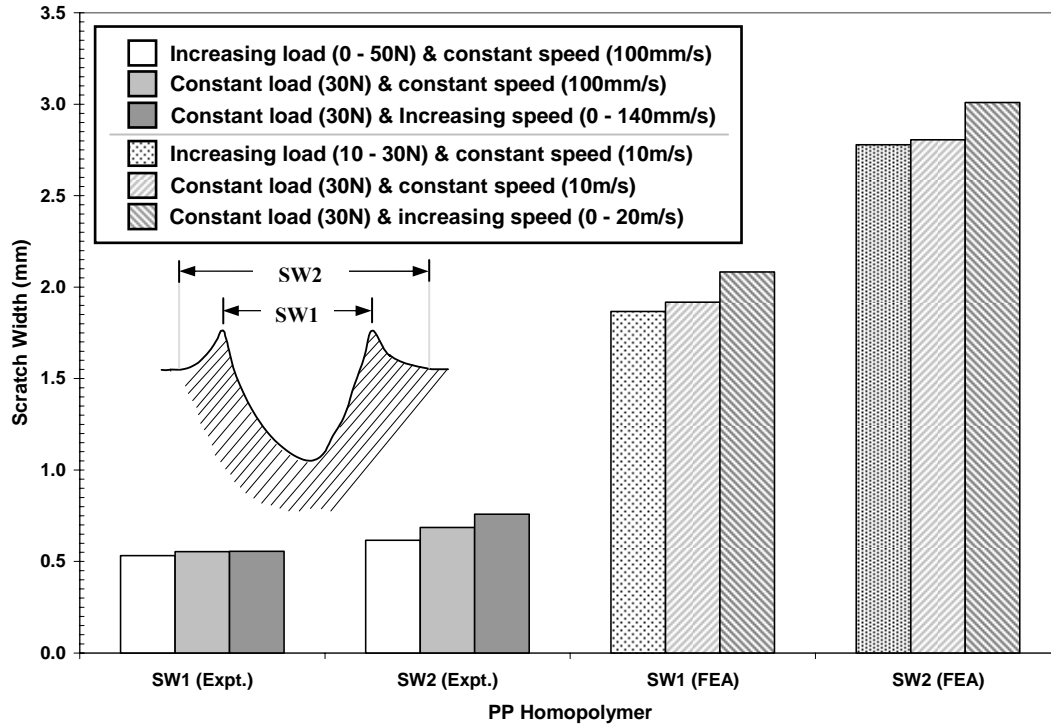


Figure 13: Comparison of scratch widths for different load cases.

Despite the dissimilarity of the scratch speed in the experiment and FE analyses, this qualitative trend can be observed from both sets of results. However, there is a marked quantitative difference between the two sets of data. For the higher scratch speed used in the FE analyses, the analyses should have predicted a lesser amount of scratch damage in the polymeric material, since the mechanical behavior of polymers are

normally affected by strain rates and tend to be stiffer at higher strain rates. Hence by relating the scratch speed to strain rate, it is concluded that the numerical effort overpredicts the scratch damage. The overprediction of scratch damage may be mainly attributed to the choice of the material constitutive model, which requires further refinement to correctly capture strain-rate dependent behavior.

SCRATCH DAMAGE PROCESS AND ITS MECHANISM

Under controlled laboratory conditions, it is relatively easy to reproduce scratches on specimens. But without a precise and rapid video imaging capability, scratch tests in most experimental set-ups will occur too rapidly to capture the sequential formation of scratch grooves. In this regard, FEA becomes useful as it generates a database of results to capture the time evolution of the scratch process that can be reproduced graphically to aid visualization.

Figure 14(a–d) shows the deformation sequence of a PP substrate as the indenter ploughs through it. In Figure 14, layers of the substrate over a section of concern are shaded differently and the indenter is moving out towards the reader. Figure 14(a) first shows a relatively undeformed section of substrate that is ahead of the approaching indenter. The section begins to undergo compression and is squeezed upwards as the indenter moves ahead as shown in Figure 14(b). In Figure 14(c), the approaching indenter continues to exert its compressive action on the section while it also pushes the material sideways. Once the indenter overcomes and ploughs through the materials, a scratch groove is formed, as illustrated by Figure 14(d).

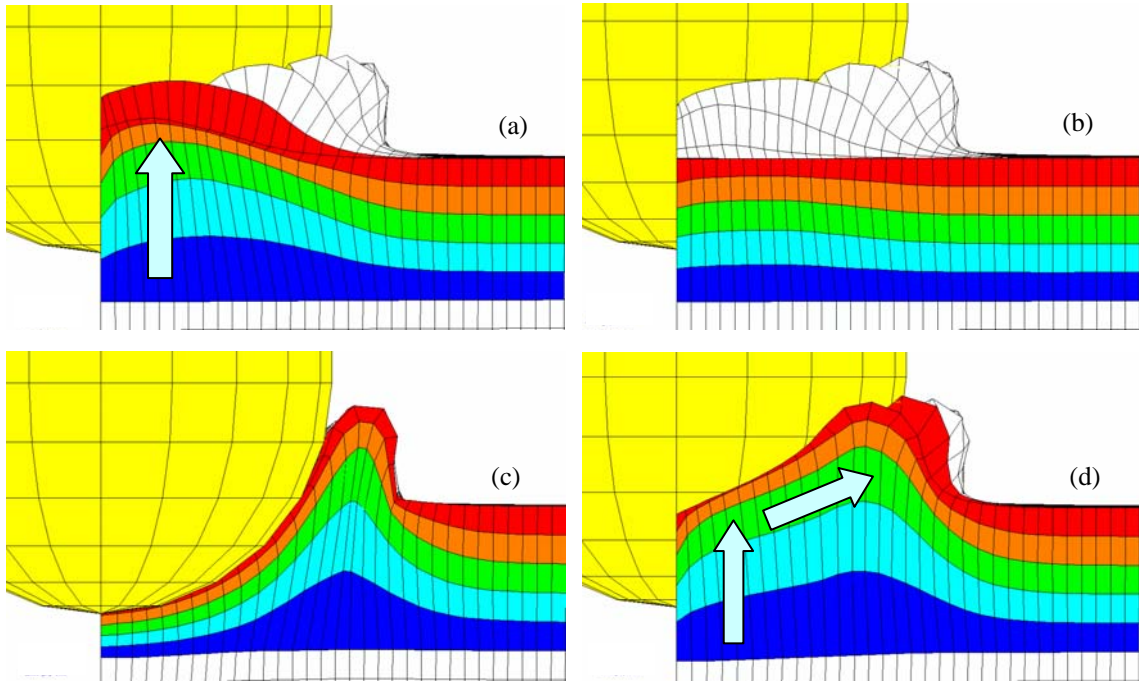


Figure 14: (a) Undeformed section; (b) section is compressed and squeezed upwards; (c) section is pushed to the side; (d) a scratch groove is formed.

Though the sequential formation of scratch grooves can be shown through Figures 14, it is more insightful if the mechanical response of the material around the indenter tip is known, which may allow one to make further prediction on the local material damage or fracture. For that, Figure 15 presents plots of the maximum principal stress variations along the length PQ of the FE mesh (see Figure 6) at various time intervals of the scratch step. Herein, discussion is focused on the results for Load Case B and Material I while the coefficient of adhesive friction at the surface of the indenter is taken to be 0.3.

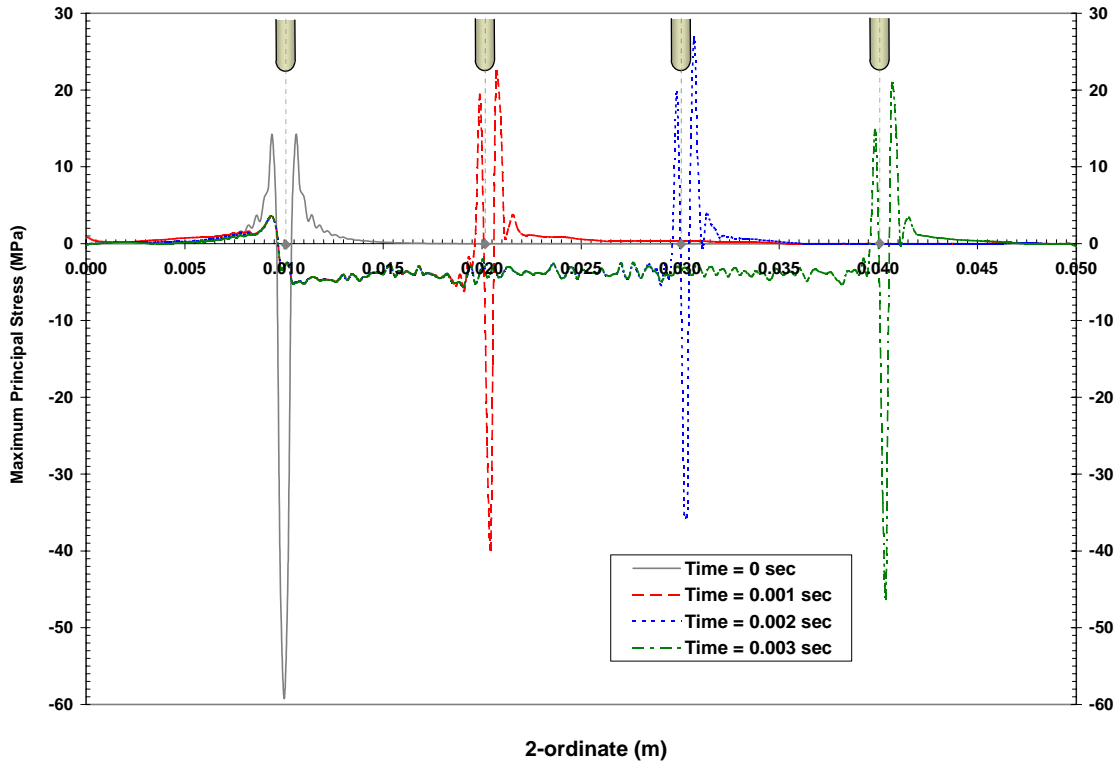


Figure 15: Maximum principal stress profiles and the positions of the indenter at various stages of the scratch process.

The maximum principal stress plots give a good indication of the stress state of the material around the indenter tip. Prior to the beginning of the scratch step ($t = 0$ sec) where the deformation remains predominantly that of an indentation, the material beneath the 1-mm tip, as observed in Figure 15, is under compression while the surrounding material is in tension. Such a stress variation has been reported analytically in [12,56]. Once scratching occurs, the maximum principal stress profiles reveal that while the material beneath the front-section of the tip remains under compression, the stress state in the material under the back-section of the tip now becomes tension. Tensile stresses can also be observed for material that is further ahead of the indenter.

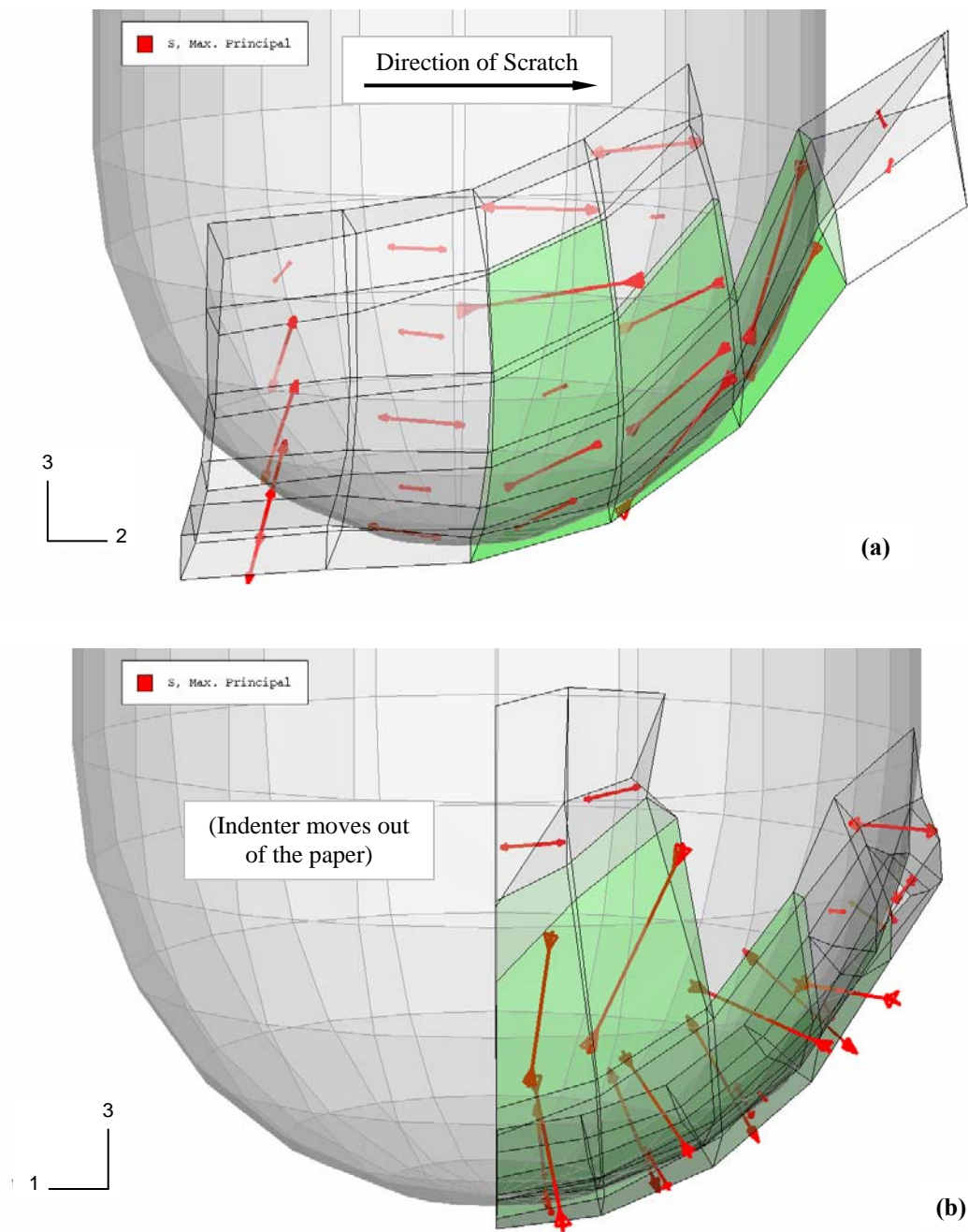


Figure 16: Direction of maximum principal stress in the elements around the indenter (Load Case B) (a) perspective in 2-3 plane; (b) perspective in 1-3 plane.

To make a link between the stress state of the materials around the indenter to the possible fracture patterns, one can review the direction at which the maximum principal stresses act for the elements around the indenter, as presented in Figure 16. Arrows pointing outwards indicate that the maximum principal stresses are tensile while inward-pointing arrows signify compressive stresses. For clarity, elements with tensile maximum principal stress are differentiated from those with compressive stresses by their lighter shading.

Figure 16(a) shows that tensile stresses are present for the elements behind and away from the indenter tip, which is consistent with the results shown in Figure 15. The state of maximum principal stress is generally compressive for the elements right under the front-section of the indenter. Also, the tensile stress vectors for the elements right behind the tip are generally in the 2-direction while the stress vectors in the left-most rows of elements are in the vertical 3-direction and with slight biases in the 2-direction. This suggests that as the indenter moves, the material right behind the indenter is stretched in the direction of the scratch. If fracture does occur, it is likely that cracks form perpendicularly to the scratch direction. As the indenter continues to plough forward, the same materials are now pulled outwards in the vertical direction in addition to being stretched in the scratch direction, possibly leading the materials to be spalled off. Such spallation or delamination is commonly observed during scratch testing of coated systems [57]. It is noted that tensile stresses are also found in the outer-most row of elements ahead of the indenter. As shown in Figure 16(b), the stress vectors of these elements are stretched outwardly in the 1-direction, suggesting that the material in that

region tears apart as the indenter ploughs through, forming cracks parallel to the scratch direction.

In summary, through the study of the maximum principal stress and its directionality in the materials beneath and around the indenter tip during a scratch, the phenomenological occurrence of the scratch damage mechanism can be deduced, which is, in turn, related to the fracture patterns of scratches.

QUANTIFICATION OF PLASTIC DAMAGE

Based on the elasto-plastic FEA as discussed earlier, it is expected that the maximum von Mises stress exists underneath the tip of the indenter as it traverses across the scratch path. Change in the maximum von Mises stress along the scratch path indicates the amount of the plastic flow (hardening or softening) taking place during the scratch and this can indirectly be related to the extent of plastic damage that occurred along the scratch path. The amount of plastic flow can also be measured by the magnitude of the equivalent plastic strain, which is used to describe a change of the yield stress for the isotropic hardening rule in Eq. (2).

To study the plastic flow and thereby evaluate the extent of plastic damage across the scratch path, maximum envelopes of the von Mises stress and equivalent plastic strain as computed by FEA for Load Case A – C and Material I are presented in Figures 17 and 18, respectively. In both figures, a plot of the ultimate von Mises stress and equivalent plastic strain has been included accordingly. Neglecting the numerical fluctuation, the maximum envelope of the von Mises stress for Load Case B reaches the

ultimate value the most rapidly, followed by Load Cases C and A. The reason for such a trend is that among all cases, Load Case B has the most severe loading conditions right from the beginning of the scratch process while in Load Case A, the increasing normal load expectedly produces an increasing stress variation before the ultimate value is reached. As modeled, the material has no additional load-carrying capacity beyond the ultimate value and behaves perfectly plastic, which explains why the maximum envelopes do not exceed the ultimate value.

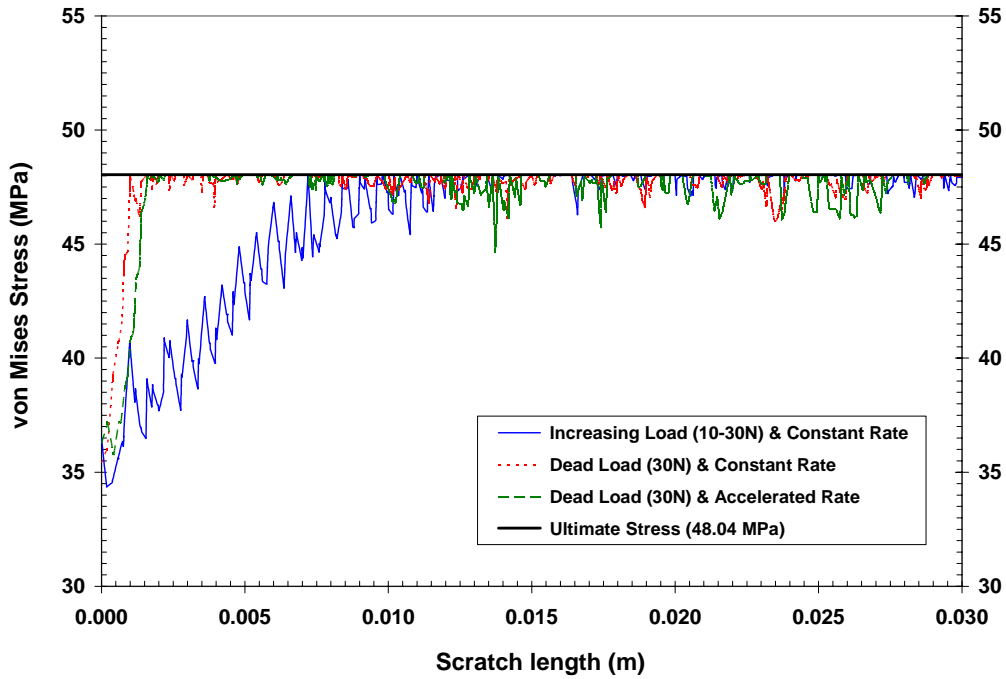


Figure 17: Maximum envelope of von Mises stress for different load cases along the scratch path.

For the equivalent plastic strain, similar conclusion can be reached such that the maximum envelope reaches the critical value that corresponds to the ultimate stress, first

for Load Case B and C and, finally, A. Beyond the ultimate value, the equivalent plastic strain continues to raise, indicating that more plastic flow is taking place despite that no further hardening or softening of the material. Another worthwhile inference that can be drawn from this discussion is that a more realistic and comprehensive damage model can be implemented in the FEA, together with the constitutive model. Allowing the loss of material stiffness at various stages of damage in the new damage model yields a better representation of plastic damage at material points and thereby results in stress redistribution to neighboring materials.

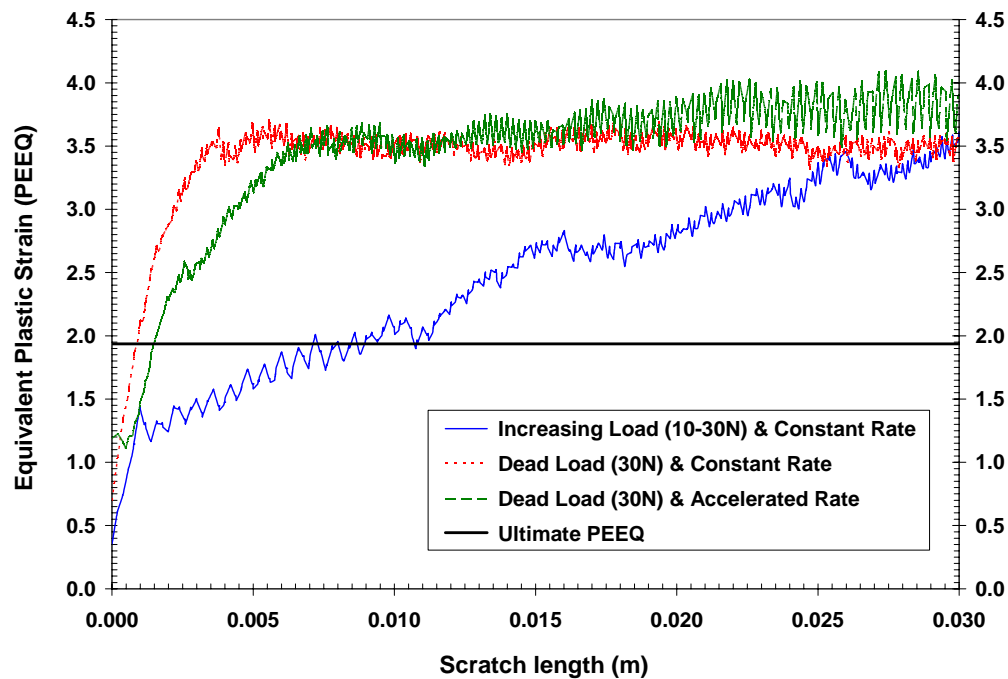
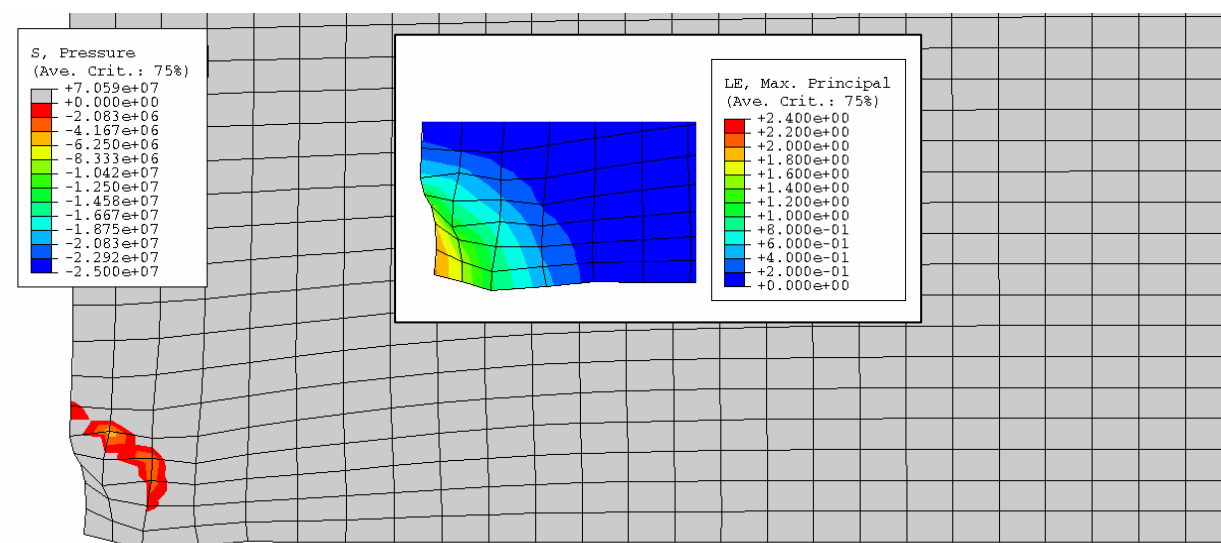


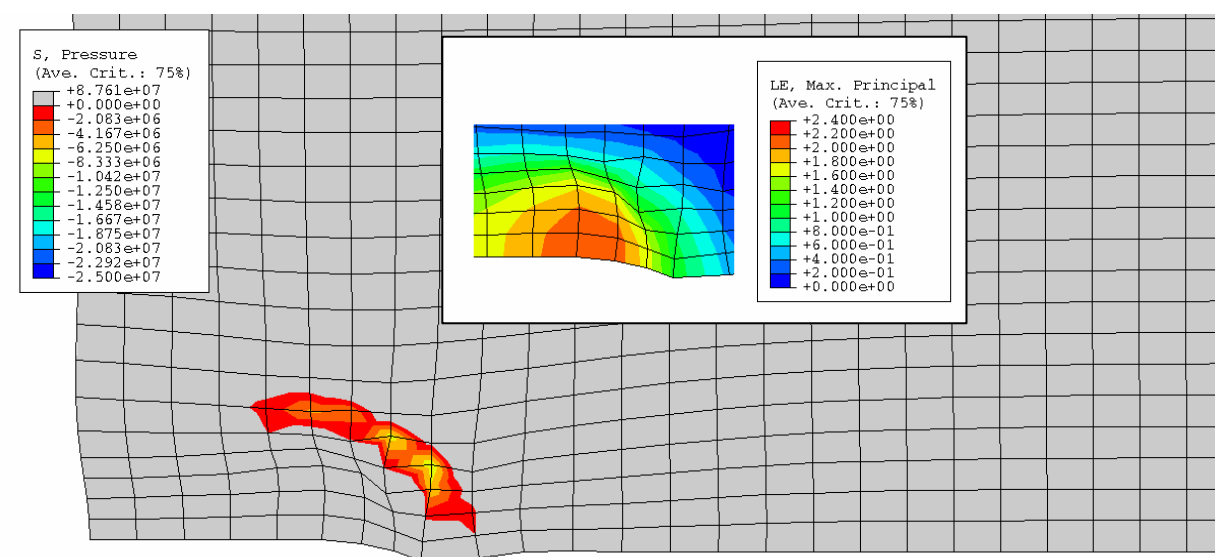
Figure 18: Maximum envelope of equivalent plastic strain for different load cases along the scratch path.

ASSESSMENT OF CRAZE INITIATION

Fracture mechanisms such as crazing, voiding, debonding, and cracking can cause stress whitening in polymers. Hence, there is a need to investigate the possible initiation of these fracture processes prior to looking into stress whitening. Though the scope of this study focuses on craze initiation, the governing criteria for craze initiation can nevertheless be applied to voiding, debonding, and cracking because these fracture processes are fundamentally similar to crazing and can be described by the same type of stress/strain components, *i.e.*, the critical strain, the maximum dilatation, and the maximum hydrostatic tensile stresses. Of the various criteria for craze initiation, the critical strain criterion by Bowden and Oxborough [54] is adopted. Using this criterion, Eq. (4), the compressive stress (pressure) contour plots at four different time intervals are given in Figure 19(a-d) for Load Case A and Material I. Only negative values of the pressure contours are presented as they correspond to hydrostatic tensile stresses. Inset plots in each of the figures contain the maximum principal strain data that are limited to positive values. From these figures, it is apparent that crazes are likely to form in the regions ahead and around the front sides of the moving indenter. As the indenter thrusts forward, the crazes ahead of the indenter if they exist are ruptured based on previously identified scratch damage process in Figure 14. As such, the only crazes that can probably be observed are along the side ridges of the scratch groove. With regard to Load Case A, it can be inferred that there is a point along the scratch path where the maximum principal strain increases to a critical value, beyond which crazing occurs and stress-whitening phenomenon prevails.



(a)

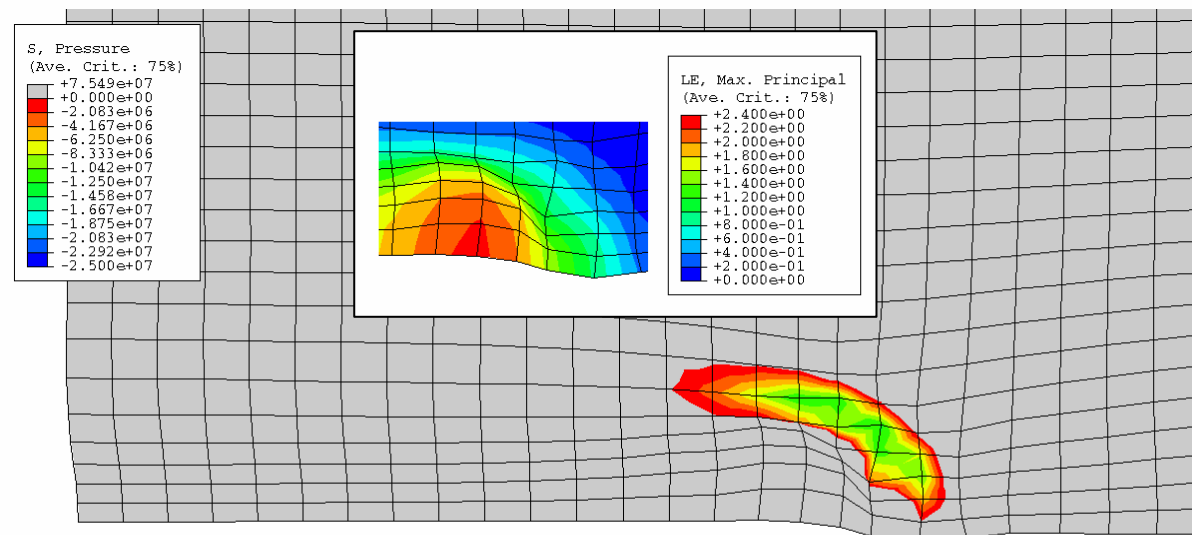


(b)

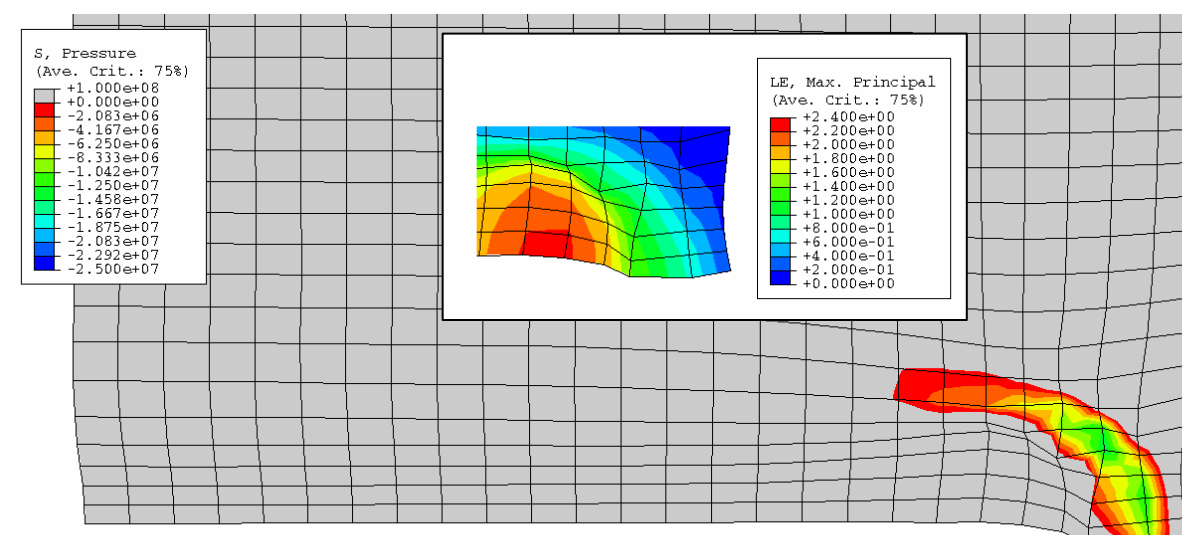
Direction of Scratch



Direction of Scratch



(c)



(d)

Figure 19: Pressure and maximum principal strain contour plots at four different time intervals (a – d) (Load Case A).

PLASTIC YIELDING AND CRAZING

It is known that shear yielding and crazing are two key damage modes for polymers. From previous sections, numerical results have been reviewed for a phenomenological examination of the occurrence of damage in materials around the indenter tip and the formation of crazes during the scratch process. Henceforth, it is of research interest to study the quantitative variation of plastic yielding and crazing along the scratch length, based on the increasing load in Load Case A.

Presented in Figures 20 and 21 are plots of the maximum envelope of the equivalent plastic strain and volumetric strain along the scratch path for Material I, respectively. From Figure 20, it is evident to note the large extent of plastic damage occurs in the material, especially towards the end of the scratch process. Though not considered in the FEA, materials are likely to fracture and spall off from the scratch path beyond plastic strain levels of 200-300%. The consideration of ultimate material failure is introduced formally as a future research scope in Chapter VII.

For Figure 21, the use of volumetric strain allows one to correlate to the amount of crazing that takes place during the scratch process. Comparing both plots and considering the linear load increase in Load Case A, it is interesting to note that other than the initial portion, the variation of equivalent plastic strain follows a linear trend while the volumetric strain increases in a quadratic manner. This indicates that crazing may not be a dominant damage mode at the beginning of the scratch process but may compete with shear yielding for dominance towards the end. Since crazing promotes the stress-whitening phenomenon, there is a critical point during the scratch process where

the volumetric strain reaches the threshold to initiate stress-whitening. For future implementation, it is beneficial for the study of crazing damage if criteria for the growth and failure/fracture of crazes can be incorporated in the FEA. Again, the above discussion reiterates the need for a more complete damage mechanism that not only captures the incidence of plastic yielding and crazing, but also allows competition between these two damage modes.

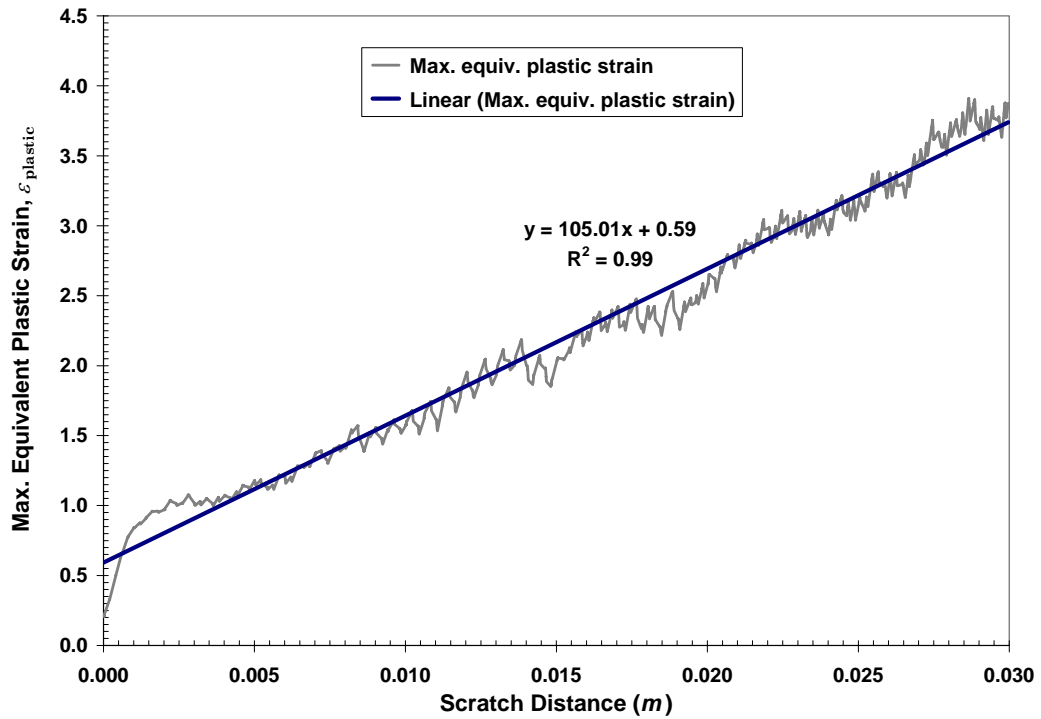


Figure 20: Maximum envelope of equivalent plastic strain along the scratch path.

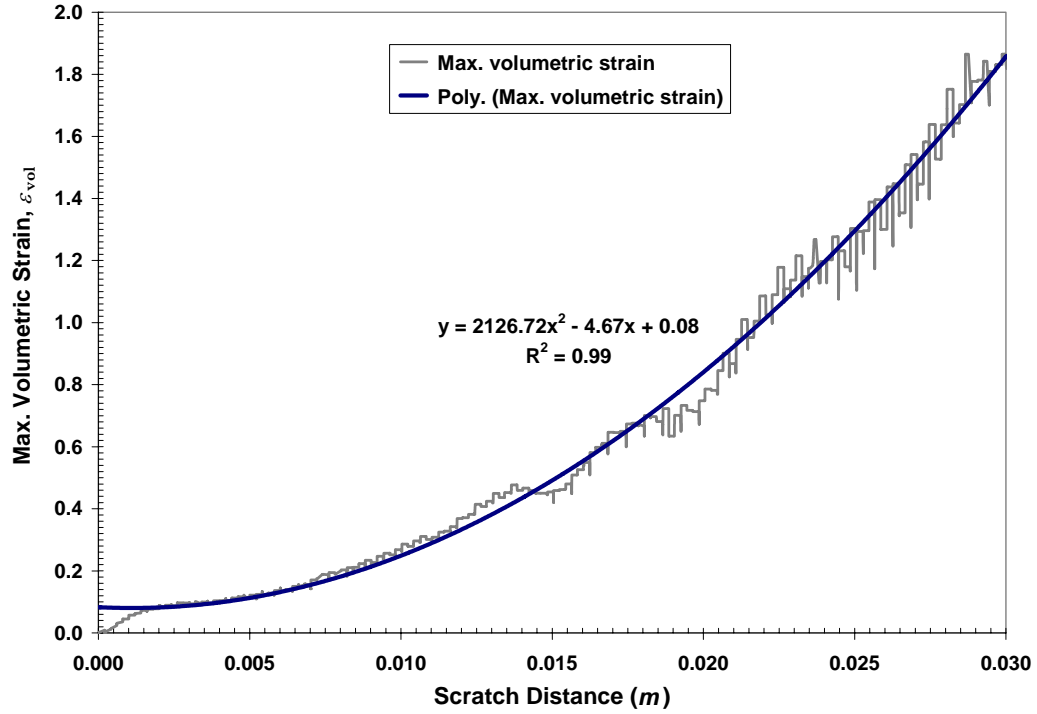


Figure 21: Maximum envelope of volumetric strain along the scratch path.

SCRATCHING COEFFICIENT OF FRICTION (μ_s)

Due to the initial indentation from the applied normal load, the tangential force encountered by the indenter during the scratch process cannot be entirely attributed to the adhesive frictional interaction. As noted in several research works [49,50,58] and shown in Figure 22, part of the tangential force on the indenter comes from the resistance of the material ahead of the indenter as the indenter ploughs forward. As such, the ratio of the tangential force to the normal load, herein referred to as the scratching coefficient of friction, μ_s (SCOF), has both the adhesive and ploughing components.

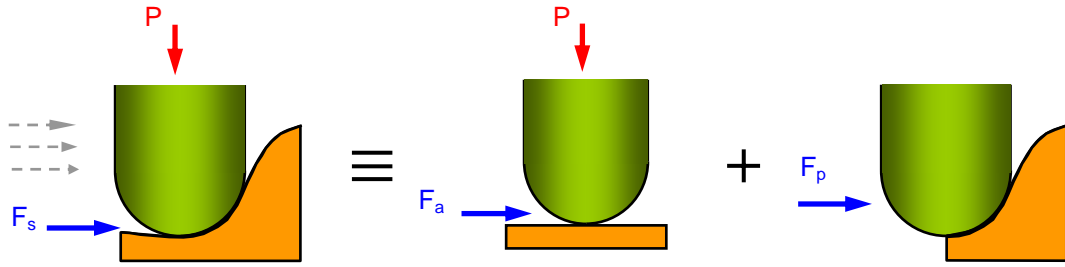


Figure 22: Tangential force acted on the indenter during the scratch process.

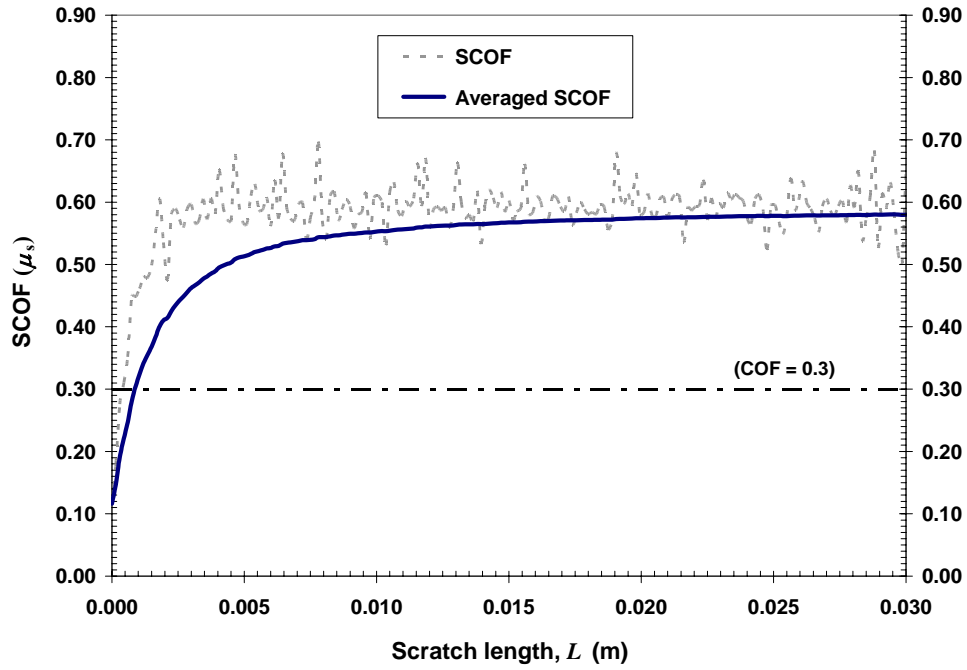


Figure 23: Scratching coefficient of friction along the scratch path (Load Case B).

To evaluate the SCOF for PP (Material I), Load Case B was adopted as it yields a homogeneous state of scratch deformation. Figure 23 shows a plot of the computed SCOF over the scratch length using Load Case B, whose oscillating behavior can be attributed to the dynamical variation and intrinsic numerical noise. Despite the

numerical fluctuation, it can be observed that the plot fluctuates around a mean value. To demonstrate this, an additional plot has been given in Figure 23 to show the averaged value of the SCOF across the scratch length. Towards the end of the scratch length, the averaged plot converges toward a limiting value. To seek this limiting value, an apparent solution is to perform FE analysis over a longer scratch length. This option can however be time-consuming and impractical since the required scratch length to achieve convergence is unknown. To overcome that, a Southwell plot can be created by plotting the scratch length (L) against the value of (L/μ_s) . Through the use of Southwell plot, the limiting value can readily be furnished from the slope of the linear fit of the Southwell plot. Based on the result of Figure 24, the scratching coefficient of friction of polypropylene is found to be 0.589, as compared to the adhesive value (μ_a) of 0.3. The amount of deviation of μ_s from the coefficient of adhesive friction is indicative of the extent of ploughing resistance. Also for Load Case B where a constant normal load is imposed throughout the scratch process, the SCOF can be related to the resistance put up by the material against the scratching action and can hence be used to evaluate the scratch resistance of a material. As discussed in Chapter V, there are two components for the assessment of the scratch performance of a material, which are scratch resistance and scratch visibility. For materials that exhibit a same level of scratch visibility due to similar fracture patterns, the SCOF can then be adopted as a useful ranking parameter for scratch performance.

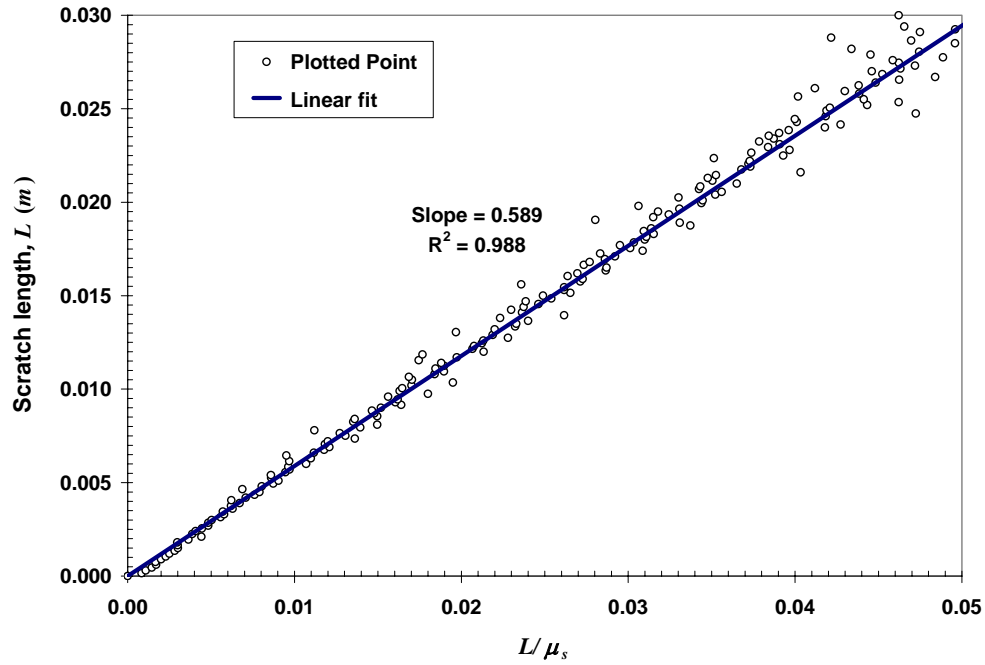


Figure 24: Southwell plot of the scratching coefficient of friction.

CONCLUDING REMARKS

As presented in this chapter, findings from the numerical discussion contribute to the current knowledge of the scratch damage of a polymer. To assess the change in scratch damage due to loading conditions, it has been shown that the results furnished by finite element analysis (FEA) correspond qualitatively well with the experimental data. Changing the scratch velocity during the scratch process produces the worst scratch damage, as compared to keeping the scratch velocity the same or increasing the normal load imposed on the indenter. Through examination of the maximum principal stress along the scratch path, a drastic change in the state of stress was noted in materials under the indenter before and after scratching. By further reviewing the action of the

maximum principal stress vectors in the materials beneath the indenter, a mechanistic understanding on the occurrence of scratch damage and the fracture patterns is obtained.

Numerical results from FEA were also reviewed to look into the two main damage modes of polymeric materials, plastic yielding and crazing. With regards to the attempt to quantify plastic flow in the scratched materials, it was found that a loading condition of constant normal load and constant scratch speed generates the earliest initiation of ultimate fracture, as compared to the conditions of changing normal load or scratch velocity. Such an understanding on the fracture initiation based on shear yielding indicates a future research need for a more realistic damage model that permits a loss of stiffness at material points where the ultimate stress state is attained. The new damage model, if implemented in FEA, should allow a better representation of stress redistribution in materials near a damaged region. Through the application of craze initiation criterion by Bowden and Oxborough [54] and volumetric strain measure, it is learned that crazing and shear yielding can coexist during a scratch deformation. Numerical results also suggest that these two damage modes may compete against each other for dominance in the scratch process. In view of crazing, the damage model proposed earlier can further be enhanced in its modeling capability by incorporating crazing as part of the damage criterion. In an attempt to quantify the scratch resistance of a material, a parameter called scratching coefficient of friction is employed in this study to relate the tangential force acted on the indenter to the normal load imposed during the scratch process.

CHAPTER V

SCRATCH PARAMETRIC STUDY

As part of research, parametric studies are often conducted to evaluate the importance of various quantities and assess the extent of their influence on a problem. For this scratch study, the interest of performing parametric study is particularly relevant to material scientists whose common aim is to design high performance scratch-resistant polymers. As an obscure quantity, it is per se difficult to give a definition to the scratch performance of a material, let alone to make quantification. For a systematic study on the topic, it is proposed that there are two key elements to scratch performance, namely, scratch resistance and scratch visibility. To evaluate the dual elements of scratch performance, finite element analysis (FEA) of the scratch problem using ABAQUS[®] is executed. Parametric studies using FEA are also performed to identify key mechanical and surface properties of a material that are important for improving scratch performance.

In this chapter, a formal introduction of the dual elements or definitions of the scratch performance is made to serve the needs of the intended parametric study using FEA. Presented thereafter are the parametric results to reveal the influence of the mechanical and surface properties of a material on its scratch performance.

SCRATCH PERFORMANCE

Similar to steel or concrete structural designs where ultimate strength design must be satisfied together with serviceability requirements, scratch performance of materials can also be perceived with the same duality. Herein, the dualism in scratch performance of materials is related to scratch resistance and scratch visibility. Scratch resistance can be interpreted as the inherent material resistance to scratch deformation and is derived purely as a material response. Scratch visibility, on the other hand, is the degree of visual perceptibility of scratch damage by human eyes and can be influenced by the types of surface damage and external factors such as color and lighting. Particularly for polymers, fracture mechanisms like brittle fracture and plastic yielding can play a vital role in affecting scratch visibility [4]. The need of dual definitions for scratch performance can be appreciated that in some cases where only minor scratch damages are observed on a material that are highly scratch-resistant. However due to brittle fracture leading to a drastic change in surface roughness, light dispersion from the scratches become more pronounced, making the scratches easily perceptible by individuals. In other applications where product aestheticism is emphasized, reducing scratch visibility of a material may be weighed more importantly than improving its scratch resistance. Therefore, the balance between scratch resistance and scratch visibility for the emphasis of scratch performance depends on the applications and industries.

The first documented attempt to quantify scratch resistance of materials should be attributed to Mohs back in 1824. Remaining useful until today, Mohs' simple scale

ranks the scratch hardness of a material using ten different minerals with talc being the softest and diamond the hardest. In a related work [59], Tabor compiled the indentation hardness values of the minerals by other researchers and established a relationship between the hardness values and Mohs numbers. While there is no dispute over the relationship between indentation and scratch hardness, the physics behind the proposed relationship and its practical use however remain unclear. Though the Mohs scale can be employed to differentiate the scratch hardness of materials, its numbers are not equally spaced and are limited for materials to be ranked within the same interval. It was not until Williams [45] published his analytical work more than a century after Mohs that formal definitions for scratch and ploughing hardnesses are put in place for quantifying scratch resistance of materials. After that, there are several other scratch-related hardness quantities that have appeared in the literature, like *tangential hardness* [60,61], *dynamic hardness* [60] and *specific grooving energy* [62]. Despite the wide variety of hardness definitions, their physical meanings remain essentially unchanged, *i.e.*, to determine the magnitude of force needed to induce a certain amount of scratch damage in the form of damaged area or volume. In retrospect if the scratched area or volume can be controlled, the scratch hardness (resistance) of a material is simply reduced to none other than the forces needed to make scratches. Such a situation does exist in problems where scratch depth is controlled at a constant value throughout the scratch process.

To measure scratch visibility of a material, evaluation and imaging tools like scanners [4,55], optical and electron microscopes [4,50,63] and VIEEW[®] [4] are

commonly used. Characterization of scratch damage can range from simple scratch geometry descriptions like scratch widths and depths [50] to sophisticated image analysis parameters like light scattering average and difference [63]. A key contributing factor to increased scratch visibility is the surface roughness of the scratched material. A rougher scratched surface is likely to scatter light in a more pronounced manner, thereby increasing scratch visibility. In line with the technique employed for parametric study in the present work, the use of scratch geometry should suffice to compare scratch visibility if the corresponding scratch damage mechanisms are the same among the material systems to be compared.

SCHEME OF PARAMETRIC STUDY

The objectives of the parametric exercise are to identify and understand the influence of mechanical and surface properties of a material on its scratch performance. For the parametric study, ABAQUS[®] is adopted to perform the required FEA and Mesh D and Material Type III (see Tables 2 and 3, respectively) are employed. However, the FEA considered herein is different from those considered in the last chapter as scratches are displacement-controlled (Load Case D – see Table 4 in Chapter III), rather than load-controlled. Without the need of finding the right indentation depth for a specified normal load, this simplifies the FEA and hence reduces the total computational time. As will be highlighted later, this also allows a simple assessment of the scratch resistance of a material. The parameters of concern in this study are the elastic modulus, Poisson's ratio, yield stress and the coefficient of adhesive friction of a material. Table 6 outlines

the scheme of the parametric study and the selected parametric ranges are in general relevant to polypropylene.

Table 6: Scheme of parametric study for scratch performance.

Parameter Type	Parametric Range	Constant Input
Elastic Modulus (E)	1.0 – 2.0 GPa	$\nu = 0.4$ $\sigma_y = 35\text{MPa}$ $\mu_a = 0$
Poisson's Ratio (ν)	0.25 – 0.45	$E = 1.65\text{GPa}$ $\sigma_y = 35\text{MPa}$ $\mu_a = 0$
Yield Stress (σ_y)	30 – 50 MPa	$E = 1.65\text{GPa}$ $\nu = 0.4$ $\mu_a = 0$
Coefficient of Adhesive Friction (μ_a)	0 – 0.6	$E = 1.65\text{GPa}$ $\nu = 0.4$ $\sigma_y = 35\text{MPa}$

PARAMETRIC STUDY: SCRATCH RESISTANCE

Due to the complexity that is involved in the scratch deformation process, quantifying the scratch resistance of a polymer requires an appropriate measure. Based on the constant-depth scratch analysis adopted, the scratch damaged area under the indenter remains fairly constant. Hence as discussed earlier, scratch resistance of a material can be simply associated with the reaction forces (tangential and normal) experienced by the indenter during the scratch process. A higher reaction force on the

indenter indicates more resistance by the material against the action of the force. Hence the normal force can be related to the indentation resistance of the material while the tangential force can be associated to scratch resistance. The indentation resistance as referred herein should not be confused with the static indentation hardness, since the scratch process is dynamical in nature.

Mechanical Properties

Performing the required FEA based on the scheme of the parametric study, averaged values of the reaction forces acted on the indenter during the scratch process are computed and presented with the corresponding standard deviations in Figure 25(a) – (c). As a remark, the fluctuation observed in the results of in Figure 25, as indicated by the standard deviations, is a numerical artifact due to finite element mesh size.

From Figure 25, one can observe that increasing the elastic modulus and yield stress of a material has a positive impact on its scratch resistance. To seek an explanation for such an improvement, it is helpful to first appreciate the fact that the scratch deformation at hand is essentially a constant-strain problem since the scratch depth and velocity remain constant throughout the process. With this in mind and the aid of the stress-strain diagram in Figure 26(a), increasing the elastic modulus while keeping the yield stress constant generates more internal strain energy in the system as indicated by the area (X). Additional strain energy can also be observed in the area (Y) of Figure 26(b) when one increases the yield stress and keeps the elastic modulus the same. For the conservation of energy, the additional internal strain energy must be

balanced by an increase in externally applied force, which provides the reasoning for the increase of tangential and normal forces when elastic modulus or yield stress is raised.

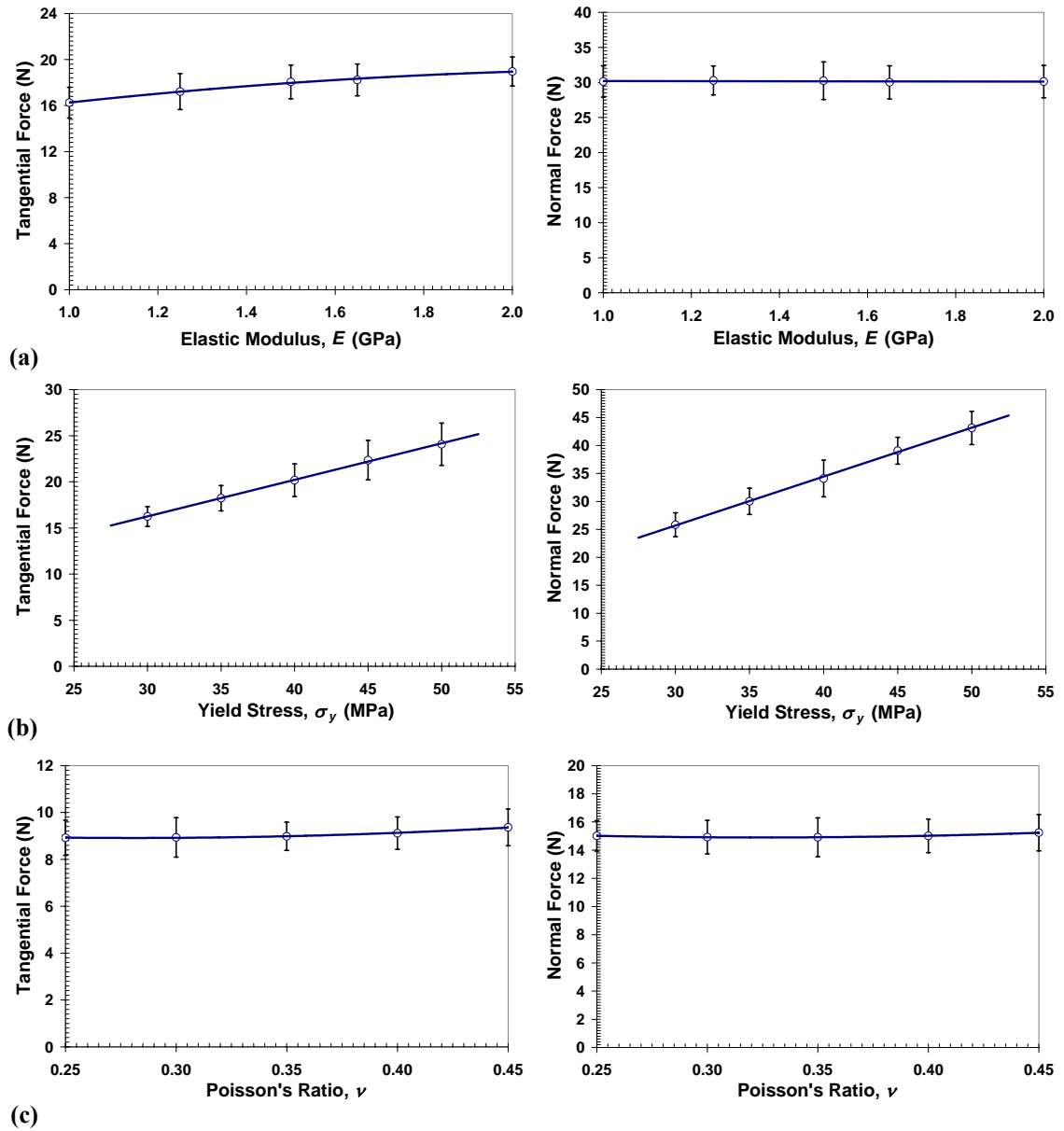


Figure 25: Variation of reaction forces with (a) elastic modulus; (b) yield stress; and (c) Poisson's ratio.

Also from Figure 25(a) and 25(b), it is also interesting to observe that the improvement in scratch resistance by raising the elastic modulus of a material is not as significant as that for changes in its yield stress. In line with those of elastic modulus and yield stress, raising the Poisson's ratio of a material does improve its scratch resistance but only slightly, as demonstrated in Figure 25(c).

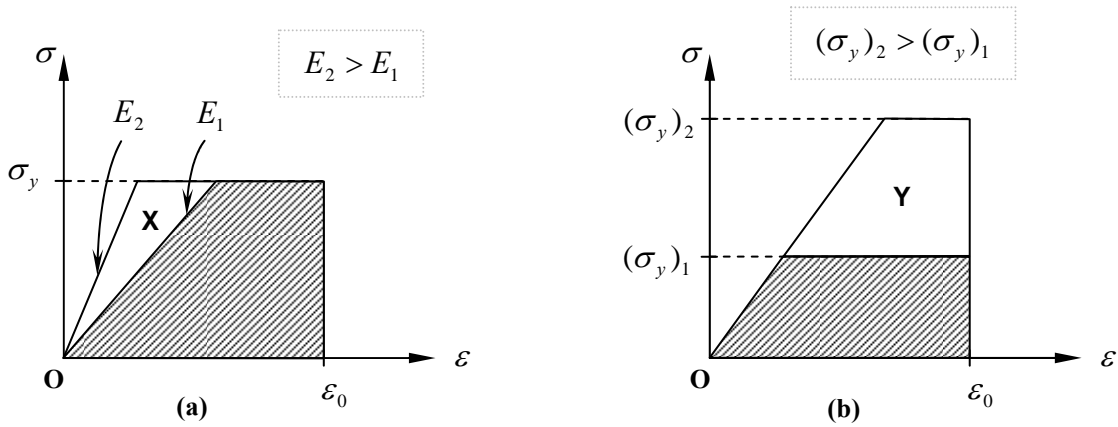


Figure 26: Stress-strain diagram to illustrate the effect of changing (a) elastic modulus and (b) yield stress for change in strain energy.

Surface Property

To review the effect of surface property of a material on its scratch resistance, averaged reactions forces are plotted in Figure 27 for various values of the coefficient of adhesive friction. From the figure, the increase in the coefficient of adhesive friction results in an increased tangential force, which is expected since more frictional resistance is generated between the contacting surfaces and additional force is thus

required. However, an opposite trend of a decreasing normal force is noted when there is more friction between the surfaces.

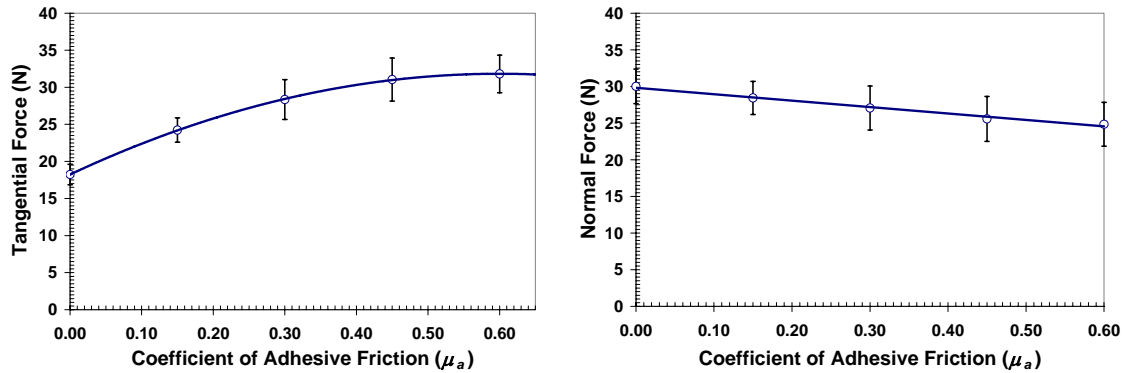


Figure 27: Variation of reaction forces with the coefficient of adhesive friction.

To gain an understanding with regards to the conflicting trends, one can review the forces that are acting on the indenter during the scratch process. Figure 28 illustrates the interaction between the indenter and the substrate during a scratch process, with a free-body diagram showing the different forces acted on the indenter. In Figure 28(a), the interaction between the indenter and substrate has been depicted with care, assuming that the material in the wake of scratch damage has undergone extensive plastic deformation and experiences only minor elastic recovery. This interpretation is substantiated by the results that are presented in the next section. In the free-body diagram, the forces, P and F , are the normal and tangential forces imposed on the indenter for the scratching action while the overall resistance from the material is

denoted by the force, R and f is the frictional force on the indenter. Through resolving and balancing of forces on the indenter, it can be readily concluded with the needed explanation that when there is more frictional resistance at the surface, the tangential force increases while the normal force is reduced accordingly.

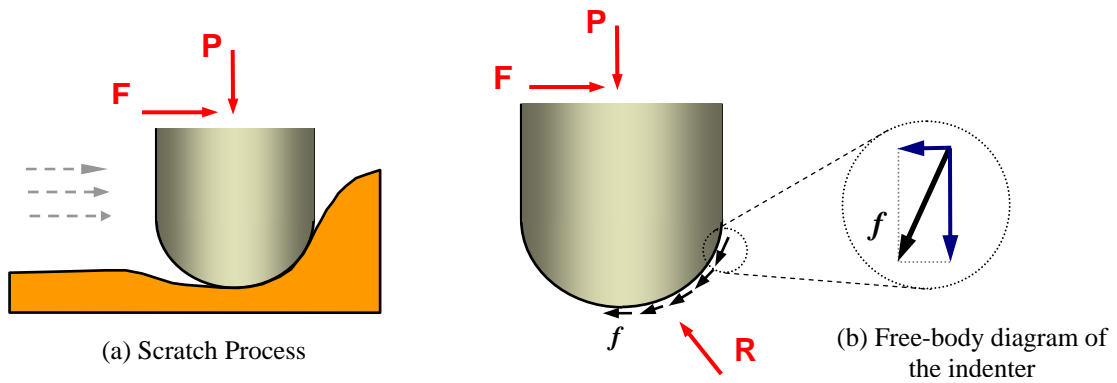


Figure 28: (a) Interaction between indenter and substrate and (b) forces acting on the indenter.

PARAMETRIC STUDY: SCRATCH VISIBILITY

For the quantification of scratch visibility, a simplistic approach is taken to examine the residual scratch depth profile at the end of the scratch process. Herein, it is argued that the greater the residual scratch depth is, it is easier for the reflected light from the scratch groove to be scattered in a pronounced manner to cause an increase in scratch visibility [64]. Presented in Figure 29(a – c) are the residual scratch depth profiles at the end of the scratch step for various values of elastic modulus, yield stress and shear modulus, respectively. From the scratch depth profiles in Figure 29, it is noted that there is only a small amount of elastic recovery in the material after the scratch

deformation. This observation substantiates the drawing in Figure 28(a) to depict the amount of interaction between the indenter and substrate and therefore validates the consideration of forces on the indenter in Figure 28(b). It can be observed from the figures that increasing the elastic modulus results in a lesser elastic recovery in the scratched materials while raising the level of yield stress promotes elastic recovery. Just like the trend for scratch resistance, varying the Poisson's ratio of a material has no observable influence on the residual scratch depth or scratch visibility.

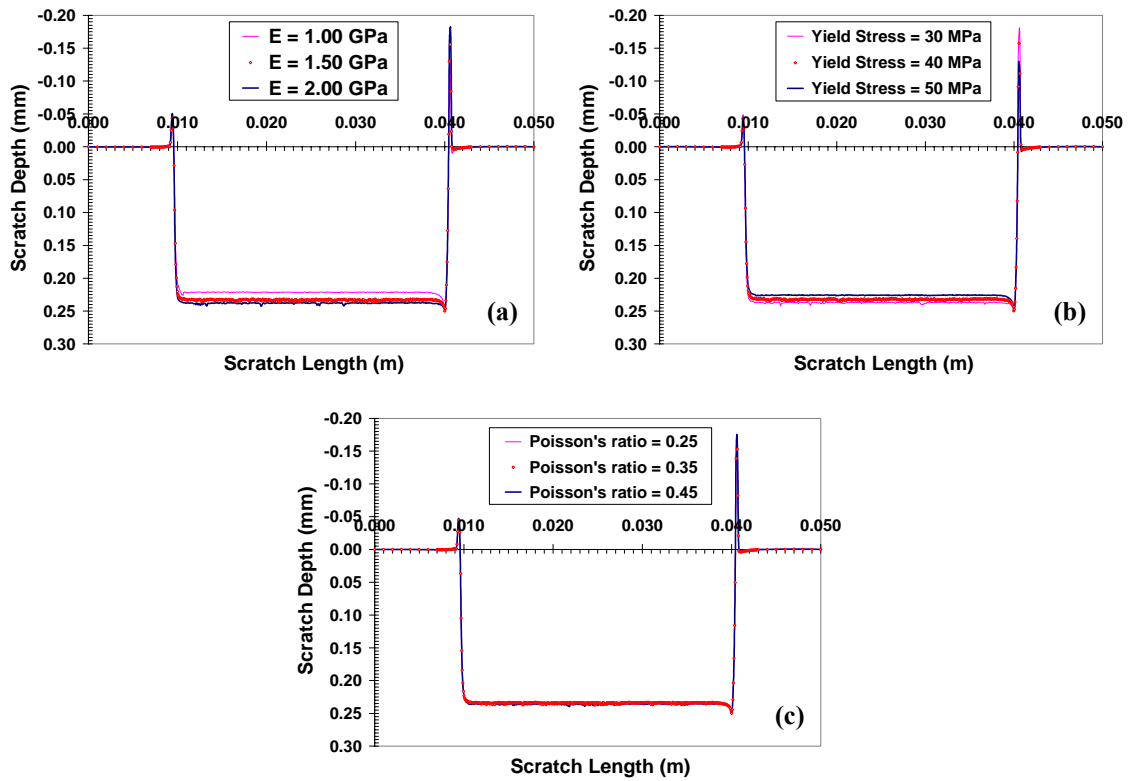


Figure 29: Variation of scratch depth profiles with (a) elastic modulus; (b) yield stress; and (c) Poisson's ratio.

To understand why modifying the elastic modulus or yield stress can bring about a change in the residual scratch depth (scratch visibility) [64], stress-strain diagrams used for explaining the improved scratch resistance can again be referred to. Due to the constant scratch depth imposed by the indenter during the scratch process, scratched materials yield and undergo plastic deformation until the strain level reaches a maximum value of ε_0 . Beyond that, the indenter leaves the materials and unloading occurs. Based on this discussion, one can follow the progression of stress paths for different elastic moduli shown in Figure 30(a). Illustrated by bold arrows in the figure, the recovery paths show that a higher elastic modulus yields a lesser strain recovery as compared to its lower counterpart. On the other hand for the same elastic modulus, strain recovery is more pronounced for materials with higher yield stress, as indicated in Figure 30(b). With this, the mechanistic explanation is provided to reason the trend of the change in scratch visibility with regards to the variation of the elastic modulus and yield stress.

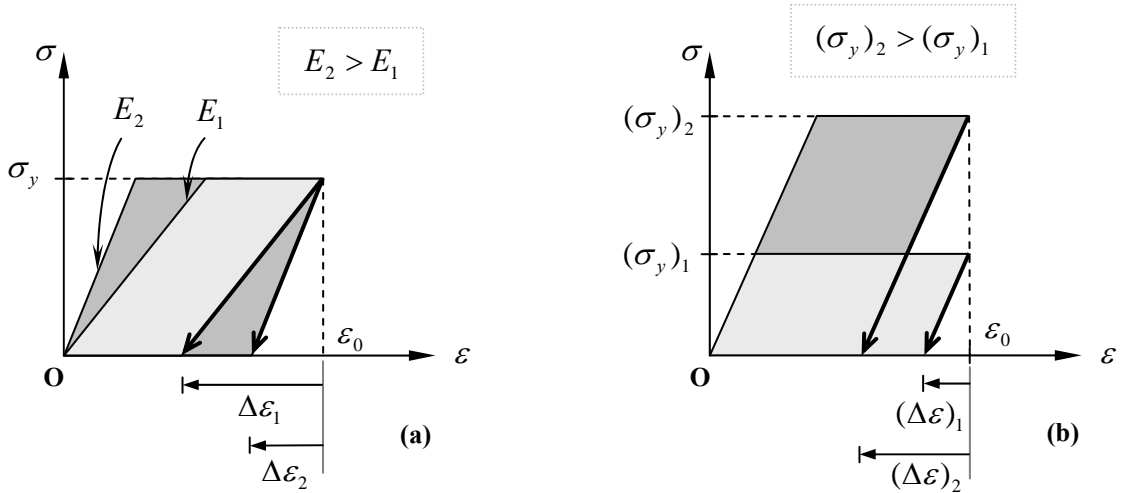


Figure 30: Stress-strain diagram to illustrate the effect of changing (a) elastic modulus and (b) yield stress for elastic recovery.

CONCLUDING REMARKS

To evaluate the scratch performance of a material, dual definitions, namely, scratch resistance and scratch visibility, are introduced in this chapter. Based on these definitions, parametric studies are performed using finite element analysis (FEA) to evaluate the influence of mechanical and surface properties of the material. To conduct the parametric studies using FEA, Load Case D, Mesh D and Material III are considered.

From the discussion of results, it can be concluded that increasing the yield stress, as opposed to the changes in elastic modulus and Poisson's ratio, is an effective way of improving the overall scratch performance of a material, from both the perspectives of scratch resistance and visibility. Though a rise in the elastic modulus of a material helps to improve the scratch resistance, its scratch visibility however increases. Also, introducing more frictional resistance between surfaces, via increasing the coefficient of adhesive friction, increases the tangential force on the indenter, but reduces its normal force.

It should be noted that these conclusions are drawn based on the type of analysis, FE mesh design, the material and surface properties as well as the parametric ranges considered. Further studies should be performed if materials or conditions of analysis are not similar to those adopted in this work. Nevertheless, it is the author's opinion that the dual definitions of scratch performance adopted in this study are useful in assisting material engineers to identify and evaluate critical scratch parameters in designing better scratch-resistant products.

CHAPTER VI

RUBBER ELASTICITY

Rubber can be considered as one of most researched and well understood polymeric materials due to its early discovery and wide range of applications. This chapter considers the formulation of constitutive laws for rubbery materials. Various considerations, assumptions and derivation of the Gaussian and non-Gaussian rubber network models are reviewed. A new rubber elasticity model, herein referred as *the mixed model*, is proposed that combines the modeling capability of the Gaussian and non-Gaussian rubber network models for an enhancement of the overall prediction accuracy. To be presented in this chapter, comparison of numerical results between various rubber network models and ABAQUS® will demonstrate that the mixed rubber model is a better constitutive model over a wide range of deformation. It is envisioned that this material constitutive modeling work on rubbery material allows one to extend the effort to amorphous materials since both materials share a similar network-type morphological structure.

RUBBER NETWORK

To describe the elasticity of elastomeric materials, the approach commonly taken by researchers follows that outlined by Treloar in his well-cited monograph on rubber elasticity [40]. Prior to the derivation of rubber elasticity models, the conditions that constitute a rubber-like elasticity are first reviewed. For a material to behave in a

rubber-like manner under mechanical loadings, it must exhibit the following three characteristics:

- (i) there must be a presence of long-chain molecules with free-rotating links;
- (ii) there are weak secondary forces between the chain molecules;
- (iii) the chain molecules are interlocked with one another at isolated locations along their chain length, creating a three-dimensional network.

Natural rubber or poly-isoprene, like most other polymers, consists of long-chain macromolecules with isoprene as the repeating unit and typically has molecular weights in the range of 1,000,000 g/mol. In its naturally occurring form, rubber is soft and sticky with a low melting temperature of approximately 30°C and has very little practical usage. This is because natural rubber is highly amorphous and has virtually no chemical cross-linking between the chain molecules to provide significant resistance or rigidity against thermal agitation and mechanical deformation. Rubber molecules tend to slide over one another and the elasticity of the material is only provided through weak van der Waal's forces of attraction and physical entanglements between molecules. Through a process called vulcanization where sulfur is introduced to promote chemical cross-linking, elastomeric properties of rubber are substantially enhanced and the network of cross-linked molecules deforms together as a coherent body. Figure 31 shows the chemical structure of a rubber molecule (poly-isoprene) and the chemical cross-linking between rubber molecules and sulfur as a result of vulcanization. Relating to the above three elastomeric properties, it is of no surprise to realize that these properties are motivated

by the morphology structure and mechanical response of vulcanized rubber, the very first form of commercial rubber.

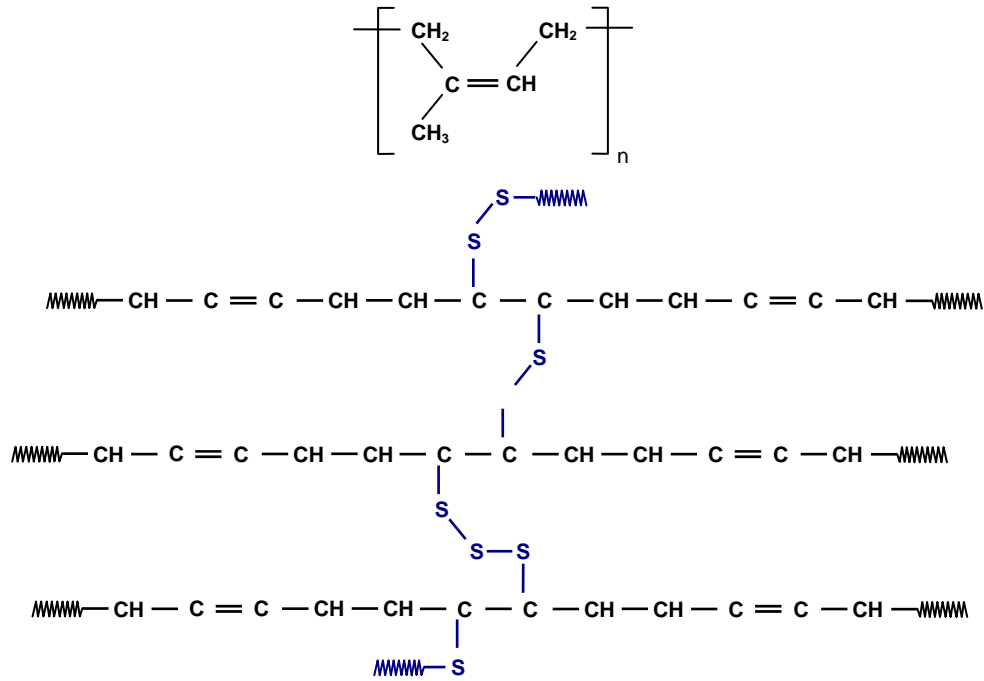


Figure 31: Chemical structure of poly-isoprene (natural rubber) and chemical cross-linking due to vulcanization.

Closely related to the elastomeric properties and important for the derivation of the constitutive theory for rubbers, the five fundamental assumptions of rubber elasticity are stated as [36]:

- (i) A rubber network contains N chains per unit volume;
- (ii) The entropy of the rubber network is the sum of the entropies of each chain;
- (iii) The mean-square end-to-end distance of the network in its unstrained state is equal to the sum of the corresponding distance of each chain;

- (iv) The chains move affinely with the embedded continuum during a deformation process;
- (v) Volume of the continuum remains unchanged under deformation.

A chain referred to herein is defined as the segment of a molecule between two successive points of cross-linkage. The first three assumptions are mathematical simplifications introduced so that the derivation of the constitutive theory remains tractable and conceivable. The fourth assumption of affine deformation is, by the author's opinion, the most critical of all, without which the constitutive law established fails to hold at the continuum level. The last assumption is another mathematical simplification that is inserted to link the strain energy of the rubber network to its stress-strain response. It is demonstrated later in this chapter that the assumption of isochoric (or volume preserving) deformation can be readily relaxed for generality.

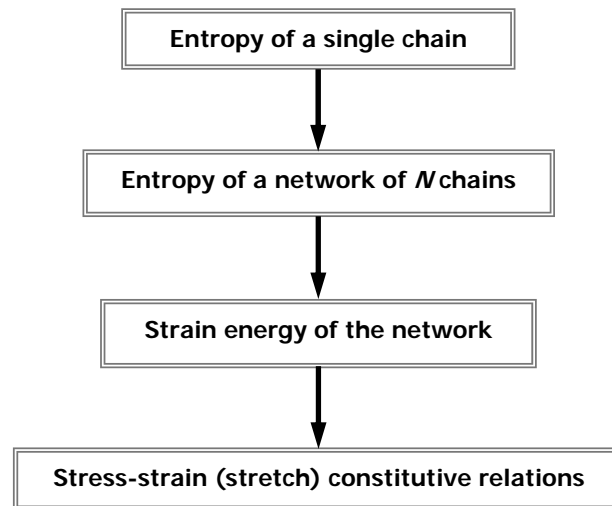


Figure 32: Flow chart for the formulation of the constitutive relations of rubber.

With that and to proceed with the derivation of the constitutive theory for rubbers, the approach taken follows the flow chart presented in Figure 32 where the entropy of a single chain is first calculated. In accordance with the second assumption, the entropy of the rubber network is computed accordingly. Within the framework of thermodynamics, the strain energy of the network is furnished. Finally, the stress-strain or stress-stretch relation of the rubber network is established with the aid of continuum mechanics.

Entropy of a Rubber Chain

It is quite clear from Figure 31 that a cross-linked poly-isoprene or rubber molecule can have an infinitely large number of conformations, taking in account that the single bond enjoys rotational degree of freedom under the constraint of the valence angle between bonds. Furthermore for a macromolecule with high molecular weight like rubber, it is practically impossible to identify precisely the conformation of a molecule. However using statistical theory, it becomes viable to describe the probability of achieving a particular conformation for a molecule.

Now considering a rubber chain with one end fixed in Cartesian space at a reference origin (**O**), as shown in Figure 33. The other end of the molecule is free to occupy any location $A(x, y, z)$ in space. To statistically describe the conformation of the rubber chain, probability density functions $P(x, y, z)$ can be employed. Suppose that the free-end of the rubber chain can move within an infinitesimal control volume (dV) of space, as depicted by the box in Figure 33. Therefore, the probability $p(x, y, z)$ of a chain with its free-end occupying a point in space can be given by

$$p(x, y, z) = P(x, y, z) \cdot dV \quad (5)$$

For generality, the probability density function is not defined explicitly until later. In retrospect, the probability of a conformation of a rubber chain computed in Eq. (5) can be related to the number of conformations available to the chain. This is an important statement of postulation as this aptly allows the introduction of statistical thermodynamics into the derivation.

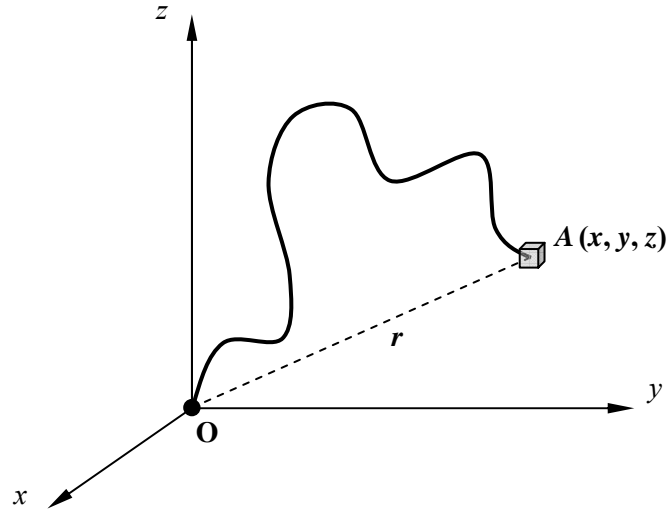


Figure 33: Conformation of a rubber chain in Cartesian space.

Based on the principles of statistical thermodynamics, the entropy of a system is proportional to the logarithm of the number of configurations available at a particular state [40]. To adapt this for the possible conformations of the rubber chain, the entropy,

S of a single chain whose free-end is occupying a random location (x, y, z) in space can be described by

$$S = k \ln[P(x, y, z) \cdot dV], \quad (6)$$

where k is Boltzmann's constant.

Entropy of a Rubber Network

As outlined earlier by the first assumption of rubber elasticity, there are N chains in a rubber network. One can readily compute the entropic change of a rubber network during a deformation with the aid of the second assumption as

$$dS = \sum_{m=1}^N (S_m - S_m^0), \quad (7)$$

where the subscript “ m ” and S_m^0 denote quantities and the entropy of the undeformed m -chain, respectively, while the entropy S_m is to be calculated from Eq. (6).

Strain Energy of a Rubber Network

To relate the evolution of entropy from the conformation change of the rubber network during deformation, the laws of thermodynamics are called upon. The first law of thermodynamics for a closed system asserts that the change in the internal energy (dU) of the system must be balanced by the heat absorbed by the system (dQ) and the work done on it by external forces (dW) [65]. Mathematically, the first law of thermodynamics can be stated as

$$dU = dQ + dW. \quad (8)$$

As in the second law of thermodynamics, the entropy of a system can be related to its heat adsorption as

$$dQ = T dS, \quad (9)$$

where T is the absolute temperature in Kelvin degree. It has been observed by Treloar [36] in his experimental work with rubbers that heat evolves when the material is being stretched and is absorbed upon the release of the force. Treloar further argued that during a deformation process, the conformation change of the rubber network and the heat generated only affect the entropy but constitute no changes to the internal energy [36]. In essence, this statement asserts that

$$dU = 0. \quad (10)$$

In view of Eqs. (8) – (10), one can arrive to

$$dW = -T dS. \quad (11)$$

Now introducing the entropy change of the rubber network, Eq. (7) to Eq. (11),

$$W = -T \sum_{m=1}^N (S_m - S_m^0), \quad (12)$$

In Eq. (12), the work done is treated as an absolute quantity, rather than a change as previously stated in Eq. (11). This treatment remains valid so long as no prior work done has been introduced to the system before the deformation process takes place.

Finally, requiring equality between the work done on the rubber network and its elastic stored energy or strain energy (Π) gives

$$\Pi = W = -T \sum_{m=1}^N (S_m - S_m^0). \quad (13)$$

GAUSSIAN RUBBER NETWORK MODEL

This section considers the choice of the probability density function $P(x, y, z)$ that has hitherto not been defined since its first introduction in Eq. (5). The choice of the probability density functions in general depends on the extent of elongation of the molecular chains [38]. At small strains, it has been shown by Treloar [36,37] in his experimental data that the Gaussian error function gives a good prediction of stress-stretch response of vulcanized rubber. In one-dimensional (1-D) form, the Gaussian function $G(x)$, can be defined as

$$G(x) = \frac{b}{\sqrt{\pi}} \exp(-b^2 x^2), \quad (14)$$

where b is a parameter to be discussed later. The coefficient of the exponential in Eq. (14) is a normalizing factor such that

$$\int_{-\infty}^{\infty} G(x) dx = 1. \quad (15)$$

As an illustration, the Gaussian function is plotted in Figure 34 by setting the value of b to 1. By taking the product of the 1-D form of the Gaussian function in three dimensions, the 3-D Gaussian probability density function can be furnished as

$$P_G(x, y, z) = \left(\frac{b}{\sqrt{\pi}} \right)^3 \exp[-b^2(x^2 + y^2 + z^2)] \equiv \left(\frac{b}{\sqrt{\pi}} \right)^3 \exp(-b^2 r^2), \quad (16)$$

where the subscript “ G ” denotes the Gaussian quantities and $r (= \sqrt{x^2 + y^2 + z^2})$ is the end-to-end distance of the rubber chain, shown in Figure 33. As shown by Treloar [36], b is related to the mean-square length of the unstretched chain ($\overline{r_0^2}$) as

$$\overline{r_0^2} = \frac{3}{2b^2} = nl^2, \quad (17)$$

where n and l are the number and average length of links in a rubber chain, respectively.

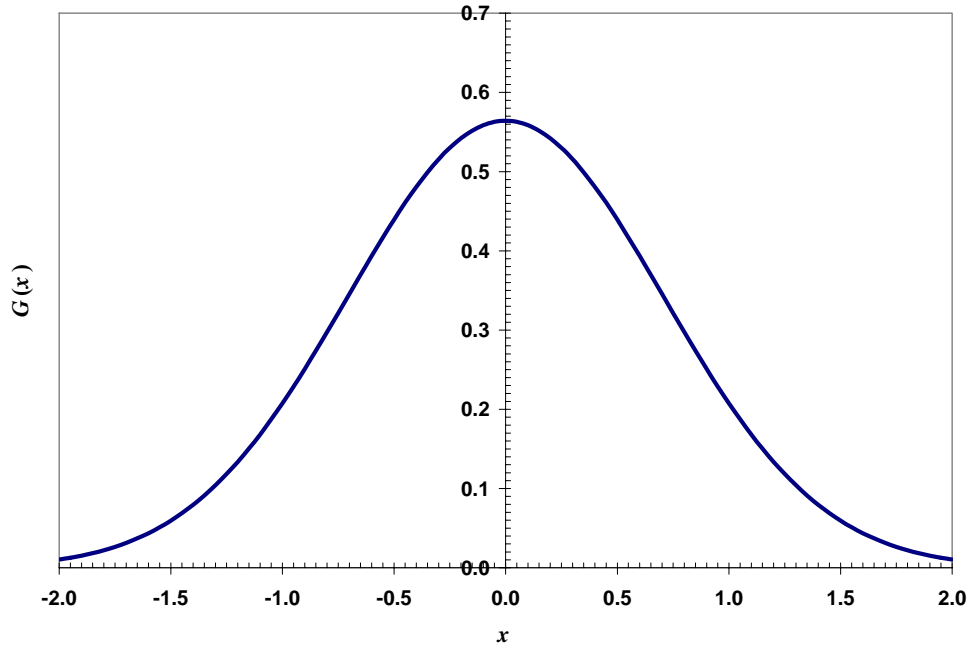


Figure 34: Bell-shaped curve of the Gaussian function ($b = 1$).

After introducing the Gaussian probability density function, the focus is now on furnishing the strain energy of the rubber network under the rubber elasticity framework. To apply the assumption of affine deformation, a link between the deformation of the rubber chain and its continuum body needs to be established. This link can be provided through the kinematical description of a position vector at both continuum and molecular

levels. Suppose that a unit representative continuum cube undergoes deformation or stretching in the three principal directions, as shown in Figure 35.

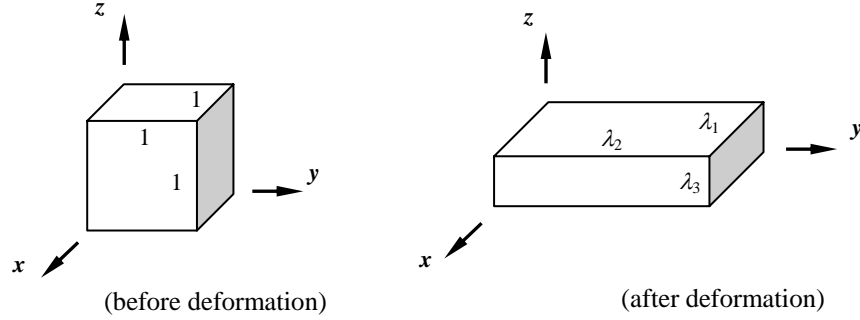


Figure 35: Stretching of the unit continuum cube.

For affine deformation, a rubber chain should deform similarly with the continuum. Spatial coordinates of the chain free end after deformation is updated as

$$x = \lambda_1 x_0, \quad y = \lambda_2 y_0, \quad z = \lambda_3 z_0, \quad (18)$$

where x_0 , y_0 and z_0 are coordinates of the undeformed chain end while λ_1 , λ_2 and λ_3 are the principal stretches.

In view of Eqs. (6), (16) and (18), the entropies of the undeformed (S^0) and (S) deformed rubber can be determined as

$$S^0 = c + k \ln dV_0 - kb^2(x_0^2 + y_0^2 + z_0^2), \quad (19a)$$

$$S = c + k \ln dV - kb^2(\lambda_1^2 x_0^2 + \lambda_2^2 y_0^2 + \lambda_3^2 z_0^2), \quad (19b)$$

where $c = 3k \ln(b/\sqrt{\pi})$. With the chain entropies, the strain energy of the rubber network can be established using Eqs. (13) and (19) as

$$\begin{aligned}
\Pi_G &= kb^2T \sum_{m=1}^N \left[\lambda_1^2 x_0^2|_m + \lambda_2^2 y_0^2|_m + \lambda_3^2 z_0^2|_m - (x_0^2|_m + y_0^2|_m + z_0^2|_m) \right] - kT \sum_{m=1}^N \ln \left(\frac{dV}{dV_0} \right)_m \\
&= kb^2T \left[\lambda_1^2 \sum x_0^2 + \lambda_2^2 \sum y_0^2 + \lambda_3^2 \sum z_0^2 - \sum (x_0^2 + y_0^2 + z_0^2) \right] - kNT \ln \left(\frac{dV}{dV_0} \right). \quad (20)
\end{aligned}$$

Note that the summation index in Eq. (20) has been dropped for convenience and the summation is always taken from 1 to N , unless otherwise stated. Note that the assumption of affine deformation has been applied to the summation of volumetric change to obtain the result in Eq. (20). As a simplification, it is considered that

$$\sum x_0^2 = \sum y_0^2 = \sum z_0^2 = \frac{1}{3} \sum r_0^2. \quad (21)$$

where $r_0^2 = x_0^2 + y_0^2 + z_0^2$. As postulated in the third assumption, the mean-square end-to-end distance of the rubber network can be derived from the corresponding distance of each chain as

$$\sum r_0^2 = N \overline{r_0^2}. \quad (22)$$

Combining Eqs. (20) – (22), it can be ascertained that

$$\Pi_G = \frac{b^2}{3} kNT \overline{r_0^2} (\lambda_1^2 + \lambda_2^2 + \lambda_3^2 - 3) - kNT \ln J. \quad (23)$$

where $J = dV/dV_0 = \lambda_1 \lambda_2 \lambda_3$. Next considering the relation between b and $\overline{r_0^2}$ in Eq. (17), the final form of the strain energy for the Gaussian rubber network model becomes

$$\Pi_G = \frac{1}{2} \mu (\lambda_1^2 + \lambda_2^2 + \lambda_3^2 - 3) - \mu \ln J, \quad (24)$$

where $\mu = kNT$ is the initial shear modulus. Hitherto, the assumption of isochoric deformation has not been applied to derive the Gaussian rubber network model. If the

deformation process incurs no change in the continuum volume, *i.e.*, $J=1$, the familiar form of the incompressible Gaussian rubber network model is recovered as

$$\hat{\Pi}_G = \frac{1}{2}\mu(\lambda_1^2 + \lambda_2^2 + \lambda_3^2 - 3), \quad (25)$$

where the cap symbol denotes incompressible quantities. Note that the incompressible Gaussian rubber network model is also sometimes referred as the *neo-Hookean* model.

NON-GAUSSIAN RUBBER NETWORK MODELS

As mentioned, the applicability of the Gaussian network model is only valid at small strains or when the extended length of the rubber chain is significantly less than the maximum extended chain length [36,38],

$$r \ll nl. \quad (26)$$

When r approaches $0.4nl$, the stretching behavior of rubber chains becomes significantly non-Gaussian [38]. Hence in such large strain (stretch) regime, it is necessary to adopt non-Gaussian functions. A survey of relevant literature shows that the work by Kuhn and Gr \ddot{u} n [36] has been adopted extensively to establish the 3-chain [39], 4-chain [40], 8-chain [41], full-chain [34] and averaged-stretch [42] non-Gaussian network models for rubber. The non-Gaussian probability density function proposed by Kuhn and Gr \ddot{u} n [36] can be stated as follows:

$$P_{NG}(r) = \exp\left\{C - n\left[\frac{r\beta}{nl} + \ln\left(\frac{\beta}{\sinh \beta}\right)\right]\right\} \quad (27)$$

where C is a constant and the subscript “NG” denotes non-Gaussian quantities. β is the inverse Langevin function of $\bar{\lambda}$, i.e.,

$$\beta = L^{-1}(\bar{\lambda}) \quad (28a)$$

where $\bar{\lambda}$ is a stretch measure to be defined separately for each network model and the Langevin function is stated as

$$L(x) = \coth x - \frac{1}{x}. \quad (28b)$$

Entropy and Strain Energy of Non-Gaussian Rubber Network

Based on the Kuhn-Grün function, one can calculate the entropy of a rubber chain before and after a deformation as

$$S^0 = kC + k \ln dV_0 - nk \left[\frac{r_0 \beta_0}{nl} + \ln \left(\frac{\beta_0}{\sinh \beta_0} \right) \right], \quad (29a)$$

$$S = kC + k \ln dV - nk \left[\frac{r\beta}{nl} + \ln \left(\frac{\beta}{\sinh \beta} \right) \right]. \quad (29b)$$

With this and using Eq. (13), the strain energy of the non-Gaussian rubber network with N number of chains can be established as

$$\begin{aligned} \Pi_{NG} &= \hat{C} + nkT \sum_{m=1}^N \left[\frac{r\beta}{nl} + \ln \left(\frac{\beta}{\sinh \beta} \right) \right]_m - kT \sum_{m=1}^N \ln \left(\frac{dV}{dV_0} \right)_m \\ &= \hat{C} + nkNT \left[\frac{r\beta}{nl} + \ln \left(\frac{\beta}{\sinh \beta} \right) \right] - kNT \ln J. \end{aligned} \quad (30)$$

where \hat{C} accounts for the conformational entropy of undeformed rubber chains. Other than considering isochoric deformation, it is also assumed in the derivation of Eq. (30)

that the entropic contribution to the strain energy is the same for every rubber chain. To yield the stress-strain relation, the derivative of the strain energy is to be taken with respect to the principal stretch. Hence, the constant \hat{C} , can be dropped from Eq. (30) without any loss of generality. Finally in view of Eq. (17), the strain energy of a general non-Gaussian rubber network model can be furnished as

$$\Pi_{NG} = n\mu \left[\frac{r\beta}{\bar{r}_0\sqrt{n}} + \ln\left(\frac{\beta}{\sinh \beta}\right) \right] - \mu \ln J, \quad (31)$$

and its incompressible counterpart is given by

$$\hat{\Pi}_{NG} = n\mu \left[\frac{r\beta}{\bar{r}_0\sqrt{n}} + \ln\left(\frac{\beta}{\sinh \beta}\right) \right]. \quad (32)$$

Comparison between Gaussian and Kuhn-Grün Functions

Like the Gaussian function, the formulation of the Kuhn-Grün probability density function is also motivated by the quest to statistically predict the end-to-end distance of the rubber chain. As presented earlier, the Gaussian approach determines the chain length through its prediction of the most probable spatial position of the free end. However in the Kuhn-Grün approach, the chain length is computed with a different philosophy, which is based on the probability distribution of the link angles with respect to the length **OA** in Figure 33.

Besides that, it is interesting to see how the Kuhn-Grün function performs at small strains, as compared to its Gaussian counterpart. According to Kuhn and Kuhn [36], the Kuhn-Grün function, Eq. (27) can be expressed in a series form as

$$\ln P_{NG}(r) = C - \frac{3}{2} \left(\frac{r^2}{nl^2} \right) \left[1 + \frac{3}{10} \left(\frac{r}{nl} \right)^2 + \frac{33}{175} \left(\frac{r}{nl} \right)^4 + \frac{513}{3500} \left(\frac{r}{nl} \right)^6 + \dots \right] \quad (33)$$

Substituting Eqs. (16) and (17) into Eq. (33) yields

$$\ln P_{NG}(r) = C + [\ln P_G(r) + \gamma] \left\{ 1 - \frac{1}{5n} [\ln P_G(r) + \gamma] \left[1 + \frac{22}{35} \left(\frac{r}{nl} \right)^2 + \frac{171}{350} \left(\frac{r}{nl} \right)^4 + \dots \right] \right\} \quad (34)$$

where $\gamma = 3 \ln(\sqrt{\pi}/b)$. When $r/(nl)$ is small and ignoring higher-order terms, Eq. (34) reduces to

$$\begin{aligned} \ln P_{NG}(r) &\cong C + \ln P_G(r) + \gamma - \frac{1}{5n} [\ln P_G(r) + \gamma]^2 \\ &\cong \tilde{C} + \left(1 - \frac{2\gamma}{5n} \right) \ln P_G(r) \end{aligned} \quad (35)$$

where $\tilde{C} = C + \gamma - \gamma^2/(5n)$. Since b must be less than $\sqrt{\pi}$ from Eq. (16) and γ must be always positive, it is evident from Eq. (35) that the Kuhn-Grün probability density function gives a lower prediction of the chain length than that of the Gaussian function at small strains. This conclusion is different from that arrived by Treloar [36] that at small strains, the Kuhn-Grün function provides an *equivalent* prediction as that of the Gaussian. This statement is further substantiated with numerical solutions later in this chapter.

3-Chain and 8-Chain Non-Gaussian Models

Of the various non-Gaussian rubber network models, the 3-chain [39] and 8-chain models [41] possess a simpler mathematical framework that allows easy computational implementation and still has a good accuracy in modeling the elastic response of rubbers. The principle of these N -chain models goes one step further in the

theory of rubber elasticity by explicitly specifying the initial orientation of the N chains. In the idealization of the 3-chain model, all the rubber chains are initially oriented along the three mutually orthogonal principal directions of deformation, as shown in Figure 36(a). For the 8-chain model, the chains, as illustrated in Figure 36(b), are idealized to emanate diagonally from the center of a unit cube to each of its eight corners.

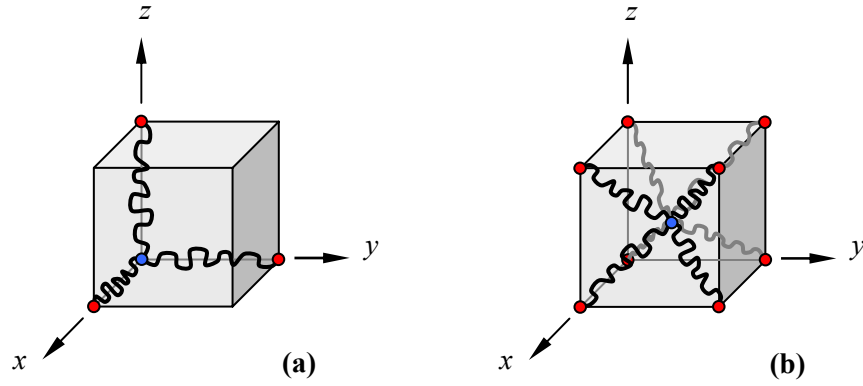


Figure 36: (a) 3-chain rubber model; (b) 8-chain rubber model.

For the 3-chain model, the deformed chain length along each principal axis (i) can be characterized as

$$r_i = \lambda_i \bar{r}_0. \quad (36)$$

To compute β , the relative principal stretch ($\bar{\lambda}_i$) is given by

$$\bar{\lambda}_i = \frac{\lambda_i}{\sqrt{n}}. \quad (37)$$

As a discussion in [42], it may be argued that the 3-chain model should be extended to a 6-chain model to completely represent the different quadrants in space. However, the symmetry present in the 6-chain model readily reduces itself to a 3-chain model. Hence, the 3-chain model is adequate to represent the chain deformation in the considered orthogonal directions. Assuming that the rubber chains in the network are evenly distributed in the three orthogonal directions, one can furnish the strain energy for the compressible 3-chain rubber network from Eqs. (31), (36) and (37) as

$$\Pi_{3\text{-chain}} = \frac{n\mu}{3} \sum_{i=1}^3 \left[\bar{\lambda}_i \beta_i + \ln \left(\frac{\beta_i}{\sinh \beta_i} \right) \right] - \mu \ln J, \quad (38)$$

where $\beta_i = L^{-1}(\bar{\lambda}_i)$.

For the 8-chain model shown in Figure 36(b), Beatty [42] demonstrated mathematically that the principal stretches in each of the eight chains are invariant or the same, *if and only if* the chains extend from the geometric center to all its corners of a uniform polyhedron; examples of uniform polyhedrons are cubes and tetrahedrons. With this and considering the direction vector of the chains, one can readily deduce that the deformed chain length is

$$r_c = \lambda_c \bar{r}_0, \quad (39)$$

where $\lambda_c = \sqrt{(\lambda_1^2 + \lambda_2^2 + \lambda_3^2)/3}$ and the relative chain stretch,

$$\bar{\lambda}_c = \frac{\lambda_c}{\sqrt{n}}, \quad (40)$$

In view of Eqs. (31), (39) and (40), it is surprising to obtain a relatively simpler mathematical expression for the strain energy of the compressible 8-chain model as

$$\Pi_{8\text{-chain}} = n\mu \left[\bar{\lambda}_c \beta_c + \ln \left(\frac{\beta_c}{\sinh \beta_c} \right) \right] - \mu \ln J, \quad (41)$$

where $\beta_c = L^{-1}(\bar{\lambda}_c)$.

Evaluation of Inverse Langevin Function

To implement any of the above-stated non-Gaussian rubber network models, Eqs. (38) and (41), it is essential to be able to compute the inverse Langevin function accurately since there is no exact form to the function. As compiled by Horgan and Saccomandi [66], there are generally two types of analytical solutions to approximate the inverse Langevin function, *i.e.*, rational polynomials and series solutions.

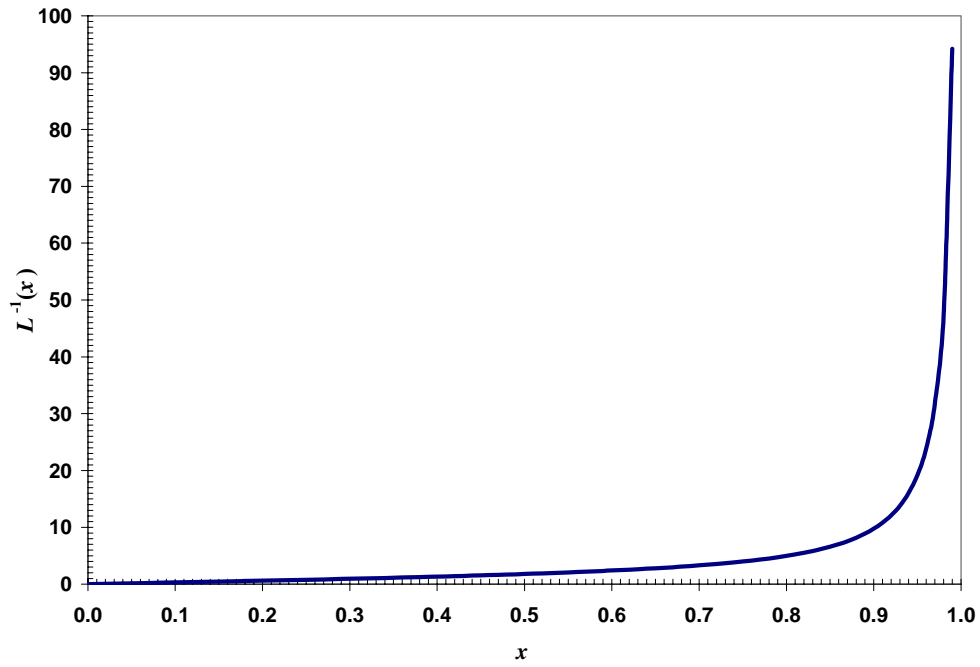


Figure 37: Inverse Langevin function and its singularity at $x = 1$.

The rational polynomials for the inverse Langevin function are usually obtained empirically [36,67] or using Padè approximant [68] while series solutions are derived based on the series expansion of Eq. (28) and comparing algebraic coefficients of a selected number of terms for the inverse function [36,69]. As illustrated in Figure 37, inverse Langevin function has a singularity when x approaches 1, of which Horgan and Saccomandi [66] pointed out that such a singularity can be captured more accurately using rational polynomials than the series solutions.

On the approximation of inverse Langevin function by rational polynomials, Treloar [36] suggested the first empirical form as

$$L^{-1}(x) \cong \frac{3x}{1 - \left(\frac{3}{5}x^2 + \frac{1}{5}x^4 + \frac{1}{5}x^6 \right)}, \quad (42)$$

and the other from another work of his [67],

$$L^{-1}(x) \cong \frac{3x}{1 - \left(\frac{3}{5}x^2 + \frac{36}{175}x^4 + \frac{108}{875}x^6 \right)}. \quad (43)$$

Using Padè approximant, Cohen [68] proposed a simpler rational polynomial

$$L^{-1}(x) \cong \frac{x(3 - x^2)}{1 - x^2}. \quad (44)$$

In terms of series solutions, the first eight terms of the expansion for the inverse Langevin function are given as

$$\begin{aligned} L^{-1}(x) \cong & 3x + \frac{9}{5}x^3 + \frac{297}{175}x^5 + \frac{1539}{875}x^7 + \frac{126117}{67375}x^9 + \frac{43733439}{21896875}x^{11} \\ & + \frac{231321177}{109484375}x^{13} + \frac{20495009043}{9306171875}x^{15} + \dots \end{aligned} \quad (45)$$

The first four terms of the series expansion in Eq. (45) can be attributed to Treloar [36,67] while Anand [69] added two more terms to the series. The last two terms of the series have been independently derived in this study.

From the suggested approximants, the form of rational polynomials Eq. (42), by Treloar [36] and Eq. (44), by Cohen [68] capture exactly the singularity of the inverse Langevin function. To access the accuracy in the approximation of the inverse Langevin function, one can refer to Figure 38(a) and (b) for the comparison of percentage errors by the various methods. Since there are no exact values of the inverse Langevin function for comparison, the errors presented are computed based on how well the calculated values of the inverse Langevin function can recover the original values used for the calculation in Eq. (28). From Figure 38(a), one can observe that near the region of singularity ($0.9 \leq x < 1$), rational polynomials Eqs. (42) – (44) expectedly yield better accuracy than the series solutions. Though Eq. (44) by Cohen [68] may be the most accurate in predicting values around the region of singularity, its accuracy over other regions is generally poor. In the range of $0 \leq x < 0.6$, it is evident from Figure 38(b) that the accuracy of the series solutions of using 6 or 8 terms is superior to those of rational polynomials. However in terms of overall accuracy, the rational polynomial, Eq. (42) has the lowest percentage error over the entire domain among various methods. For the purpose of implementing non-Gaussian models in this work, the rational polynomial of Eq. (42) is adopted for evaluating the inverse Langevin function.

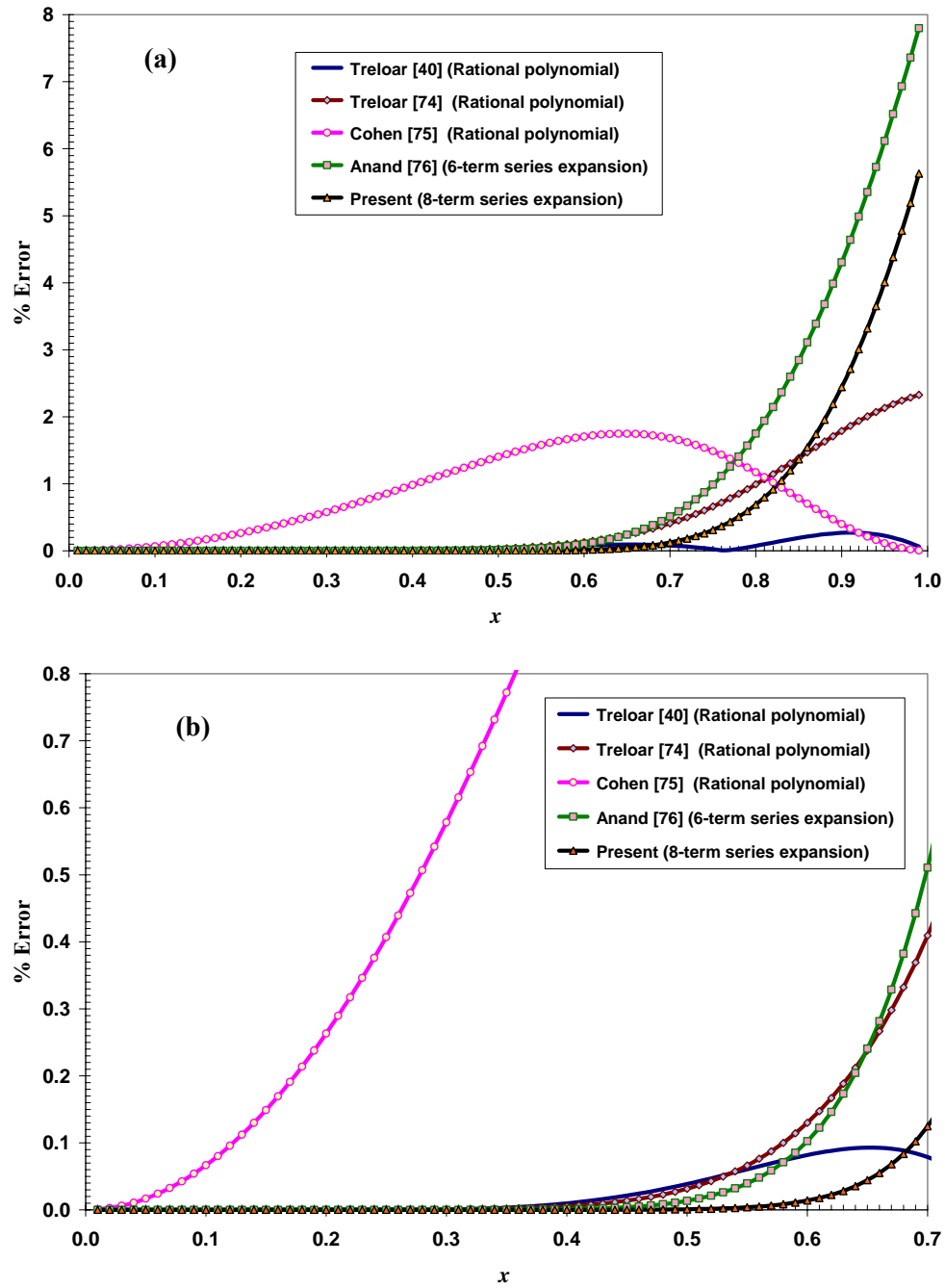


Figure 38: Comparison of percentage error in approximation over (a) $0 \leq x < 1$; (b) $0 \leq x \leq 0.7$.

STRESS-STRETCH CONSTITUTIVE EQUATIONS

With the strain energy (Π) of the Gaussian and non-Gaussian rubber network models derived, it now remains to establish the constitutive equations so as to link the stresses to the state of deformation, *i.e.*, strains or stretches. Under the framework of finite elasticity, it is assumed that the material of concern in this study, rubber, is hyperelastic, isotropic and homogeneous. For material isotropy and hyperelasticity, it follows that the strain energy of the material can be expressed as [70]

$$\Pi = \Pi(I_1, I_2, I_3) \quad (46)$$

and the corresponding stress tensor ($\boldsymbol{\sigma}$) is given by [71]

$$\boldsymbol{\sigma} = \chi_0 \mathbf{I} + \chi_1 \mathbf{B} + \chi_{-1} \mathbf{B}^{-1}, \quad (47)$$

where \mathbf{I} is the identity tensor, \mathbf{B} is the left Cauchy-Green deformation tensor and

$$\chi_0 = \frac{2}{\sqrt{I_3}} \left(I_2 \frac{\partial \Pi}{\partial I_2} + I_3 \frac{\partial \Pi}{\partial I_3} \right), \quad (48a)$$

$$\chi_1 = \frac{2}{\sqrt{I_3}} \frac{\partial \Pi}{\partial I_1}, \quad (48b)$$

$$\chi_{-1} = -2\sqrt{I_3} \frac{\partial \Pi}{\partial I_2}. \quad (48c)$$

In Eqs. (48), the principal invariants of \mathbf{B} can be expressed in terms of the principal stretches as

$$I_1 = \lambda_1^2 + \lambda_2^2 + \lambda_3^2, \quad (49a)$$

$$I_2 = \lambda_1^2 \lambda_2^2 + \lambda_2^2 \lambda_3^2 + \lambda_1^2 \lambda_3^2 = I_3 \left(\frac{1}{\lambda_1^2} + \frac{1}{\lambda_2^2} + \frac{1}{\lambda_3^2} \right), \quad (49b)$$

$$I_3 = \lambda_1^2 \lambda_2^2 \lambda_3^2 = J^2. \quad (49c)$$

Calculation of $\boldsymbol{\sigma}$ using Eqs. (47) – (49) can be cumbersome since the eigen-principal values of \mathbf{B} may not be known explicitly for a general state of deformation. For simple deformation processes like uniaxial or biaxial extension, the axes of deformation are naturally aligned with the principal directions. Hence, \mathbf{B} is diagonal and its diagonal elements are the principal values, which correspond to the square of the stretches,

$$\mathbf{B} = \begin{pmatrix} \lambda_1^2 & 0 & 0 \\ 0 & \lambda_2^2 & 0 \\ 0 & 0 & \lambda_3^2 \end{pmatrix}. \quad (50)$$

However for an arbitrary state of deformation, it is necessary to first compute the eigen-values and eigenvectors of \mathbf{B} before using Eq. (47) to determine the principal stresses. Finally, the principal stresses are to be transformed from the eigen-space back to the original Cartesian space based on the following transformation

$$\boldsymbol{\sigma} = \mathbf{Q} \cdot \boldsymbol{\sigma}^P \cdot \mathbf{Q}^T, \quad (51)$$

where $\boldsymbol{\sigma}^P$ is the principal stress tensor and \mathbf{Q} is the transformation matrix whose columns correspond to the unit eigen-vectors of \mathbf{B} .

Now suppose the deformation in Cartesian space has been transformed to or coincides with the eigen-space so that Eq. (50) remains valid. Through simple algebraic manipulation, the principal stress (σ_i) can be established from Eqs. (47), (48) and (50) as

$$\sigma_i = \chi_0 + \chi_1 \lambda_i^2 + \chi_{-1} \left(\frac{1}{\lambda_i^2} \right)$$

$$= \frac{2}{\sqrt{I_3}} \left[\lambda_i^2 \frac{\partial \Pi}{\partial I_1} + \left(I_2 - \frac{I_3}{\lambda_i^2} \right) \frac{\partial \Pi}{\partial I_2} + I_3 \frac{\partial \Pi}{\partial I_3} \right]. \quad (52)$$

Evaluating the derivative of the principal invariants in Eq. (49) with respect to the principal stretches yields

$$\frac{\partial I_1}{\partial \lambda_i} = 2\lambda_i, \quad (53a)$$

$$\frac{\partial I_2}{\partial \lambda_i} = \frac{2}{\lambda_i} \left(I_2 - \frac{I_3}{\lambda_i^2} \right), \quad (53b)$$

$$\frac{\partial I_3}{\partial \lambda_i} = \frac{2I_3}{\lambda_i}. \quad (53c)$$

Substituting Eqs. (53) into Eq. (52) readily yields the simplified form of the principal stress-stretch constitutive equations for homogeneous, isotropic, compressible and hyperelastic materials

$$\sigma_i = \frac{\lambda_i}{\sqrt{I_3}} \left(\frac{\partial \Pi}{\partial I_1} \cdot \frac{\partial I_1}{\partial \lambda_i} + \frac{\partial \Pi}{\partial I_2} \cdot \frac{\partial I_2}{\partial \lambda_i} + \frac{\partial \Pi}{\partial I_3} \cdot \frac{\partial I_3}{\partial \lambda_i} \right) = \frac{\lambda_i}{J} \cdot \frac{d\Pi}{d\lambda_i} \quad (54)$$

For incompressible materials ($J = 1$), the principal stress-stretch relations become [71]

$$\hat{\sigma}_i = p + \lambda_i \cdot \frac{d\Pi}{d\lambda_i} \quad (55)$$

where p is a parameter that is to be determined from the boundary conditions.

From the constitutive equations in Eq. (54) and the strain energies in Eqs. (24), (38) and (41), material compressibility can be considered readily in the formulation, which indicates that the last assumption of the rubber elasticity defined in the early part of this chapter can be relaxed easily.

Stress-Stretch Constitutive Equations for Gaussian Model

For a general state of deformation, the principal stress-stretch constitutive relations for compressible Gaussian rubber network model can be derived from Eqs. (24) and (54) as

$$(\sigma_G)_i = \frac{\mu}{J}(\lambda_i^2 - 1), \quad (56a)$$

and for its incompressible counterpart, from Eqs. (25) and (55),

$$(\hat{\sigma}_G)_i = p + \mu \lambda_i^2. \quad (56b)$$

For uniaxial extension where $\lambda_1 = \lambda$ and $\lambda_2 = \lambda_3 = 1/\sqrt{\lambda}$, applying the stress-free boundary condition to $(\hat{\sigma}_G)_2$ or $(\hat{\sigma}_G)_3$ in Eq. (56b) arrives to

$$p = -\frac{\mu}{\lambda}. \quad (57)$$

For pure shear ($\lambda_1 = \lambda$, $\lambda_2 = 1$ and $\lambda_3 = 1/\lambda$), the stress-free boundary condition only holds for $(\hat{\sigma}_G)_3$. Hence,

$$p = -\frac{\mu}{\lambda^2}. \quad (58)$$

Stress-Stretch Constitutive Equations for 3-Chain Non-Gaussian Model

For the 3-chain non-Gaussian rubber network model, the compressible principal stress-stretch constitutive relations can be calculated from Eqs. (28), (38) and (54) to give

$$(\sigma_{3\text{-chain}})_i = \frac{\mu}{3J}(\lambda_i \beta_i \sqrt{n} - 3), \quad (59a)$$

and its incompressible counterpart can be derived from Eqs. (38) and (55) as

$$(\hat{\sigma}_{3\text{-chain}})_i = p + \frac{\mu\sqrt{n}}{3}(\lambda_i\beta_i). \quad (59b)$$

For the uniaxial extension testing, p can be determined as

$$p = -\frac{\mu\sqrt{n}}{3}\left(\frac{\beta_u}{\sqrt{\lambda}}\right), \quad (60)$$

where $\beta_u = L^{-1}\left(\frac{1}{\sqrt{n\lambda}}\right)$. Applying pure shear deformation to the incompressible 3-chain model yields

$$p = -\frac{\mu\sqrt{n}}{3}\left(\frac{\beta_s}{\lambda}\right), \quad (61)$$

where $\beta_s = L^{-1}\left(\frac{1}{\lambda\sqrt{n}}\right)$.

Stress-Stretch Constitutive Equations for 8-Chain Non-Gaussian Model

Now consider the 8-chain non-Gaussian rubber network model and using Eqs. (41) and (54), its compressible principal stress-stretch constitutive relations are

$$(\sigma_{8\text{-chain}})_i = \frac{\mu}{3J}\left(\frac{\lambda_i^2\beta_c}{\bar{\lambda}_c} - 3\right). \quad (62a)$$

For determining the constitutive equations of the incompressible 8-chain rubber network, Eqs. (41) and (54) are employed to give

$$(\hat{\sigma}_{8\text{-chain}})_i = p + \frac{\mu}{3}\left(\frac{\lambda_i^2\beta_c}{\bar{\lambda}_c}\right). \quad (62b)$$

To model uniaxial extension, the appropriate value for p is ascertained as

$$p = -\frac{\mu}{3} \left(\frac{\beta_c}{\lambda \bar{\lambda}_c} \right). \quad (63)$$

For pure shear deformation, it follows that

$$p = -\frac{\mu}{3} \left(\frac{\beta_c}{\lambda^2 \bar{\lambda}_c} \right). \quad (64)$$

NUMERICAL IMPLEMENTATION OF RUBBER MODELS

With the extensive discussion and derivation of the Gaussian and non-Gaussian rubber network models, it is of interest to see how well these two general types of rubber elasticity models can describe the deformation response of rubbers. Experimental stress-strain data for vulcanized rubber (with 8% by weight of sulphur) tested at room temperature (20°C) under different types of deformation by Treloar [36,37] would be adopted as experimental benchmarks for the comparison study.

Presented in Figures 39(a) and (b) are the nominal stress-stretch curves of the considered vulcanized rubber under uniaxial extension and shear deformation. Also illustrated in these figures are the predictions of the elastic response by the Gaussian [Eq. (25)], 3-chain [Eq. (38)] and 8-chain [Eq. (41)] rubber network models. Note that material incompressibility has been considered in the prediction. The nominal stress, f_i used in the figure is defined as the ratio of the applied force, P to the original area, A_0 . Considering the x -direction in Figure 35, it can be derived that

$$\sigma_1 = \frac{P_1}{A} = \frac{P_1}{A_0} \left(\frac{1}{\lambda_2 \lambda_3} \right) = \frac{f_1}{\lambda_2 \lambda_3} \Rightarrow f_1 = \sigma_1 (\lambda_2 \lambda_3) \quad (65)$$

where σ_1 is the Cauchy stress in the x -direction and on the y - z plane. For the uniaxial extension and pure shear deformation discussed in Eqs. (57) and (58), the nominal stress in x -direction is given as

$$f_1 = \frac{\sigma_1}{\lambda} \quad (66)$$

To obtain the parameters for various models, a simple optimization program is used to determine the set of parameters that minimizes the error from the curve-fitting the experimental data for uniaxial extension. Table 7 lists the set of parameters for the Gaussian, 3-chain and 8-chain non-Gaussian rubber network models. From Figure 39(a), it is clear that the prediction by Gaussian rubber network model at large stretches is notably poor, as compared to the other non-Gaussian models. Generally, both non-Gaussian models have very good correlation with the experimental uniaxial extension results over moderate and large stretches. However, a careful examination of the results over small stretches reveals that those from the 3-chain and 8-chain models are consistently lower than the test data, which numerically supports the analytical finding established earlier in Eq. (35). The same trend is again observed for the shear experimental data in Figure 39(b) where the Gaussian model generally performs better at small stretches while the non-Gaussian models have better approximations at large deformation. From the shear test data, the 8-chain non-Gaussian network model shows a slight improvement in the prediction over its 3-chain counterpart.

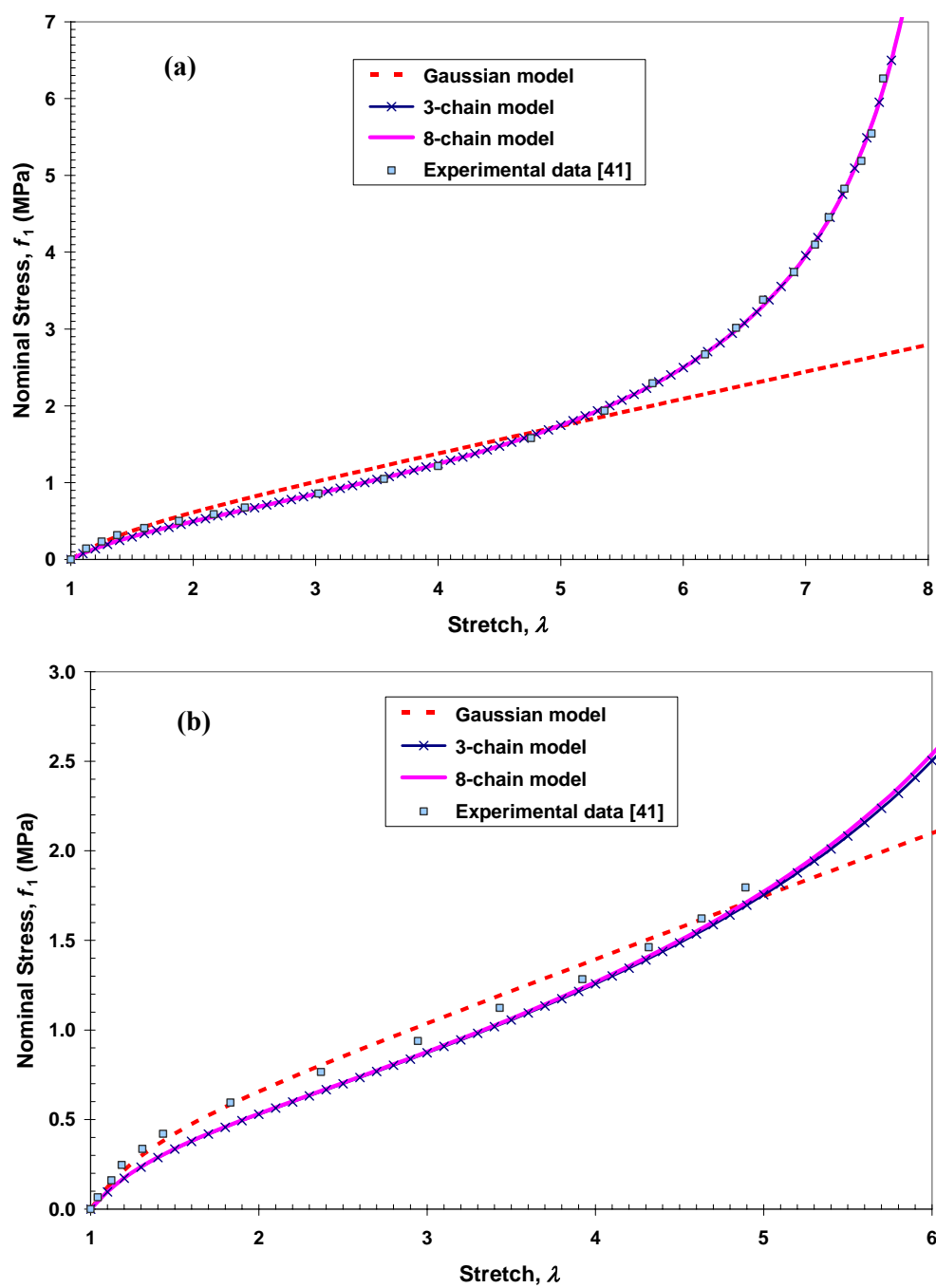


Figure 39: Nominal stress-stretch curves of rubber under (a) uniaxial extension; (b) shear.

Table 7: Parameters for Gaussian, 3-chain and 8-chain rubber network models.

Model	Shear modulus, μ (MPa)	n
Gaussian	0.350	-
3-chain	0.273	76.575
8-chain	0.272	25.603

Mixed Rubber Elasticity Model

From the results presented in Figure 39, especially for the shear data, it is clear that neither the Gaussian nor non-Gaussian rubber network models is capable of capturing the mechanical response of rubbers at both small and large strains on its own. To preserve the predictive capability of both types of rubber network models, it is candid for one to propose that different rubber network models are used for different extent of deformations. However, to simply apply different models over various domains of deformation may introduce kinks or slope discontinuities at the transition. To facilitate a smooth transition of network models across different domains, smoothing functions may be employed. Herein this study, the smoothing function adopted is

$$f(\xi) = \xi^3(10 - 15\xi + 6\xi^2) \quad (67)$$

where $\xi = (\lambda - 1)/(\lambda_{tr} - 1)$ and λ_{tr} is the transition stretch beyond which non-Gaussian models should prevail. The smoothing function in Eq. (67) is selected for its simple numerical implementation and high-order of continuity. As discussed earlier since rubber chains only begin to exhibit non-Gaussian response when $r \approx 0.4nl$ [38], it is reasonable to assume that full non-Gaussian effect only takes place at $r = 0.8nl$, which

is less than the maximum possible chain stretch of nl . In view of Eq. (17), the transition stretch is taken as

$$\lambda_{tr} = 0.8\sqrt{n} \quad (68)$$

Considering only the Gaussian and 8-chain non-Gaussian network models for the mixed model and for the range of stretches ($1 \leq \lambda \leq \lambda_{tr}$), the strain energy of the incompressible mixed model can be computed from Eqs. (32), (41) and (67) as

$$\hat{\Pi}_{Mixed} = (1-f) \cdot \hat{\Pi}_G + f \cdot \hat{\Pi}_{8-chain}. \quad (69)$$

Beyond the transition, the non-Gaussian 8-chain model is applied solely to predict the response of the rubbery material.

Plotted in Figures 40(a) and (b) are the constitutive predictions by the mixed model for the uniaxial extension and shear deformation, together with those by the other two models. From these figures, the mixed model, despite its simple formulation, shows significant improvements in modeling accuracy as compared to the two constituent models, especially for shear data. The implementation of the mixed rubber network model in FORTRAN code is documented in Appendix A-7.

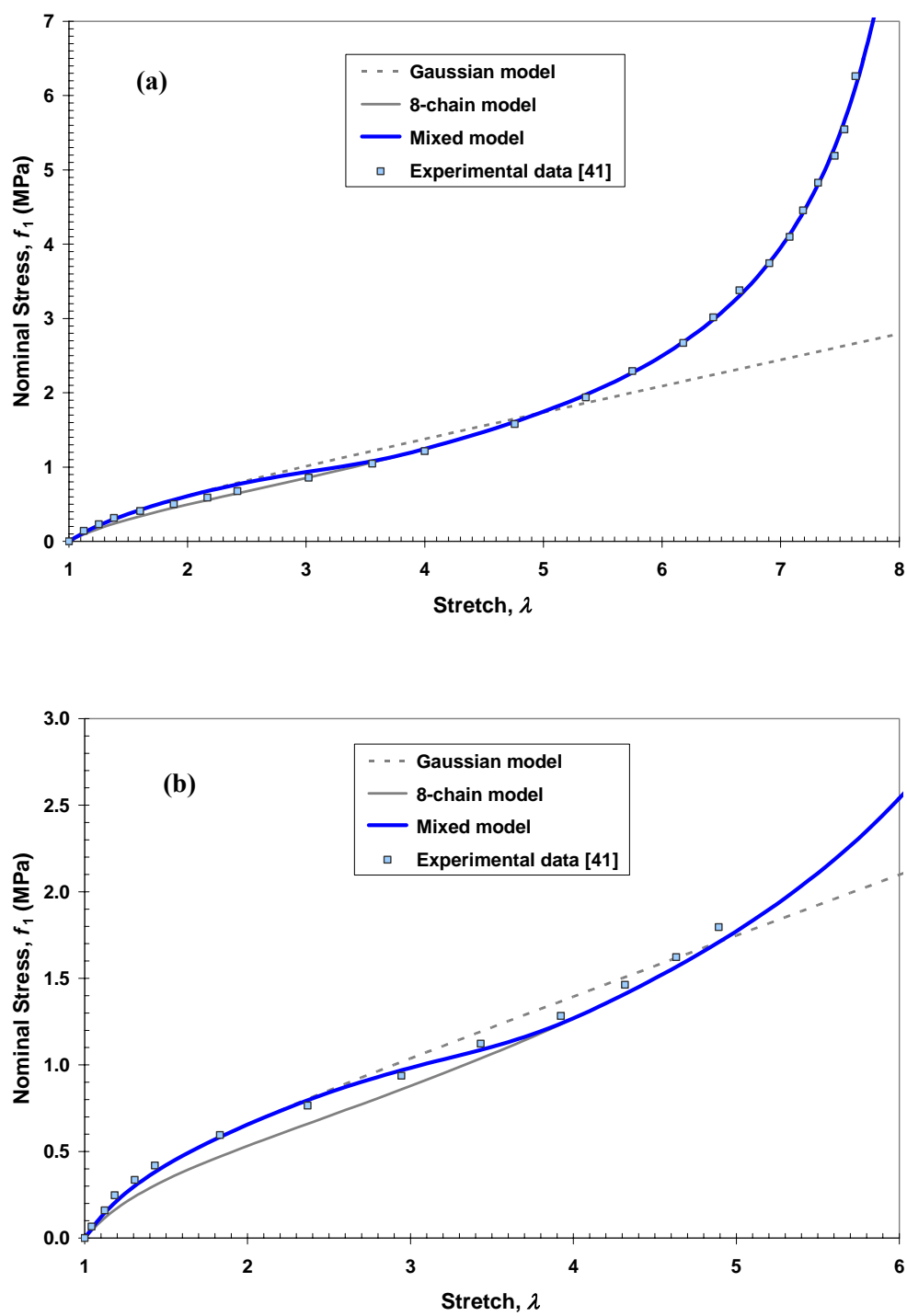


Figure 40: Prediction of stress-stretch behavior by the Gaussian, 8-chain and mixed models.

Material Subroutine for ABAQUS®

One of the most important aspects of constitutive modeling effort is to be able to apply newly formulated constitutive laws to real life problems. For this, it is necessary to integrate constitutive equations as part of the analysis technique adopted to yield solutions to practical engineering problems. Since this dissertation adopts ABAQUS® as the FEA tool to generate numerical results for the scratch problem at hand, it is compelling for one to ask if unique constitutive relations, like the rubber elasticity models introduced earlier, can be incorporated into the ABAQUS® analysis. A key attribute of ABAQUS® is its flexibility to allow users to define material subroutines to analyze problems involving unique or complex materials. As itself, ABAQUS® [46] has also included many commonly known material constitutive laws like the Gaussian and the non-Gaussian 8-chain models, in its material database for users. To particularly include the mixed rubber network model in ABAQUS®, a material subroutine (UHPYER) has been written to define its strain energy to be used for computation and is documented in Appendix A-8.

This material subroutine is written with the flexibility to allow users to select the types of rubber network models among the Gaussian, non-Gaussian 8-chain and mixed models. To suit the inherent structure of the subroutine as required by ABAQUS® [46], two minor modifications have been made to the formulation. The first modification is the change of the parameter (ξ) used in the smoothing function in Eq. (67) to

$$\xi = \frac{I_1 - 3}{\hat{I}_1 - 3}, \quad (70)$$

where \hat{I}_1 is the first principal invariant of \mathbf{B} that corresponds to the transition stretch, $\hat{\lambda}$. The second modification is to adopt the formulation of ABAQUS[®] for material compressibility, based on the work of Kaliske and Rothert [44] for rubbery materials at finite strains. For that, the strain energy of the rubber network model, regardless of the types considered, can be written generally as

$$\Pi = \hat{\Pi} + \frac{1}{D} \left(\frac{J^2 - 1}{2} - \ln J \right), \quad (71)$$

where $D = 2/K$ and K is the bulk modulus of the material. Though the material subroutine is written with the capability to account for material compressibility, the deformation considered for the numerical study essentially remains incompressible, *i.e.*, $J = 1$. For this numerical study, a default value of 20μ is still taken for K , as recommended by ABAQUS[®].

For implementation of the non-Gaussian 8-chain model by ABAQUS[®], the 5-term series expansion in Eq. (45) is adopted for computing the inverse Langevin function, instead of Eq. (42) as considered in this study. To determine the appropriate material parameters for the corresponding non-Gaussian 8-chain model in ABAQUS[®], experimental data are included as inputs, which are fitted with the predicted model by ABAQUS[®]. Using the uniaxial test data from Treloar [36,37], the material parameters determined by ABAQUS[®] are 0.291 MPa and 24.21 for μ and n , respectively. When compared to the corresponding values in Table 7, the slight disparity between the material parameters can be traced to the different inverse Langevin functions used for the rubber model. To further illustrate the importance of the choice of inverse Langevin

function, Figures 41(a) and (b) show the prediction of the stress-stretch curves by ABAQUS[®] and the present work, Eq. (41) for uniaxial and shear deformation, respectively. To generate the results in Figure 41, the set of material parameters determined by ABAQUS[®] was used. One can refer to Appendix A-9 for the ABAQUS[®] input file to execute the necessary analysis. In both figures, there is little or no difference in the predictions by both approaches at small and moderate strains. At large stretches ($> 500\%$), the error in the inverse Langevin function adopted by ABAQUS[®] becomes significant and is demonstrated by the marked difference between the results by ABAQUS[®] and those obtained by the present effort, especially for the uniaxial deformation. Regardless of the choice of the inverse Langevin functions, the overall modeling accuracy of the eight-chain model is still reasonably good, despite its slightly poorer prediction at small strains for shear deformation.

By comparison with the mixed rubber model using the 8-chain material parameters in Table 7, one can see from Figures 42(a) and (b) that the mixed model with the inverse Langevin function from Eq. (43) results in a more accurate model for predicting the mechanical response of rubbers than that provided by ABAQUS[®].

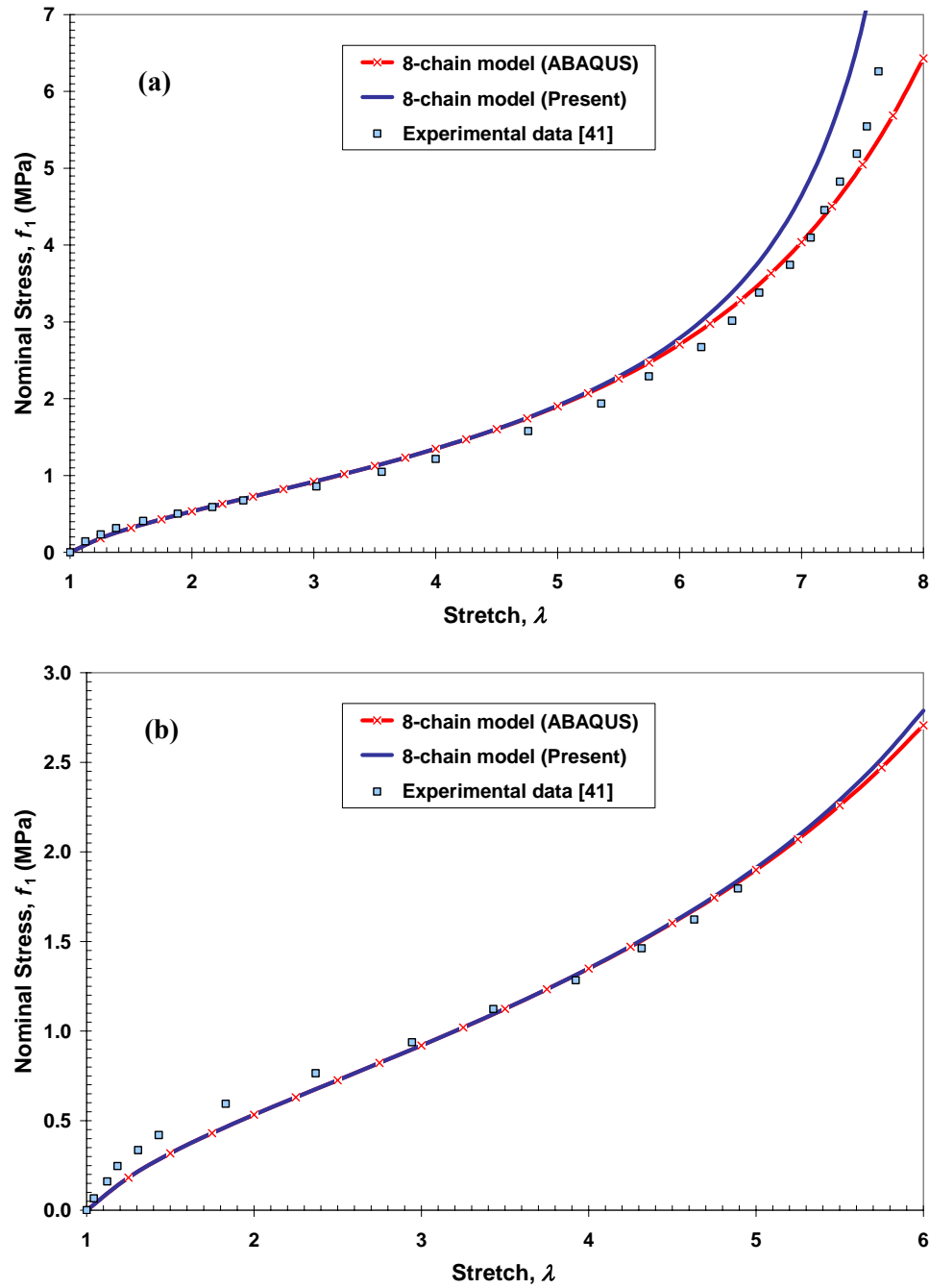


Figure 41: Stress-stretch curves of 8-chain rubber model by ABAQUS[®] and Eq. [41] in (a) uniaxial and (b) shear.

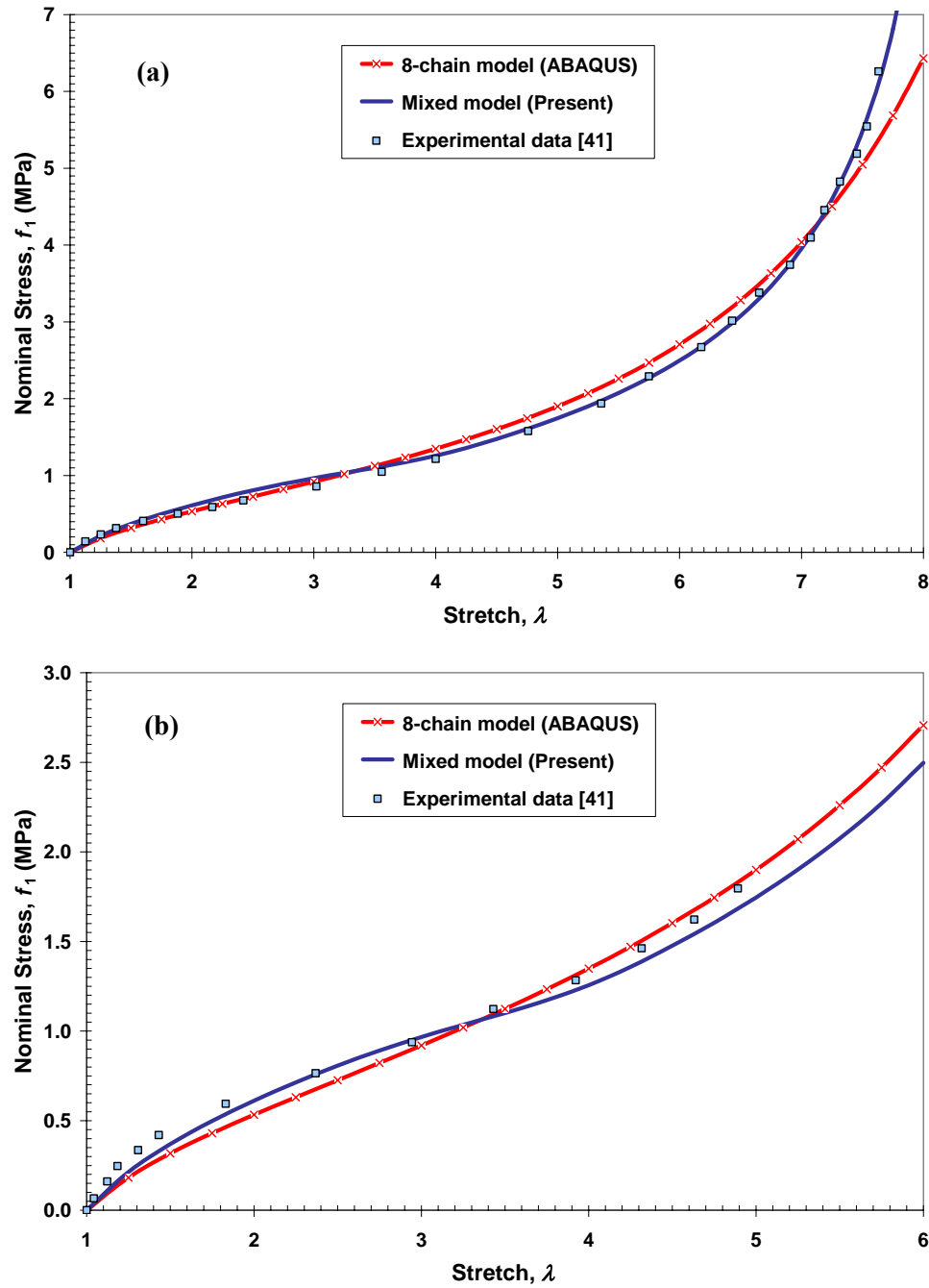


Figure 42: Stress-stretch curves of 8-chain rubber model by ABAQUS® and the mixed model in (a) uniaxial and (b) shear.

CONCLUDING REMARKS

This chapter details the considerations and assumptions in the formulation of Gaussian and non-Gaussian rubber network models. It is shown from numerical results that the Gaussian rubber model is generally applicable at small strains while the non-Gaussian models only predict well for moderate and large deformation. In particular, it was proven analytically that the non-Gaussian models using the Kuhn-Grün function under-predict the constitutive behavior of rubber at small strains, as compared to the Gaussian model. A comparative study is performed to assess the accuracy of various forms of the inverse Langevin function available in the open literature. To take advantage of the predictive powers of both the Gaussian and non-Gaussian rubber networks, a mixed model is proposed to accurately model the mechanical response of rubber over the whole range of deformation. The formulation of the new model is general and can be applied readily to various rubber elasticity models for a better overall prediction of the constitutive response. Implemented in a material subroutine (UHYPER) for ABAQUS[®], numerical results show that the mixed model is a better constitutive model for rubbers than the 8-chain rubber model considered by ABAQUS[®].

CHAPTER VII

CONCLUSION AND FUTURE RESEARCH PLAN

CLOSURE TO PRESENT SCRATCH RESEARCH

This current research effort was initiated to study the scratch deformation of polypropylene (PP) using a numerical technique, *i.e.*, finite element method (FEM) in order to obtain a better understanding of the problem. Taking into account important physical and computational considerations of the scratch problem, the finite element analysis (FEA) performed using commercial software ABAQUS[®], is shown to be qualitatively adequate to describe the material response of PP during a scratch process.

Using the graphical representation of numerical results, the knowledge on the sequential formation of a scratch groove and phenomenological understanding of the mechanism occurred in the scratch deformation are gained. Shear yielding and crazing, the two damage modes of polymers, are carefully reviewed and compared to assess the likelihood of their existence in the scratch problem. From the quantification of plastic damage based on von Mises yielding criterion, ultimate material failure can occur along the scratch path. On the other hand, the application of the critical strain criterion to the FEA solutions allows one to identify the craze initiation around the front of the indenter and along the sides of the scratch groove. Not only do these two damage modes exist in the scratch deformation of PP, but it is indicative from these research findings that they may even compete against each other for dominance.

Parametric studies using FEA were also performed to evaluate the influence of mechanical and surface properties on the scratch performance of polymers. For analysis simplification, the material of concern is taken as elastic-perfectly-plastic. To improve the scratch performance of a material, in terms of scratch resistance and scratch visibility, increasing its yield stress is found to be more effective than manipulating the elastic modulus, Poisson's ratio or the coefficient of adhesive friction.

In an effort to establish a more realistic material constitutive model for PP, rubber network elasticity models are studied. Though rubber or elastomeric material and PP may be dissimilar in their morphological structures, the network structure from the chemical cross-linking of rubber chains is similar to that due to the physical entanglement of polymers chains found in the amorphous phase of semi-crystalline PP. Combining the Gaussian [36] and the eight-chain non-Gaussian models [41], a new mixed rubber network model is proposed in this study. Implemented using FORTRAN codes as well as in the ABAQUS[®] material subroutine, the mixed rubber model is shown to have an improved overall prediction of mechanical response of vulcanized rubbers over a wide range of deformation and have a better performance than the rubber model adopted by ABAQUS[®].

The research endeavor undertaken in this dissertation for the scratch behavior of polypropylene marks a beginning step to unravel rich knowledge while opening up new exciting research frontiers and possibilities in the field. As identified in the respective chapters, the next section compiles these new research ideas, together with a discussion on their related issues and possible course of actions.

NEW SCRATCH RESEARCH DIRECTIONS

By further improving the implementation of FEA like the criteria for ultimate material failure and craze growth, the current numerical approach for scratch analysis can become a powerful quantitative tool for bulk polymeric materials. To achieve this, four future research goals have been identified.

The first research goal is to develop a more representative material constitutive law for the analysis so that a more accurate mechanical response of the polymer under the complex scratch deformation can be captured. In line with the first goal, the second goal is to perform the necessary experimentation to provide essential material parameters for constructing the material constitutive model and to validate the results generated by the scratch numerical analysis. Experimental efforts are also important in the understanding of the damage behavior of the model systems. For the third research goal, the scratch analysis is to provide a more realistic simulation of material damage. A comprehensive material-dependent criterion will be proposed to allow the two important damage modes, *i.e.*, shear yielding and crazing/cracking, to compete against each other before ultimate failure. An appropriate damage mechanism will be put in place to transfer load-carrying capability from damaged materials to neighboring pristine areas. The fourth and final goal is to perform a more realistic and complete FEA. Here, it shall be taken that FEM remains as the analysis technique and ABAQUS[®] continues to be used for conducting the analysis. To meet this goal, a two-tier effort may be necessary. First of all, the scopes of scratch analysis should be re-examined for the analysis to include as many, if not all of essential fundamental physics involved. A new addition to

the scopes of FEA will probably be thermo-elasticity to account for heat generated and its dissipation during the scratch process. The next concurrent effort for the fourth goal is to introduce improvements to FEA, as a concerted effort to save computational resources, reduce analysis time and ultimately, perform simulations that are more comparable to actual experiments.

First Research Goal: A More Representative Material Constitutive Law

The first research goal exemplifies a key effort to bridge the gap between material science and mechanics in scratch research. To develop constitutive models for bulk amorphous polymers that can accurately represent the scratch response, a comprehensive experimental undertaking is necessary to measure material properties, which are covered in the next section under the second research goal. With the constitutive modeling efforts as presented in Chapter VI, the research accomplishments on rubber elasticity models allow an extension to amorphous polymers. Though there may be similarity in the mechanism of deformation between amorphous polymers and rubbers, the ability of undergoing plastic deformation and crazing as well as the breakage and re-establishment of tie chains at points of entanglement fundamentally set amorphous materials apart from rubbers. In particular, Boyce and her co-researchers successfully applied the non-Gaussian eight-chain rubber elasticity model [41] to the amorphous materials and captured their inherent strain-softening and strain-hardening behavior at high compressive strains [72]. But it remains to be verified if their model for amorphous materials can be applied to tensile, shear or other more complex modes of

deformation. Once the material constitutive models can be constructed successfully, they have to be implemented correctly in the analysis procedure, ABAQUS[®]. From the above, it is clear that there is much research ground to be covered to bring about modifications to rubber elasticity models before they can be applied to amorphous or semi-crystalline polymers.

Second Research Goal: Experimentation

From the perspective of materials science, the treatment of the scratch resistance of amorphous polymers entails several levels of investigative work and careful considerations. For the benefit of numerical analysis, comprehensive material characterization of model materials is required. Essential mechanical properties like elastic and shear moduli (static and dynamic), yield strength and ultimate strength are to be measured for different modes of deformation (tension/compression/biaxial), strain rates and temperatures. Experiments such as creep [73] or stress relaxation tests may also be performed to adequately characterize the viscoelastic nature of the materials. Evaluation work using optical and electron microscopes may be necessary to aid the understanding of the damage modes unique to polymers.

To compare and verify results from numerical analysis, scratch experimental data are to be collected from testing using the custom-built scratch machine, shown in Figure 43. Also will be beneficial to numerical analysis for its damage modeling effort, scratch damage mechanisms can be examined using evaluation tools like optical (OM) [74] and electron microscopes (SEM/TEM) and interferometer [75], as shown in Figure 44.

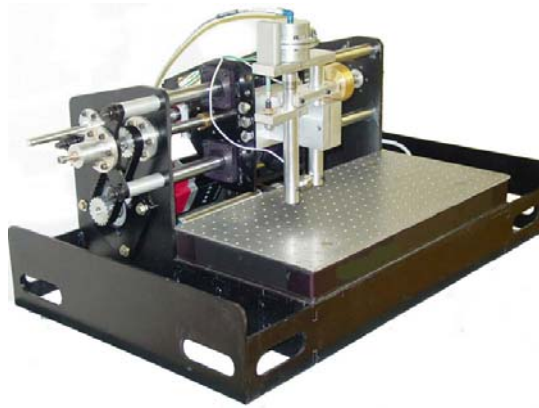


Figure 43: Scratch machine for scratch testing.

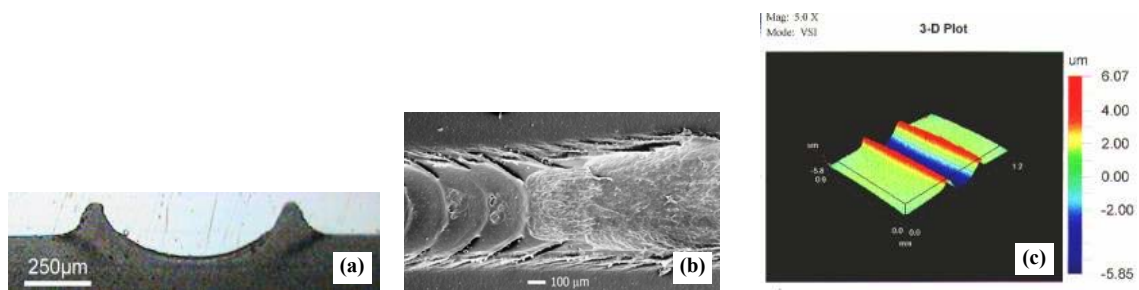


Figure 44: (a) OM image of a scratch profile [74]; (b) SEM image of scratch damage; (c) interferometer image of a scratch groove [75].

Third Research Goal: Damage Criterion

To pursue the third research goal, conscientious effort must be made to generate a criterion to differentiate the competition for the initiation of shear yielding and crazing. Also to properly characterize the extent of damage and its ultimate failure in the material, there should be a scheme to allow a gradual deterioration of load-carrying capability of the material. To propose a competing criterion for the two damage modes, it is first necessary to have the criteria for each of them. For shear yielding, one can

adopt the well-known von Mises or Tresca criteria with an appropriate hardening rule incorporated [52]. If there is a strong pressure dependency on the plastic deformation, modified von Mises or Coulomb criteria can be used [52]. To characterize crazing, Eq. (4) can continue to be employed as the initiation criterion. To be implemented as a subroutine in ABAQUS[®], the damage model can check the stress state of a material point against the damage criteria and thereon determine the mode of damage and the corresponding stress evolution for the material point. At every analysis step, the damage subroutine needs to also monitor the amount of plastic deformation or crazing to determine the amount of stiffness loss in the material. A total loss of stiffness in the material occurs when the ultimate stress state is reached. Depending on the adopted criteria, the measure of plastic deformation or crazing can be in the form of equivalent plastic strain [50] or maximum principal strain, respectively. The incorporation of a gradual and total loss of material stiffness in the analysis allows a more realistic representation of the change in stress flow at and around the affected material points.

As can be appreciated, establishing the above-mentioned damage model entails a conscientious experimental effort to adequately and correctly characterize the type and extent of material damage. In addition, it should be recognized that material damage is closely related to its constitutive relations with regards to the stiffness change and its undertaking must permit proper interaction between the two for a more complete description of material behavior and damage.

Fourth Research Goal: To Perform a More Accurate and Complete FEA

As discussed, the important feature of a realistic FEA is its inclusive scope of analysis that must encompass all of the essential physical phenomena. In the preliminary results presented earlier, the heat generation and transfer during the scratch process have been ignored for simplification. Relevant to the scratch problem, there are three different sources of heat generation. The first heat source comes from the energy release due to inelastic and plastic straining; a good illustrative example of energy release is the presence of hysteresis due to plastic loading and elastic recovery of structures. The next heat source is the frictional heat generated at the interface between contacts in the scratch problem. Ambient temperature change in the environment is another source of heat energy for the system. The presence of heat in a mechanical process can affect its analysis in two ways: one is to contribute to a dimensional change, *i.e.*, expansion or contraction while the other is a change in the material response where a material takes on a different constitutive response at various temperature levels. Of the two, the change in material rheology with temperature has a greater consequence on the mechanical response of polymers than the dimensional change. Temperature dependency can also be applied to material damage, as mentioned in [76] particularly for crazing and yielding. This again emphasizes the importance of experimental work to characterize material behavior at different temperatures for developing an appropriate temperature-dependent material law. Also appropriate for polymers, visco-elasticity and visco-plasticity should be featured in the analysis accordingly.

Now focusing on the improvements for the accuracy of FEA, it has been discussed in Chapter III that the computational resources and time required for the analysis are quite demanding; a full analysis requires four to five days of computational time and approximately three gigabytes of memory. These computational requirements limit the ability to perform FEA that are comparable to the experimental setup and thereby restricting the comparison of results to only qualitative in nature. A way to overcome this difficulty is to have a more efficient mesh design for the analysis domain where larger elements can be used in regions with low strain gradients. Another approach is to scrutinize the scratch problem further for more simplifications, such as applying non-linear elasticity only to areas with large deformation. Another method is to adopt a global-local analysis approach, in which a coarser analysis domain is first used to elicit the global response. Results of the global model are then superimposed onto a finer but smaller domain of interest to determine its local behavior. Depending on the scopes of analysis, micromechanics modeling may be required for the local analysis [77]. Using this strategy, analysis can be performed more efficiently and a good understanding of the overall global and local responses of the problem can still be gained.

If the proposed goals of this research endeavor can be accomplished with reasonable success, the collective impact on the academic and industrial worlds may be significant. The end product of this research effort will be a comprehensive and versatile analysis tool that allows researchers to not only study scratch behavior of polymers but also different types of deformation (*e.g.*, impact) and various applications (*e.g.*, micro-mechanical machines).

REFERENCES

- [1] ASTM International, "ASTM G 171-03: Standard test method for scratch hardness of materials Using a Diamond Stylus," *Annual Book of ASTM Standards*, 3-02, 2003.
- [2] International Organization for Standardization, "ISO 12137-1:1997 – Determination of mar resistance – Part 1: Method using a curved stylus," *ISO Standards*, 87.040, 1997.
- [3] International Organization for Standardization, "ISO 12137-2:1997 – Determination of mar resistance – Part 2: Method using a pointed stylus," *ISO Standards*, 87.040, 1997.
- [4] Lim, G.T., Wong, M., Reddy, J.N., and Sue, H.-J., "An integrated approach towards the study of scratch damage of polymer," *J. Coating Technol. Res.*, 2(5), 361-369 (2005).
- [5] Bowden, F.P. and Tabor, D. *The Friction and Lubrication of Solids*, Clarendon Press, Oxford, 1954.
- [6] Arruda, E.M., Azhi, S., Li, Y., and Ganesan, A., "Rate dependent deformation of semi-crystalline polypropylene near room temperature," *J. Eng. Mater. Technol.*, 119, 216-222 (1997).
- [7] Davis, J.L., *Finite Difference Methods in Dynamics of Continuous Media*, Macmillan, London, 1986.

- [8] Reddy, J.N., *An Introduction to the Finite Element Method*, 2nd Ed., McGraw-Hill, New York, 1993.
- [9] Johnson, K.L., *Contact Mechanics*, Cambridge University Press, Cambridge, 1985.
- [10] Mindlin, R.D., "Compliance of elastic bodies in contact," *J. Appl. Mech.*, 16, 259-268 (1949).
- [11] Mindlin, R.D. and Deresiewicz, H.J., "Elastic spheres in contact under varying oblique forces," *Appl. Mech.*, 20, 327-344 (1953).
- [12] Hamilton, G.M. and Goodman, L.E., "Stress field created by a circular sliding contact," *J. Appl. Mech.*, 33(2), 371-376 (1966).
- [13] Hamilton, G.M., "Explicit equations for the stresses beneath a sliding spherical contact," *P. I. Mech. Eng. C – J. Mech.*, 197, 53-59 (1983) [Errata, 197, 282].
- [14] Chen, W.T., "Stresses in some anisotropic materials due to indentation and sliding," *Int. J. Solids Struct.*, 5, 191-214 (1969).
- [15] Dahan, M. and Zarka, J., "Elastic contact between a sphere and a semi-infinite transversely isotropic body," *Int. J. Solids Struct.*, 13(3), 229-238 (1977).
- [16] Fabrikant, V.I., "Elastic field around a circular punch," *J. Appl. Mech.*, 55(3), 604-610 (1988).
- [17] Lin, W., Kuo, C.H., and Keer, L.M., "Analysis of a transversely isotropic half space under normal and tangential loadings," *J. Tribol.*, 113(2), 335-338 (1991).
- [18] Hanson, M.T., "The elastic field for conical indentation including sliding friction for transverse isotropy," *J. Appl. Mech.*, 59(2), S123-S130 (1992).

- [19] Hanson, M.T., "The elastic field for spherical Hertzian contact including sliding friction for transverse isotropy," *J. Tribol.*, 114(3), 606-611 (1992).
- [20] Hanson, M.T. and Puja, I.W., "The elastic field resulting from elliptical Hertzian contact of transversely isotropic bodies: Closed-form solutions for normal and shear loading," *J. Appl. Mech.*, 64(3), 457-465 (1997).
- [21] Churilov, V.A., "Effect of a normal load moving at a constant velocity along boundary of an elastic half-space," *J. Appl. Math. Mech.*, 41(1), 125-132 (1977).
- [22] Churilov, V.A., "Action of an elliptic stamp moving at a constant speed on an elastic half-space," *J. Appl. Math. Mech.*, 42(6), 1176-1182 (1978).
- [23] Rahman, M., "Hertz problem for a rigid punch moving across the surface of a semi-infinite elastic solid," *Z. Angew. Math. Phys.*, 47(4), 601-615 (1996).
- [24] Brock, L.M., "Exact analysis of dynamic sliding indentation at any constant speed on an orthotropic or transversely isotropic half-space," *J. Appl. Mech.*, 69(3), 340-345 (2002).
- [25] Lee, E.H. and Radok, J.R.M., "The contact problem for viscoelastic bodies," *J. Appl. Mech.*, 27, 438-444 (1960).
- [26] Hunter, S.C., "The Hertz problem for a rigid spherical indenter and a viscoelastic half-space," *J. Mech. Phys. Solids*, 8, 219-234 (1960).
- [27] Mackerle, J., "Finite element and boundary element simulations of indentation problems - A bibliography (1997-2000)," *Finite Elem. Anal. Des.*, 37(10), 811-819 (2001).

- [28] Tian, H. and Saka, N., "Finite-element analysis of an elastic-plastic 2-layer half-space - sliding contact," *Wear*, 148(2), 261-285 (1991).
- [29] Lee, J.H., Xu, G.H., and Liang, H., "Experimental and numerical analysis of friction and wear behavior of polycarbonate," *Wear*, 251(2), 1541-1556 (2001).
- [30] Wong, M., Lim, G.T., Rood, P.R., Moyse, A., Reddy, J.N. and Sue, H.-J., "Scratch damage phenomena of polyolefin materials," *TPOs in Automotive Conference* (2003).
- [31] Bucaille, J.L., Felder, E., and Hochstetter, G., "Mechanical analysis of the scratch test on elastic and perfectly plastic materials with the three-dimensional finite element modeling," *Wear*, 249(5-6), 422-432 (2001).
- [32] Subhash, G. and Zhang, W., "Investigation of the overall friction coefficient in single-pass scratch test," *Wear*, 252(1-2), 123-134 (2002).
- [33] Maier, C.; Calafut, T. *Polypropylene: The Definitive User's Guide and Databook*; PDL Handbook Series, Plastics Design Library, New York, 1998.
- [34] Wu, P.D. and van der Giessen, E., "On improved 3-D non-Gaussian network models for rubber elasticity and their application to orientation hardening in glassy polymers," *J. Mech. Phys. Solids*, 41(3), 427-456 (1993).
- [35] Kreyszig, E. *Advanced Engineering Mathematics*, 7th Ed. John Wiley & Sons, Inc., Singapore, 1184-1189, 1993.
- [36] Treloar, L.R.G., *The Physics of Rubber Elasticity*, 3rd Ed. Clarendon Press, Oxford, 1975.

- [37] Treloar, L.R.G., "Stress-strain data for vulcanized rubber under various types of deformation," *Trans. Faraday Soc.*, 40, 59-70 (1944).
- [38] Boyce, M.C. and Arruda, E.M., "Constitutive models of rubber elasticity: A review," *Rubber Chem. Technol.*, 73(3), 504-523 (2001).
- [39] James, H.M. and Guth, E., "Theory of the elastic properties of rubber," *J. Chem. Phys.*, 10, 455-481 (1943).
- [40] Flory, P.J. and Rehner, J., "Statistical mechanics of cross-linked polymer networks: I. Rubber elasticity," *J. Chem. Phys.*, 11, 512-520 (1943).
- [41] Arruda, E.M. and Boyce, M.C., "A three-dimensional constitutive model for the large stretch behavior of rubber elastic materials," *J. Mech. Phys. Solids*, 41(2), 389-412 (1993).
- [42] Beatty, M.F., "An average-stretch full-network model for rubber elasticity," *J. Elasticity*, 70, 65-86 (2003).
- [43] Bischoff, J.E., Arruda, E.M. and Grosh, K., "A new constitutive model for the compressibility of elastomers at finite deformations," *Rubber Chem. Technol.*, 74(4), 541-559 (2001).
- [44] Kaliske, M., and Rothert, H., "On the finite element implementation of rubber-like materials at finite strains," *Eng. Computation.*, 14(2), 216-232 (1997).
- [45] Williams, J.A., "Analytical models of scratch hardness," *Tribol. Intern.*, 29(8), 675-694 (1996).
- [46] ABAQUS[®], Inc., *ABAQUS[®] Analysis User's Manual Ver. 6.4*, Pawtucket, Rhode Island, 2003.

- [47] ABAQUS[®], Inc., *ABAQUS[®] Theory Manual Ver. 6.4*, Pawtucket, Rhode Island, 2003.
- [48] ABAQUS[®], Inc., *ABAQUS[®]/Example Problems Manual Ver. 6.4*, Pawtucket, Rhode Island, 2003.
- [49] Wong, M., Moyse, A., Lee, F. and Sue, H.-J., “Study of surface damage in polypropylene under progressive loading,” *J. Mater. Sci.*, 39, 3293-3308 (2004).
- [50] Wong, M., Lim, G.T., Moyse, A., Reddy, J.N. and Sue, H.-J., “A new test methodology for evaluating scratch resistance of polymers,” *Wear*, 256(11-12), 1214-1227 (2004).
- [51] Flanagan, D. P., and T. Belytschko, “A uniform strain hexahedron and quadrilateral with orthogonal hourglass control,” *Int. J. Numer. Meth. Eng.*, 17, 679–706 (1981).
- [52] Khan, A.S. and Huang, S., *Continuum Theory of Plasticity*, John Wiley & Sons, New York, 1995.
- [53] Kinloch, A.J. and Young, R.J., *Fracture Behavior of Polymers*, Elsevier Science Pub. Co.: New York, 1983.
- [54] Bowden, P.B. and Oxborough, R.J., “A general critical strain criterion for crazing in amorphous glassy polymers,” *Philos. Mag.*, 28, 547-559 (1973).
- [55] Argon, A.S. and Salama, M.M.. “Growth of crazes in glassy polymers,” *Philos. Mag.*, 36(5), 1217-1234 (1977).
- [56] Xiang, C., Sue, H.-J., Chu, J., and Coleman, B., “Scratch behavior and material property relationship in polymers,” *J. Polym. Sci. Polym. Phys. Ed.*, 39, 47-59 (2001).

- [57] Blees, M.H., Winkelman, G.B., Balkenende, A.R., and den Toonder, J.M.J., "The effect of friction on scratch adhesion testing: application to a sol-gel coating on polypropylene," *Thin Solid Films*, 359, 1-13 (2000).
- [58] Ducret, S., Pailler-Mattei, C., Jardret, V., Vargiolu, R., and Zahouani, H., "Friction characterisation of polymers abrasion (UHMWPE) during scratch tests: single and multi-asperity contact," *Wear*, 255(2), 1093-1100 (2003).
- [59] Tabor, D. "The physical meaning of indentation and scratch hardness," *Brit. J. Appl. Phys.*, 7, 159-166 (1956).
- [60] Briscoe, B.J., Delfino, A., and Pelillo, E., "Single-pass pendulum scratching of poly(styrene) and poly(methylmethacrylate)," *Wear*, 225-229(1), 319-328 (1999).
- [61] Vingsbo, O. and Hogmark, S., "Single-pass pendulum grooving- a technique for abrasive testing," *Wear*, 100, 489-502 (1984).
- [62] Liang, Y.N., Li, S.Z., Li, D.F., and Li, S., "Some developments for single-pass pendulum scratching," *Wear*, 199, 66-73 (1996).
- [63] Kody, R.S. and Martin, D.C., "Quantitative characterization of surface deformation in polymer composites using digital image analysis," *Polym. Eng. Sci.*, 36(2), 298-304 (1996).
- [64] Chu, J., Xiang, C., Sue, H.-J. and Hollis, R., "Scratch resistance of mineral-filled polypropylene materials," *Polym. Eng. Sci.*, 40, 944-955(2000).
- [65] Malvern, L.E., *Introduction to the Mechanics of a Continuous Medium*, Prentice-Hall, Inc., Englewood Cliff, New Jersey, 1969.

- [66] Horgan, C.O., and Saccomandi, G., “A molecular-statistical basis for the Gent constitutive model of rubber elasticity,” *J. Elasticity*, 68, 167-176 (2002).
- [67] Treloar, L.R.G., “The photoelastic properties of short-chain molecular networks,” *T. Faraday Soc.*, 50, 881-896 (1954).
- [68] Cohen, A., “A Padè approximant to the inverse Langevin function,” *Rheol. Acta.*, 30, 270-273 (1991).
- [69] Anand, L., “A constitutive model for compressible elastomeric solids,” *Comput. Mech.*, 18, 339-355 (1996).
- [70] Spencer, A.J.M., *Continuum Mechanics*, Longman, London, 1980.
- [71] Atkin, R.J., *An Introduction to the Theory of Elasticity*, Longman, London, 1980.
- [72] Boyce, M.C., Parks, D.M., and Argon, A.S., “Large inelastic deformation of glassy polymers. Part I: Rate dependent constitutive model,” *Mech. Mater.*, 7, 15-33 (1988).
- [73] Feng, C.-W., Keong, C.-W., Hsueh, Y.-P., Wang, Y.-Y., and Sue, H.-J., “Prediction of long-term creep behavior of epoxy adhesive for aluminum substrates,” Annual Technical Conference (ANTEC) 2004, 2860-2863.
- [74] Wong, M.-H., “The development of scratch test methodology and characterization of surface damage of polypropylene,” M.S. Thesis, Texas A&M University (2003).
- [75] Xiang, C., “Scratch behaviors in polymers,” Ph.D. Dissertation, Texas A&M University (2000).

- [76] Yamamoto, T. and Furukawa, H., "Relationship between molecular structure and deformation – fracture mechanism of amorphous polymers: 2. Crazing stress," *Polymer*, 36(12), 2393-2396 (1995).
- [77] Tang, X., Whitcomb, J.D., Li, Y., and Sue, H.-J., "Micromechanics modeling of moisture diffusion in woven composites," *Compos. Sci. Technol.*, 65, 817-826 (2005).

APPENDIX A

APPENDIX A-1

This appendix contains the ABAQUS[®] input file for the static analysis of the scratch problem.

```
*HEADING
  3D SCRATCH ANALYSIS OF POLYPROPYLENE WITH 1 SPHERICAL INDENTER
** =====
** REWRITE DEFINITION
** =====
*RESTART,WRITE,FREQUENCY=5
**
** =====
** NODAL DEFINITION
** =====
*NODE,NSET=TIP
  2000000, 0.005, 0.010, 0.0043303571429
**
** =====
** ELEMENT DEFINITION
** =====
*ELEMENT,TYPE=MASS,ELSET=PMASS
  2000000,2000000
*MASS,ELSET=PMASS
  5.E-06,
*INCLUDE,INPUT=mesh.inp
** (mesh.inp is the mesh file generated using the mesh generator -
** see Appendix A-3)
**
** =====
** CONTACT BODY DEFINITION
** =====
*SURFACE,TYPE=REVOLUTION,NAME=PUNCH
  0.005, 0.010, 0.0035, 0.005, 0.010, 0.0055
  START,0.0005,0.002
  LINE, 0.0005,0.
  CIRCL,0.,-0.0005,0.,0.
*RIGID BODY,REF NODE=TIP, ANALYTICAL SURFACE=PUNCH
**
** =====
** MATERIAL DEFINITION
** =====
*MATERIAL,NAME=PP
*ELASTIC
```

```

1.65E09,0.4
*PLASTIC,HARDENING=ISOTROPIC
34.3478E06, 0.0
36.9565E06, 0.109362
36.7391E06, 0.177734
35.4348E06, 0.278524
34.4348E06, 0.379130
33.9130E06, 0.479447
33.4783E06, 0.579710
33.2609E06, 0.679842
33.3696E06, 0.779776
33.6957E06, 0.879578
34.3478E06, 0.979183
35.4348E06, 1.078524
36.5217E06, 1.177866
38.1739E06, 1.276864
40.0000E06, 1.375758
41.3043E06, 1.474967
42.6087E06, 1.574177
44.0000E06, 1.673333
45.4348E06, 1.772464
46.7391E06, 1.871673
48.0435E06, 1.936583
*PLASTIC,HARDENING=ISOTROPIC,RATE=0.1
44.3478E06, 0.
43.9130E06, 0.173386
39.3478E06, 0.376153
36.0870E06, 0.578129
34.3478E06, 0.679183
33.3696E06, 0.779776
32.6087E06, 0.880237
32.6087E06, 0.980237
33.0435E06, 1.079974
33.6522E06, 1.179605
36.0870E06, 1.378129
39.1304E06, 1.576285
41.5217E06, 1.774835
42.3913E06, 1.874308
*PLASTIC,HARDENING=ISOTROPIC,RATE=1.0
52.6956E06, 0.
51.5652E06, 0.168748
45.2174E06, 0.372596
39.7826E06, 0.575889
37.3043E06, 0.671491
35.4348E06, 0.778524
33.9130E06, 0.879447
33.6087E06, 0.979631
33.5652E06, 1.079657
34.1304E06, 1.179315
34.7826E06, 1.278920
35.6522E06, 1.378393
36.5217E06, 1.477866
37.6087E06, 1.577207

```

```

38.6957E06, 1.676548
39.7826E06, 1.775889
40.8696E06, 1.875231
*DENSITY
  905,
**
** =====
** CONTACT DEFINITION
** =====
*CONTACT PAIR, INTERACTION=IMP_TARG
  TARGET, PUNCH
*SURFACE INTERACTION, NAME=IMP_TARG
*FRICTION
  0.3,
**
** =====
** STEP 1 DEFINITION
** (Move down the mass element)
** =====
*STEP, NLGEOM=YES, INC=200, NAME=INDENTATION
*STATIC
  ,1.0
*BOUNDARY
  BOT, 3,3,
  ENDS, 1,3,
  SIDE, 1,1,
  TIP, 1,2,
  TIP, 4,6,
  TIP, 3,3,-1.243206E-04
*OUTPUT, FIELD, VARIABLE=PRESELECT
*OUTPUT, HISTORY, VARIABLE=PRESELECT
*END STEP
**
** =====
** STEP 2 DEFINITION
** (Replace the displacement BC with the normal load BC)
** =====
*STEP, NLGEOM=YES, INC=200, NAME=LOAD_REPLACEMENT
*STATIC
  ,1.0
*BOUNDARY
  BOT, 3,3,
  ENDS, 1,3,
  SIDE, 1,1,
  TIP, 1,2,
  TIP, 4,6,
*CLOAD
  TIP, 3,-5
*END STEP
**

```

APPENDIX A-2

This appendix contains the ABAQUS® input file for the dynamic analysis of the scratch problem.

```

*HEADING
  3D SCRATCH ANALYSIS OF PP WITH SPHERICAL INDENTER
**
** =====
**  IMPORT  DEFINITION
** =====
*IMPORT,STEP=2,STATE=YES,UPDATE=NO
  Substrate
*IMPORT NSET
  ENDS, BOT, SIDE, TOP, BODY, NALL
*IMPORT ELSET
  BOT, BODY, Substrate, ADA_REMESH, TARGET_S2
**
** =====
**  NODAL DEFINITION
** =====
*NODE, NSET=TIP
2000000, 0.005, 0.010, 0.0042889169429
**
** =====
**  ELEMENT DEFINITION
** =====
*ELEMENT,TYPE=MASS,ELSET=PMASS
2000000,2000000
*MASS,ELSET=PMASS
5.E-06,
**
** =====
**  CONTACT BODY DEFINITION
** =====
*SURFACE,TYPE=ELEMENT,NAME=TARGET
  TARGET_S2, S2
*SURFACE,TYPE=REVOLUTION,NAME=PUNCH
0.005, 0.010, 0.0034585598, 0.005, 0.010, 0.0054585598
START,0.0005,0.002
LINE, 0.0005,0.
CIRCL,0.,-0.0005,0.,0.
*RIGID BODY,REF NODE=TIP, ANALYTICAL SURFACE=PUNCH
**
** =====
**  AMPLITUDE CURVE DEFINITION
** =====
*AMPLITUDE,NAME=S_RATE,TIME=STEP TIME

```

```

0.,0.,0.75E-03,0.25,1.5E-03,0.5,2.25E-03,0.75,
3.E-03,1.0
*AMPLITUDE,NAME=L_RATE,TIME=STEP TIME
0.,0.333333,0.75E-03,0.5,1.5E-03,0.666666,2.25E-03,0.833333,
3.E-03,1.0
*AMPLITUDE,NAME=B_RATE,TIME=STEP TIME
0.,0.,0.25E-04,0.25,0.5E-04,0.5,0.75E-04,0.75,
1.E-04,1.0
**
** =====
** STEP 3 DEFINITION
** (Move the mass element laterally)
** =====
*STEP,NAME=SCRATCH
*DYNAMIC, EXPLICIT
,3.E-03
*BOUNDARY,OP=NEW
  BOT, 3,3,
  ENDS, 1,3,
  SIDE, 1,1,
  TIP, 1,1,
  TIP, 4,6,
*CLOAD,AMPLITUDE=L_RATE,OP=NEW
  TIP,3,-15
*BOUNDARY,AMPLITUDE=S_RATE,OP=NEW
  TIP,2,2,0.03
*CONTACT PAIR,INTERACTION=IMP_TARG
  TARGET,PUNCH
*SURFACE INTERACTION,NAME=IMP_TARG
*FRICTION
  0.3,
*ADAPTIVE MESH, ELSET=ADA_REMESH, MESH SWEEPS=25
*OUTPUT, FIELD, NUMBER INTERVAL=50, VARIABLE=PRESELECT
*OUTPUT, HISTORY, VARIABLE=PRESELECT
*RESTART,WRITE,NUMBER INTERVAL=5,TIMEMARKS=YES
*END STEP
**

```

APPENDIX A-3

This appendix contains the program written in Fortran language to generate finite element mesh shown in Figure 6 for ABAQUS®.

```

C      Program MESH
C      *****
C      This program is to create mesh for ABAQUS
C      *****
C
      USE DFPORT
      IMPLICIT REAL*8(A-H,O-Z)
      DIMENSION X(9000000),Y(9000000),Z(9000000),AM(100000)
      DIMENSION NOD(16)
      CHARACTER*20 ITFILE, IHFILE, RECT
      CHARACTER*100 INFILE
      DATA TOL1/1.D-30/, TOL2/1.D-06/

      IT=6
      IH=7
C
C      This section is only applicable for inputs from file
C
      IN=6
      OPEN (IN, file="meshinfo.txt",Status='Unknown')
      REWIND (IN)
      READ(IN,*) NELEM, NLAYER, NUNIFO, IABAQUS
      CLOSE (IN)
C
C      File Management
      WRITE(ITFILE,'(I5)') NELEM
      L=6
      DO I=1,5
         IF(ITFILE(I:I).NE.''.AND. I.LT.L) L=I
      ENDDO
      ITFILE='section_'//ITFILE(L:LEN_TRIM(ITFILE))
      IHFILE=ITFILE(1:LEN_TRIM(ITFILE))//'.out'
      ITFILE=ITFILE(1:LEN_TRIM(ITFILE))//'.inp'

      OPEN (IT, file=ITFILE,Status='Unknown')
      OPEN (IH, file=IHFILE,Status='Unknown')
      REWIND (IT)
      REWIND (IH)
C
C      Mesh Initialization Parameter
      XMAX=5.D-03
      YMAX=5.D-02
      ZMAX=3.D-03

```

```

YPATH=3.6D-02
ZTHICK=ZMAX/DBLE(NLAYER)
IF(NUNIFO.EQ.1) ELEN = YMAX/DBLE(NELEM)
IF(NUNIFO.EQ.2) THEN
    ELEN = YPATH/DBLE(NELEM)
    YSTART=0.5D0*(YMAX-YPATH)-((INT(3.D-03/ELEN)+1)*ELEN-3.D-03)
    YEND=YSTART+YPATH
ENDIF

```

```

C      Node Generation
      Print*, 'Starting...Nodal Generation'

      TSTART=TIMEF( )
      INODE=1
      NFLAG1=0
      NFLAG2=0
      TEMPY=0.D0
      TEMPX=1.D-16
      NXOVER=0
      NXSEG=-1
      DO WHILE (ABS(TEMPX-XMAX) .GT. ABS(TEMPX+XMAX)*TOL1 .AND.
+          NXOVER.EQ.0)
          NYOVER=0
          TEMPX=TEMPX-1.D-16
          IF(NFLAG1.LE.2 .AND. NUNIFO .EQ. 2) THEN
              IF(NFLAG1.EQ.2) NFLAG2=0
              DO WHILE(ABS(YMAX-TEMPY) .GT. ABS(YMAX+TEMPY)*TOL1 .AND.
+                  NYOVER.EQ.0)
                  X(INODE)=TEMPX
                  Y(INODE)=TEMPY
                  INODE=INODE+1
                  IF(TEMPY.LT.YSTART .AND.
+                      ABS(TEMPY-YSTART) .GT. ABS(TEMPY+YSTART)*TOL2) THEN
                      TEMPY=TEMPY+YSTART/7.D0
                  ELSEIF(TEMPY.GT.YEND .OR.
+                      ABS(TEMPY-YEND) .LT. ABS(TEMPY+YEND)*TOL2) THEN
                      TEMPY=TEMPY+(YMAX-YEND)/7.D0
                  ELSE
                      IF(NFLAG1.EQ.2) NFLAG2=NFLAG2+1
                      IF(NFLAG1.LE.1) TEMPY=TEMPY+ELEN
                      IF(NFLAG1.EQ.2) TEMPY=TEMPY+DBLE(NFLAG2)*ELEN
                      IF(NFLAG1.EQ.2 .AND. NFLAG2.EQ.3) THEN
                          TEMPY=TEMPY-2.D0*ELEN
                          NFLAG2=0
                      ENDIF
                  ENDIF
                  IF(TEMPY-YMAX.GT.(TEMPY+YMAX)*TOL2) NYOVER=1
              ENDDO
              NFLAG1=NFLAG1+1
              ELSEIF(NFLAG1.EQ.3 .AND. NUNIFO .EQ. 2) THEN
                  DO WHILE(ABS(YMAX-TEMPY) .GT. ABS(YMAX+TEMPY)*TOL1 .AND.
+                      NYOVER.EQ.0)
                      X(INODE)=TEMPX

```



```

        Y(INODE)=TEMPY
        INODE=INODE+1
        IF(TEMPY.LT.YSTART .AND.
+          ABS(TEMPY-YSTART).GT.ABS(TEMPY+YSTART)*TOL2) THEN
            TEMPY=TEMPY+YSTART/7.D0
        ELSEIF(TEMPY.GT.YEND .OR.
+          ABS(TEMPY-YEND).LT.ABS(TEMPY+YEND)*TOL2) THEN
            TEMPY=TEMPY+(YMAX-YEND)/7.D0
        ELSE
            TEMPY=TEMPY+2.D0*ELEN
        ENDIF
        IF(TEMPY-YMAX.GT.(TEMPY+YMAX)*TOL2) NYOVER=1
    ENDDO
    ELEN=2.D0*ELEN
    NFLAG1=1
    ELSEIF(NUNIFO.EQ.1) THEN
        DO WHILE(ABS(YMAX-TEMPY).GT.ABS(YMAX+TEMPY)*TOL1 .AND.
+          NYOVER.EQ.0)
            X(INODE)=TEMPX
            Y(INODE)=TEMPY
            INODE=INODE+1
            TEMPY=TEMPY+ELEN
            IF(TEMPY-YMAX.GT.(TEMPY+YMAX)*TOL2) NYOVER=1
        ENDDO
    ENDIF
    TEMPY=0.D0
    TEMPX=TEMPX+ELEN+1.D-16
    IF(TEMPX-XMAX.GT.(TEMPX+XMAX)*TOL2) NXOVER=1
    IF((TEMPX+ELEN)-XMAX.GT.((TEMPX+ELEN)+XMAX)*TOL2 .AND.
+    NFLAG1.EQ.2) NXOVER=1
    NXSEG=NXSEG+1
    ENDDO
    INODE=INODE-1
    TEMPX=TEMPX-ELEN-1.D-16
    IF(NUNIFO.EQ.1) ELEN = YMAX/DBLE(NELEM)
    IF(NUNIFO.EQ.2) ELEN = YPATH/DBLE(NELEM)
    IF(XMAX-TEMPX.GT.1.D-08) THEN
        NREPEAT=INT((XMAX-TEMPX)/ELEN)+1
        XREPEAT=(XMAX-TEMPX)/DBLE(NREPEAT)
        NXSEG=NXSEG+NREPEAT
    ENDIF

    IF(NUNIFO.EQ.1) KK=NREPEAT*(NELEM+1)
    IF(NUNIFO.EQ.2) KK=NREPEAT*(NELEM+15)
    DO I=INODE,1,-1
        X(KK+I)=X(I)+NREPEAT*XREPEAT
        Y(KK+I)=Y(I)
    ENDDO

    II=1
    DO I=1,NREPEAT
        TEMPX=DBLE(I-1)*XREPEAT
        IF(NUNIFO.EQ.1) THEN

```

```

        DO J=1,NELEM+1
            X(II)=TEMPX
            Y(II)=DBLE(J-1)*ELEN
            II=II+1
        ENDDO
        ELSEIF(NUNIFO.EQ.2) THEN
            YY=-(YSTART/7.D0)
            DO J=1,NELEM+15
                IF(J.LE.8) THEN
                    YY=YY+YSTART/7.D0
                ELSEIF(J.GT.NELEM+8) THEN
                    YY=YY+(YMAX-YEND)/7.D0
                ELSE
                    YY=YY+ELEN
                ENDIF
                X(II)=TEMPX
                Y(II)=YY
                II=II+1
            ENDDO
        ENDIF
        ENDDO
        II=II-1
        INODE=INODE+II
1  WRITE(IT,11)
    DO I=1,INODE
        X(I)=XMAX-X(I)
        IF(X(I).LT.1.D-16) X(I)=0.D0
        WRITE(IT,12) I, X(I),Y(I),Z(I)
    ENDDO

    DO I=1,NLAYER
        DO J=I*INODE+1, (I+1)*INODE
            X(J)=X(J-INODE)
            Y(J)=Y(J-INODE)
            Z(J)=DBLE(I)*ZTHICK
        ENDDO
    ENDDO

    WRITE(IT,16) NLAYER*INODE,ZMAX
    WRITE(IT,18) NLAYER,INODE
    WRITE(IT,20)

    TEND=TIMEF()
    WRITE(RECT,'(E10.3)') TEND-TSTART
    Print*, 'Completed..Nodal Generation (Clock Time = ',
+RECT(1:10),' sec)'

    WRITE(IH,*) 'Completed..Nodal Generation (Clock Time = ',
+RECT(1:10),' sec)'
C  Nodal Boundary Condition Imposition
    Print*, 'Starting...Nodal Boundary Process'

```

```

TSTART=TIMEF( )
WRITE(IT,21)
II=0
DO I=1,(N_LAYER+1)*INODE
  IF (ABS(X(I)-XMAX) .LE. ABS(X(I)+XMAX)*TOL2) THEN
    II=II+1
    NOD(II)=I
    IF(II.EQ.16) THEN
      WRITE(IT,22) (NOD(J), J=1,16)
      II=0
    ENDIF
  ENDIF
  IF(I.EQ.(N_LAYER+1)*INODE .AND. II.LT. 16) THEN
    WRITE(IT,22) (NOD(J), J=1,II)
  ENDIF
ENDDO

WRITE(IT,23)
II=0
DO I=1,(N_LAYER+1)*INODE
  IF (Y(I) .LE. Y(I)*TOL2) THEN
    II=II+1
    NOD(II)=I
    IF(II.EQ.16) THEN
      WRITE(IT,22) (NOD(J), J=1,16)
      II=0
    ENDIF
  ENDIF
  IF(I.EQ.(N_LAYER+1)*INODE .AND. II.LT. 16) THEN
    WRITE(IT,22) (NOD(J), J=1,II)
  ENDIF
ENDDO

WRITE(IT,24)
II=0
DO I=1,(N_LAYER+1)*INODE
  IF (ABS(Y(I)-YMAX) .LE. ABS(Y(I)+YMAX)*TOL2) THEN
    II=II+1
    NOD(II)=I
    IF(II.EQ.16) THEN
      WRITE(IT,22) (NOD(J), J=1,16)
      II=0
    ENDIF
  ENDIF
  IF(I.EQ.(N_LAYER+1)*INODE .AND. II.LT. 16) THEN
    WRITE(IT,22) (NOD(J), J=1,II)
  ENDIF
ENDDO

WRITE(IT,25)

TEND=TIMEF( )

```

```

WRITE(RECT,'(E10.3)') TEND-TSTART
Print*, 'Completed..Nodal Boundary Imposition (Clock Time
+ = ',RECT(1:10),' sec)'

WRITE(IH,*)'Completed..Nodal Boundary Imposition (Clock Time
+ = ',RECT(1:10),' sec)'

C   Element Connectivity
Print*, 'Starting...Mesh Generation'

TSTART=TIMEF()
WRITE(IT,30)
NJUMP=0
TEMPX=XMAX
TEMPY=0.D0
IELEM=1
IADAPT=1
NOD(1)=1
DO WHILE (TEMPX .GT. TEMPX*TOL2)
  NYOVER=0
  DO WHILE (ABS(YMAX-TEMPY) .GT. ABS(YMAX+TEMPY)*TOL2 .AND.
+      NYOVER.EQ.0)
    DO I=NOD(1),INODE
      IF(ABS(X(I)-TEMPX).LE.ABS(X(I)+TEMPX)*TOL2 .AND.
+      ABS(Y(I)-TEMPY).LE.ABS(Y(I)+TEMPY)*TOL2) NOD(1)=I
    ENDDO
    NOD(2)=NOD(1)+1
    IERR=1
    YY=0.D0
2    I=NOD(2)+1
    NOD(3)=0
    DO WHILE (I.LE.INODE)
      Y1=ABS(Y(I)-Y(NOD(2))-YY)
      Y2=ABS(Y(I)+Y(NOD(2))+YY)
      IF(Y1 .LE. Y2*TOL2 .AND. X(I).LT.X(NOD(2))) THEN
        NOD(3)=I
        I=INODE
      ENDIF
      I=I+1
    ENDDO
    IF(NOD(3).EQ.0) THEN
      YY=Y(NOD(2))-Y(NOD(1))
      NJUMP=1
      GOTO 2
    ENDIF

3    YY=0.D0
    I=NOD(2)
    NOD(4)=0
    DO WHILE (I.LE.INODE)
      Y1=ABS(Y(I)-Y(NOD(1))+YY)
      Y2=ABS(Y(I)+Y(NOD(1))-YY)
      IF(Y1 .LE. Y2*TOL2 .AND. X(I).LT.X(NOD(1))) THEN

```

```

        NOD(4)=I
        I=INODE
    ENDIF
    I=I+1
ENDDO
IF(NOD(4).EQ.0) THEN
    YY=Y(NOD(2))-Y(NOD(1))
    GOTO 3
ENDIF

DO I=5,8
    NOD(I)=NOD(I-4)+INODE
ENDDO
WRITE(IT,40) IELEM, (NOD(I),I=1,8)
IF(Y(NOD(2)).GE.0.7D-02 .AND. Y(NOD(2)).LE.4.3D-02) THEN
    IF(X(NOD(3)).GE.3.D-03) THEN
        AM(IADAPT)=IELEM
        IADAPT=IADAPT+1
    ENDIF
ENDIF
IF(IEERR.EQ.3) WRITE(IT,50) IELEM
TEMPY=Y(NOD(2))
IF(NJUMP.EQ.1) THEN
    TEMPY=Y(NOD(2)+1)
    NJUMP=0
ENDIF
IELEM=IELEM+1
IF(TEMPY-YMAX.GT.(TEMPY+YMAX)*TOL2) NYOVER=1
ENDDO
TEMPY=0.D0
TEMPX=X(NOD(3))
ENDDO
IELEM=IELEM-1
IADAPT=IADAPT-1
DO I=2, NLAYER
    WRITE(IT,52) (I-1)*IELEM,(I-1)*INODE
ENDDO
WRITE(IT,54)
WRITE(IT,60)
IF(IABAQUS.EQ.2) WRITE(IT,65)

TEND=TIMEF()
WRITE(RECT,'(E10.3)') TEND-TSTART
Print*, 'Completed..Mesh Generation (Clock Time =',
+RECT(1:10),' sec)'

WRITE(IH,*)'Completed..Mesh Generation (Clock Time =',
+RECT(1:10),' sec)'

C    Element Connectivity
Print*, 'Starting...Element Set Definition'

TSTART=TIMEF()

```

```

JJ=0
WRITE(IT,70)
DO I=INT(0.5*NLAYER),NLAYER-1
  DO J=1,IADAPT
    JJ=JJ+1
    NOD(JJ)=AM(J)+I*IELEM
    IF(JJ.EQ.16) THEN
      WRITE(IT,22) (NOD(K), K=1,16)
      JJ=0
    ELSEIF(I*J.EQ.NLAYER*IADAPT .AND. JJ.LT. 16) THEN
      WRITE(IT,22) (NOD(K), K=1,JJ)
    ENDIF
  ENDDO
ENDDO

```

```

JJ=0
WRITE(IT,72)
DO J=1,IADAPT
  JJ=JJ+1
  NOD(JJ)=AM(J)+(NLAYER-1)*IELEM
  IF(JJ.EQ.16) THEN
    WRITE(IT,22) (NOD(K), K=1,16)
    JJ=0
  ELSEIF(J.EQ.IADAPT .AND. JJ.LT. 16) THEN
    WRITE(IT,22) (NOD(K), K=1,JJ)
  ENDIF
ENDDO
WRITE(IT,74)

```

```

TEND=TIMEF( )
WRITE(RECT,'(E10.3)') TEND-TSTART
Print*, 'Completed..Element Set Definition (Clock Time =',
+RECT(1:10),' sec)'

WRITE(IH,*)'Completed..Element Set Definition (Clock Time =',
+RECT(1:10),' sec)'

```

C To Print Mesh Configuration Summary

```

K=(NLAYER+1)*INODE
WRITE(*,90) IELEM*NLAYER,K,K*3,ELEN,XREPEAT,ZTHICK,ITFILE
WRITE(IH,90) IELEM*NLAYER,K,K*3,ELEN,XREPEAT,ZTHICK,ITFILE

```

```

CLOSE (IT)
CLOSE (IH)

```

```

10 FORMAT(3X,69('*'),/,3X, '*',3X,
+'Welcome to Mesh Generation Program for PTC Scratch '
+'Consortium',3X
+,'*',/,3X, '*',14X,'(Version 1.1 - Updated on 16 March 2005)',14X,
+'*', /,3X,69('*'),/)
11 FORMAT(' *NODE, NSET=BOT')
12 FORMAT(I8,3(' ',3X,E12.6))

```

```

14 FORMAT('*NODE, NSET=SET1')
16 FORMAT('*NCOPY, SHIFT, OLD SET=BOT, NEW SET=TOP, CHANGE NUMBER='
+      ,I8,/,X,2(X,','),E12.6,/,2X,6(',','X'))
18 FORMAT('*NFILL, BIAS=1.0, NSET=BODY',/, ' BOT, TOP',2(',','I6))
20 FORMAT('*NSET, NSET=NALL',/, ' BOT, BODY, TOP')
21 FORMAT('*NSET, NSET=SIDE')
22 FORMAT(X,I8,15(',','2X,I8))
23 FORMAT('*NSET, NSET=HEAD')
24 FORMAT('*NSET, NSET=TAIL')
25 FORMAT('*NSET, NSET=ENDS',/, ' HEAD, TAIL')
30 FORMAT('*ELEMENT, TYPE=C3D8R, ELSET=BOT')
40 FORMAT(I8,8(',','2X,I8))
50 FORMAT(6X,'No element connectivity for Element',X,I6)
52 FORMAT('*ELCOPY, OLD SET=BOT, NEW SET=BODY, ELEMENT SHIFT='
+      ,I8,', SHIFT NODES=',I8)
54 FORMAT('*ELSET, ELSET=Substrate',/, ' BOT, BODY')
60 FORMAT('*SOLID SECTION,ELSET=Substrate,',
+      ' MATERIAL=PP,CONTROLS=SECT')
65 FORMAT('*SECTION CONTROLS,NAME=SECT,HOURLASS=COMBINED')
70 FORMAT('*ELSET, ELSET=ADA_REMESH')
72 FORMAT('*ELSET, ELSET=TARGET_S2')
74 FORMAT('*Surface, type=ELEMENT, name=Target',/, ' TARGET_S2, S2')
80 FORMAT()
90 FORMAT(/,68('*'),/,3X,'Type of FE element used (ABAQUS): 3D'
+   'Brick elements (C3D8R)',/,3X,'Number of elements created: ',I8
+   ,/,3X,'Number of nodes created: ',I8
+   ,/,3X,'Total number of DOFs: ',I10
+   ,/,3X,'Critical Element Size: ',2(E9.3,'m x '),E9.3,'m'
+   ,/,3X,'Output file created: ',A20,/,68('*'))
888 STOP
END

```

APPENDIX A-4

This appendix contains the plots used to predict indentation depths for different normal loads using Mesh D for Material I.

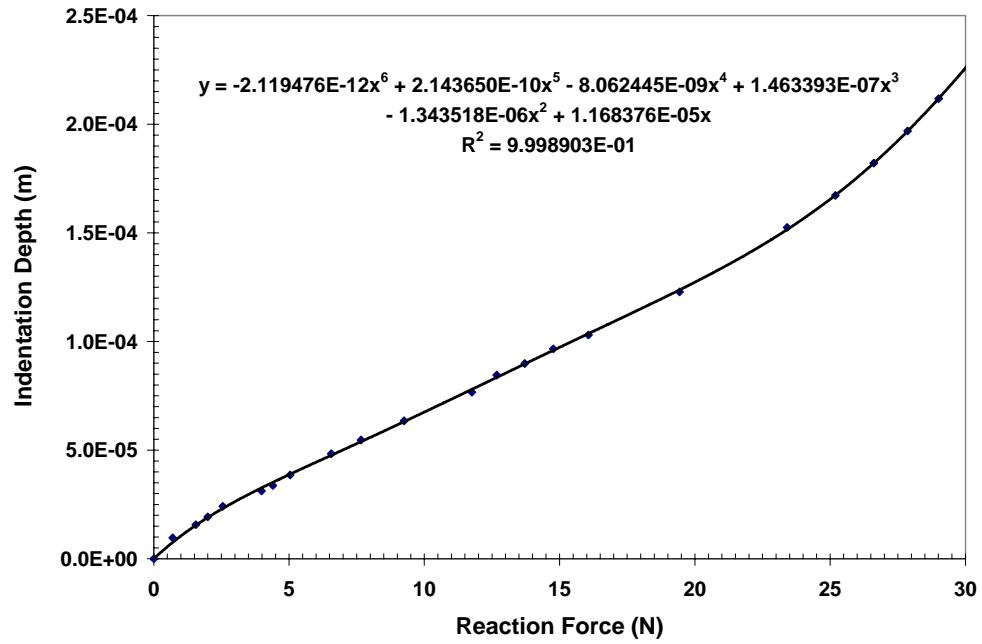


Figure 45: Indentation depths versus normal load for Mesh D and Material I ($\mu_a = 0$).

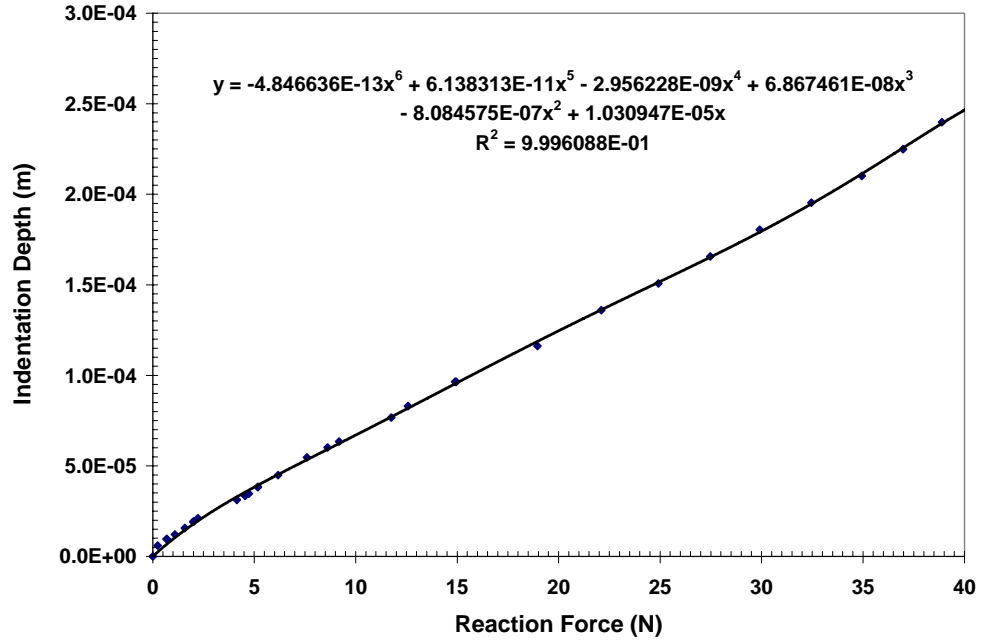


Figure 46: Indentation depths versus normal load for Mesh D and Material I ($\mu_a = 0.3$).

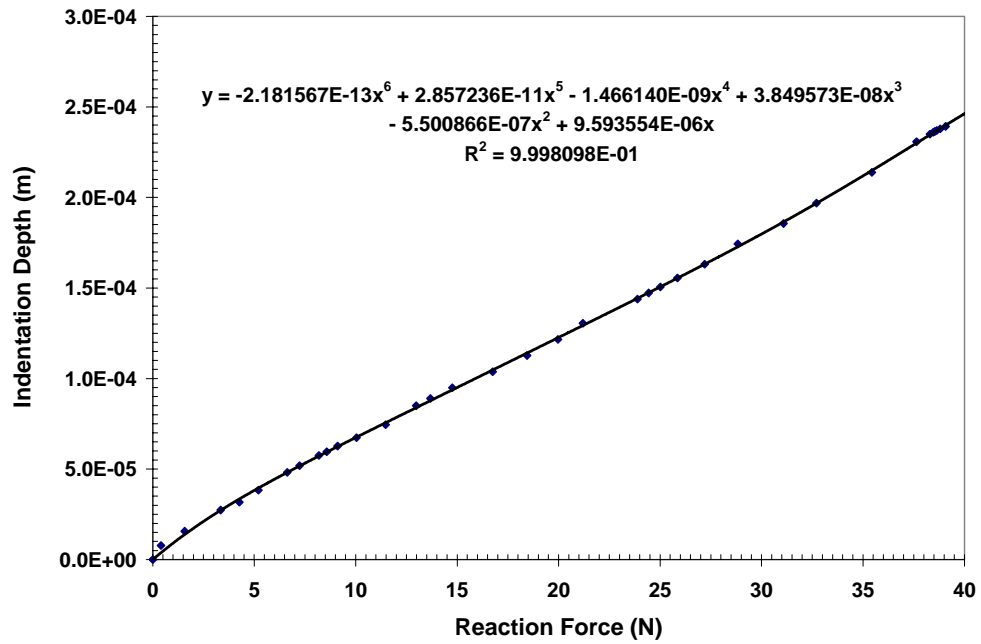


Figure 47: Indentation depths versus normal load for Mesh D and Material I ($\mu_a = 0.6$).

APPENDIX A-5

This appendix contains the plots used to predict indentation depths for different normal loads using Mesh D for Material II.

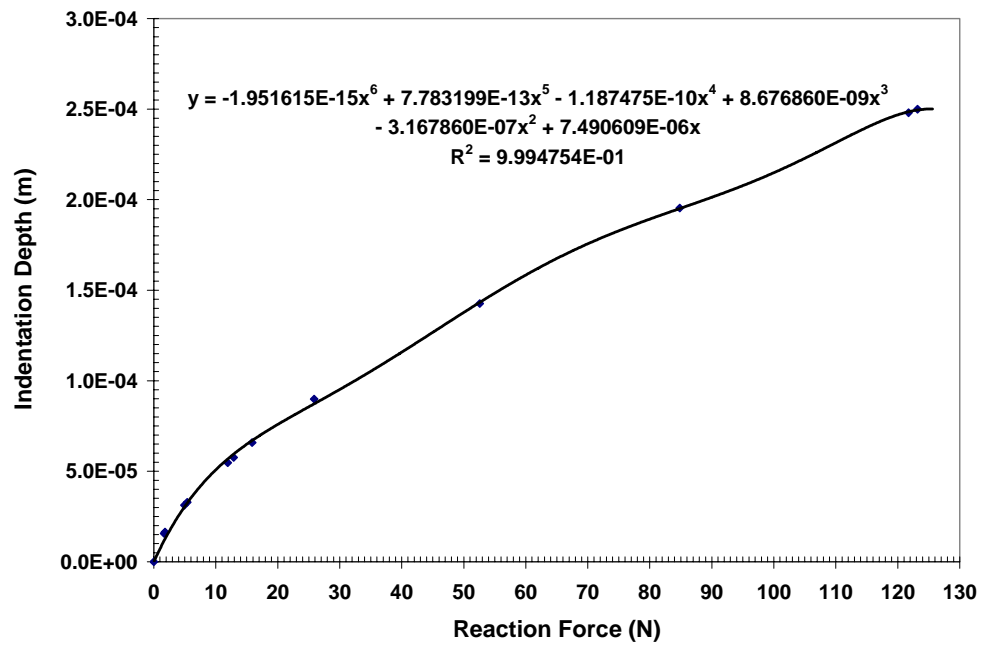


Figure 48: Indentation depths versus normal load for Mesh D and Material II ($\mu_a = 0$).

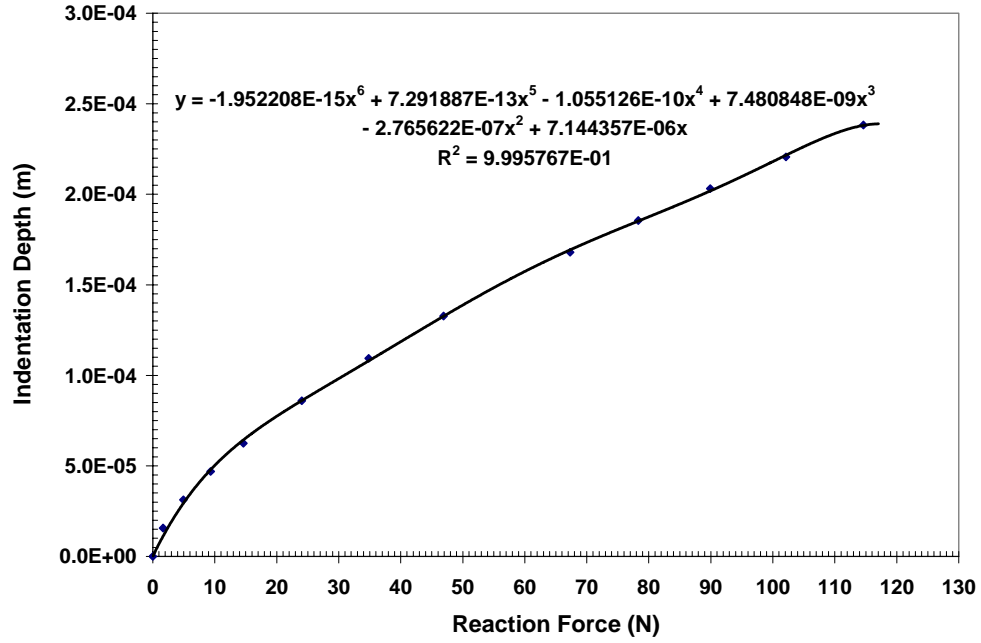


Figure 49: Indentation depths versus normal load for Mesh D and Material II ($\mu_a = 0.3$).

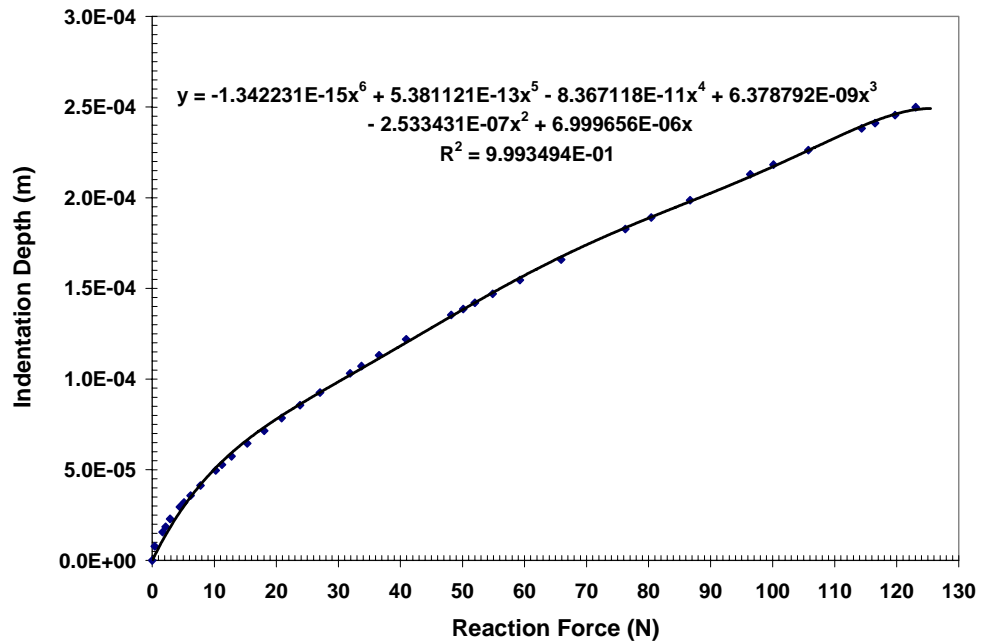


Figure 50: Indentation depths versus normal load for Mesh D and Material II ($\mu_a = 0.6$).

APPENDIX A-6

This appendix contains the plots used to predict indentation depths for different normal loads using Mesh D for Material III.

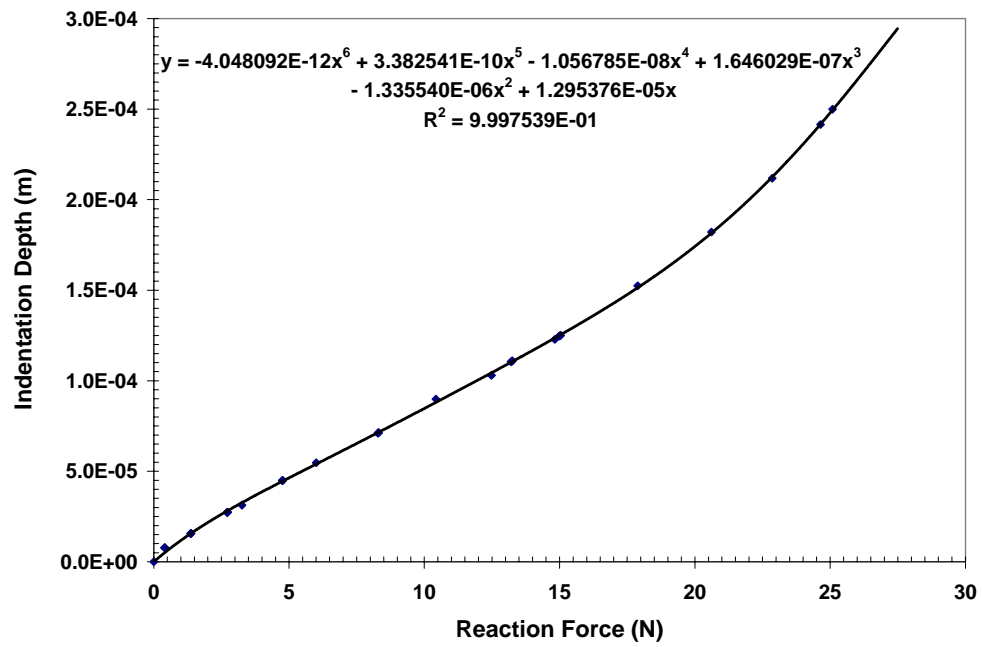


Figure 51: Indentation depths versus normal load for Mesh D and Material III ($\mu_a = 0$).

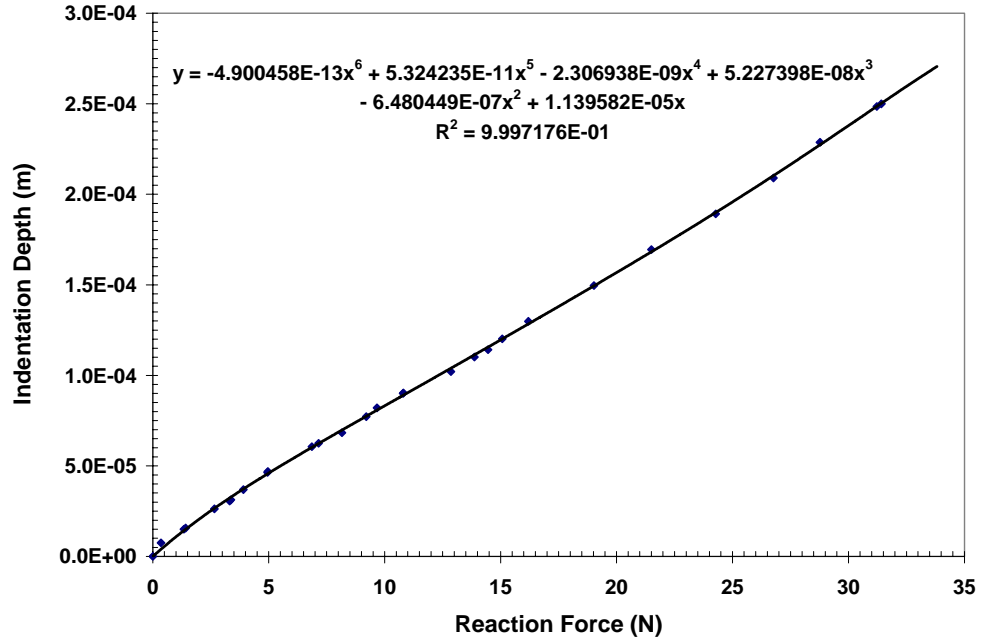


Figure 52: Indentation depths versus normal load for Mesh D and Material III ($\mu_a = 0.3$).

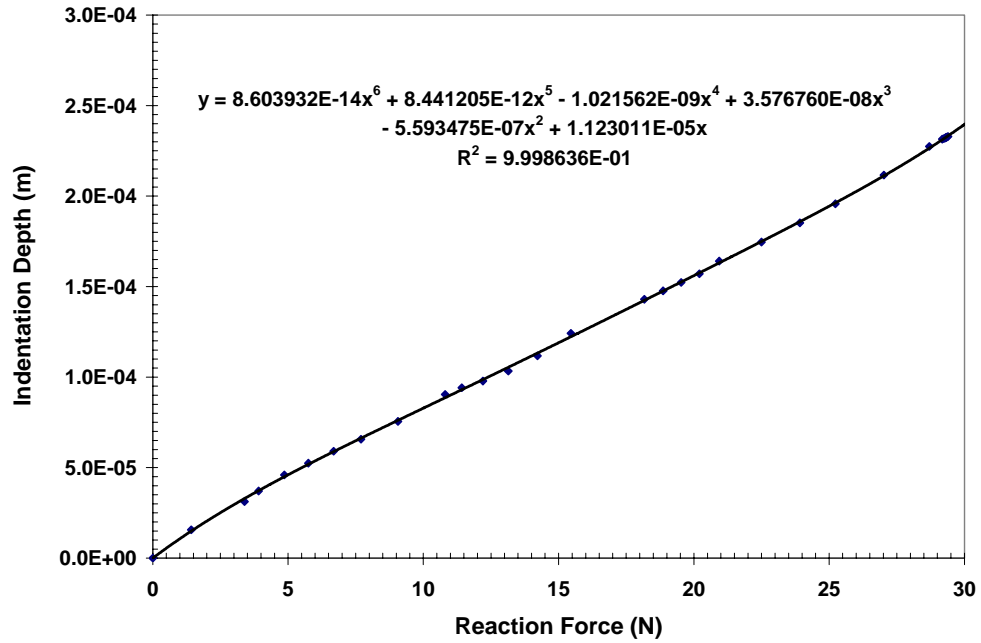


Figure 53: Indentation depths versus normal load for Mesh D and Material III ($\mu_a = 0.6$).

APPENDIX A-7

This appendix contains the FORTRAN program that calculates the constitutive response of the mixed rubber network model.

```

      Program MIXED
C
C      *****
C      This program is to implement the mixed rubber network model
C      *****
C
      IMPLICIT REAL*8(A-H,O-Z)
      DOUBLE PRECISION N,MU,LAMBDA(10000)
      DIMENSION A(10000),B(10000),S(10000)
      CHARACTER*20 TODAY,OUFIL
C
      Implicit Function
      F(A)=SQRT((A*A+2.D0/A-3)**2.D0+(2.D0*A+1.D0/(A*A)-3)**2.D0)
      G(A)=3.0*A/(1.D0-0.6D0*A*A-0.2D0*A**4.D0-0.2D0*A**6.D0)
      H(A)=A**3.D0*(10.D0-15.D0*A+6.D0*A*A)
      P(A)=A*A+1.D0/(A*A)-3
C
      IT=6
      WRITE(*,10)
      PRINT*,'Enter filename of output file without extension'
+          ' ("XXXX")='
      READ*, OUFIL

      OUFIL=OUFIL(1:LEN_TRIM(OUFIL))//'.txt'

      WRITE(*,20)
      READ*, ITEST
C
      File Management
      OPEN (IT, file=OUFIL,Status='Unknown')
      REWIND (IT)
C
      Network parameters
      SA=F(1.D0)
      SC=F(4.04795D0)
C
      Material Properties
      N=25.603
      MU=0.2719
      AA=0.35
C
      Calculation for the stress-strain curve
      NFLAG1=0
      LAMBDA(1)=1.D0
      DO I=1,7001

```

```

      IF(I.GT.1) LAMBDA(I)=LAMBDA(I-1)+1.D-03
      IF(ITEST.EQ.1) S(I)=F(LAMBDA(I))
      IF(ITEST.EQ.2) S(I)=P(LAMBDA(I))
      XX=LAMBDA(I)**2.D0
      IF(S(I).LT.SA) THEN
        A(I)=0.D0
        Z=0.D0
      ELSE
        IF(ITEST.EQ.1) XR=SQRT((XX+2.D0/LAMBDA(I))/(3.D0*N))
        IF(ITEST.EQ.2) XR=SQRT((XX+1.D0/XX+1.D0)/(3.D0*N))
        BR=G(XR)
        Z=(MU*BR)/(3.D0*XR)
        IF(S(I).GE.SA .AND. S(I).LE.SC) THEN
          A(I)=H((S(I)-SA)/(SC-SA))
        ELSEIF(S(I).GT.SC) THEN
          A(I)=1.D0
        ENDIF
      ENDIF
      UU=A(I)*Z*LAMBDA(I)**2.D0
      IF(ITEST.EQ.1) VV=A(I)*Z/LAMBDA(I)
      IF(ITEST.EQ.2) VV=A(I)*Z/XX
      B(I)=1.D0-A(I)
      IF(ITEST.EQ.1) WW=XX-1.D0/LAMBDA(I)
      IF(ITEST.EQ.2) WW=XX-1.D0/XX
      S11=B(I)*AA*WW+UU-VV
      S11=S11/LAMBDA(I)
      IF(I.EQ.1 .OR. MOD(I,100).EQ.0)
+      WRITE(IT,30)LAMBDA(I),S11,S(I)/SC
      ENDDO

3  WRITE(*,40)
   CALL FDATE(TODAY)
   WRITE(IT,50) TODAY
   WRITE(*,60) OUFIL
   CLOSE (IN)
   CLOSE (IT)

10 FORMAT(3X,60('*'),/,3X,'*',10X,
+ 'Welcome to Mixed Rubber Network Program',9X,
+ '*',/,3X,'*',10X,'(Version 1.0 - Updated on 26 May 2005)',10X,
+ '*',/,3X,60('*'),/)
20 FORMAT(/,X,'Select the test output data:',/,
+X,'(1) Extension Data',/,
+X,'(2) Pure Shear Data',/)
30 FORMAT(5(F12.6,4X))
40 FORMAT(/,'End of Program')
50 FORMAT(/,'Program (Ver. 1.0) by G.T. Lim ('',A19,'')')
60 FORMAT(/,'Processed output data has been written to ',A20)
100 STOP
      END

```

APPENDIX A-8

This appendix contains the material subroutine (UHYPER) used for the mixed rubber network model.

```

SUBROUTINE UHYPER(BI1,BI2,AJ,U,UI1,UI2,UI3,TEMP,NOEL,CMNAME,
$                INCOMPFLAG,NUMSTATEV,STATEV,NUMFIELDV,
$                FIELDV,FIELDVINC,NUMPROPS,PROPS)
C
C   INCLUDE 'ABA_PARAM.INC'
C
C   CHARACTER*80 CMNAME
C   DIMENSION U(2),UI1(3),UI2(6),UI3(6),STATEV(*),FIELDV(*),
$           FIELDVINC(*),PROPS(*)
C   REAL*8 N,MU
C
C   File Management
C   IT=6
C   OPEN(IT,
+ file="/home/gtl8110/material/temp/input.txt",Status='Unknown')
C   REWIND (IT)
C
C   MU = PROPS(1)
C   N = PROPS(2)*PROPS(2)
C   D1 = PROPS(3)
C   GAU= PROPS(4)
C   IFLAG=PROPS(5)
C
C   IF(D1.EQ.0.D0) D1=1.D0/(10.D0*MU)
C
C   S=BI1*AJ**(2.D0/3.D0)
C   XR=DSQRT(S/(3.D0*N))
C   C1=(3.D0/5.D0)
C   C2=(1.D0/5.D0)
C   C3=(1.D0/5.D0)
C   DENOM=1.D0-(C1*XR*XR+C2*XR**4.D0+C3*XR**6.D0)
C   P=1.D0/DENOM
C   DP=(2.D0*C1*XR+4.D0*C2*XR**3.D0+6.D0*C3*XR**5.D0)/DENOM**2.D0
C   BR=3.D0*XR*P
C   CN=0.8D0*N+2.D0/(0.8D0*N)
C   AA=1.D0
C   IF(IFLAG.EQ.1) THEN
C     IF(S.LE.CN) THEN
C       ZZ=(S-3.D0)/(CN-3.D0)
C       AA=ZZ**3.D0*(10.D0-15.D0*ZZ+6.D0*ZZ*ZZ)
C     ELSE
C       AA=1.D0
C     ENDIF
C   ENDIF
C   ENDIF

```


C

```

U(1)=0.5D0*(1.D0-AA)*GAU*S+AA*MU*N*(BR*XR+DLOG(BR/DSINH(BR)))
U(1)=U(1)+(AJ*AJ-1.D0)/2.D0-DLOG(AJ)/D1
WRITE(IT,*) U

UI1(1)=0.5D0*(1.D0-AA)*GAU+AA*(MU*P*AJ**(2.D0/3.D0))/2.D0
UI1(2)=0.D0
UI1(3)=(AJ-1.D0/AJ)/D1
WRITE(IT,*) (UI1(J),J=1,3)

UI2(1)=AA*(MU/(12.D0*N))*(DP/XR)*AJ**(4.D0/3.D0)
UI2(2)=0.D0
UI2(3)=(1.D0+1.D0/(AJ*AJ))/D1
UI2(4)=0.D0
UI2(5)=AA*(MU*P)/(3.D0*J**(1.D0/3.D0))
UI2(6)=0.D0
WRITE(IT,*) (UI2(J),J=1,6)

UI3(1)=AA*(MU/(18.D0*N))*(DP/XR)*AJ**(1.D0/3.D0)
UI3(2)=0.D0
UI3(3)=0.D0
UI3(4)=-AA*(MU*P)/(9.D0*J**(4.D0/3.D0))
UI3(5)=0.D0
UI3(6)=-2.D0/(D1*AJ**3.D0)
WRITE(IT,*) (UI3(J),J=1,6)

CLOSE(IT)
RETURN
END

```

APPENDIX A-9

This appendix contains the ABAQUS® analysis input file used for uniaxial extension and pure shear deformation of rubber based on the mixed rubber network model.

```
*HEADING
HYPERELASTIC TEST DATA INPUT
TRELOAR'S EXPERIMENTAL DATA
UNIAXIAL TEST DATA ONLY
*RESTART,WRITE,FREQUENCY=5
*NODE,NSET=ALL
1,
2,1.
3,1.,1.,
4,0.,1.,
5,0.,0.,1.
6,1.,0.,1.
7,1.,1.,1.
8,0.,1.,1.
*NSET,NSET=FACE1
1,2,3,4
*NSET,NSET=FACE2
5,6,7,8
*NSET,NSET=FACE3
1,2,5,6
*NSET,NSET=FACE4
2,
*NSET,NSET=FACE42
3,6,7
*NSET,NSET=FACE5
3,4,7,8
*NSET,NSET=FACE6
4,1,8,5
*EQUATION
** Since the S11 output is Cauchy or true stress, we need to
** determine the nominal stress for post-processing.
** Nodes 3,6,7 are tied to node 2 in dof 1 so that:
** Nominal stress (dof 1) = RF1 (@ node 2) / Original area
** (w/c is 1 x 1 = 1)
2,
FACE42,1,1, 2,1,-1
*ELEMENT,TYPE=C3D8RH,ELSET=ONE
1,1,2,3,4,5,6,7,8
*SOLID SECTION,ELSET=ONE,MATERIAL=TREL
*HOURLASS STIFFNESS
1E01,,
*MATERIAL,NAME=TREL
*HYPERELASTIC,USER,TYPE=INCOMPRESSIBLE,PROPERTIES=5
```

```

0.2719E06, 5.059940711, 0., 0.35E06, 1
**HYPERELASTIC, ARRUDA-BOYCE
** 0.291682227E06, 4.92031012, 0.
**HYPERELASTIC,ARRUDA-BOYCE,TEST DATA INPUT
**UNIAXIAL TEST DATA
** 0.0000E+00, 0
** 1.4254E+05, 0.126
** 2.3230E+05, 0.253
** 3.1598E+05, 0.379
** 4.0888E+05, 0.6
** 5.0188E+05, 0.884
** 5.8860E+05, 1.168
** 6.7532E+05, 1.421
** 8.5808E+05, 2.021
** 1.0471E+06, 2.558
** 1.2144E+06, 3
** 1.5799E+06, 3.758
** 1.9362E+06, 4.358
** 2.2924E+06, 4.749
** 2.6704E+06, 5.179
** 3.0142E+06, 5.432
** 3.3798E+06, 5.653
** 3.7422E+06, 5.905
** 4.0985E+06, 6.076
** 4.4548E+06, 6.189
** 4.8265E+06, 6.316
** 5.1890E+06, 6.455
** 5.5452E+06, 6.537
** 6.2608E+06, 6.632
*STEP,NLGEOM,INC=50
Step 1: Uniaxial Tension
*STATIC,DIRECT
.25,5.
** .25,7.
*BOUNDARY,OP=NEW
** FACE1,3
** FACE3,2
** FACE6,1
** FACE4,1,1,7.
FACE1,3
FACE3,2
FACE5,1
FACE6,1
FACE4,1,1,5.
*OUTPUT,FIELD,FREQUENCY=1
*ELEMENT OUTPUT
S, NE
*NODE OUTPUT,NSET=ALL
U,RF
*OUTPUT,HISTORY,FREQUENCY=1
*END STEP

```

VITA

As a Singaporean, Mr. Goy Teck Lim had his early education in his native country. Mr. Lim earned his Bachelor of Engineering in civil engineering with honours (Second Upper Division) from the National University of Singapore in 1998. For his undergraduate thesis research, Mr. Lim worked under the supervision of Professor Chien Ming Wang in developing bending relationships between classical and higher-order plate solutions for plates and was awarded the *Innovation Merit Award* by the university. Upon graduation, Mr. Lim continued to pursue his graduate research under Professor Wang in the same university and earned his Master of Engineering in civil engineering in 2000.

Mr. Lim's permanent address is Blk 30, #05-042, Balam Road, Singapore 370030, Republic of Singapore.